Dependence of Shortwave Radiation on Cirrus Cloud Parameters and the Derivation of Cirrus Information Using Satellite Observations

Kazuhiko MASUDA

June 1991

Acknowledgements

I would like to express my sincere appreciation to Professor Shoichiro Fukao of Kyoto University for his continued guidance, suggestions, and encouragements during the course of research that has culminated in this thesis.

I acknowledge with deep appreciation Professor Hisanao Ogura of Kyoto University for his invaluable comments and encouragements throughout the present work. I thank Professor Susumu Kato of Kyoto University for his valuable comments on this work.

Special thanks are due to Dr. Tsutomu Takashima of Meteorological Research Institute for his continued cooperation during this research and careful reading of the manuscript.

I would also like to express my deep appreciation to Professor Tadashi Mukai of Kobe University, Professor Sonoyo Mukai of Kinki University, Emeritus Professor Sueo Ueno of Kyoto University, and Professors Takashi Kusaka and Yoshiyuki Kawata of Kanazawa Institute of Technology for their helpful suggestions and comments. I also would like to thank Dr. Shoji Asano of Meteorological Research Institute for useful discussions and Mr. Yohzo Takayama of Meteorological Research Institute for his kind cooperation.

Computations used in the present work were carried out on the HITAC S810/10 and M280H computers of Meteorological Research Institute.

Abstract

To develop a monitoring technique for estimating the shortwave radiation absorbed in the ocean (I^{*}_{abs}) from space, dependence of I^{*}_{abs} and the upward irradiance at the top of the atmosphere (I^{t}) on cirrus cloud parameters are investigated in a model atmosphere-ocean system in the wavelength (λ) region ranging from 0.285 μm to 5.0 μm. The cirrus cloud is assumed to be composed of hexagonal ice crystals (columns and plates). The effects of orientation of crystals are also estimated, for cases in which they are randomly oriented in space and in which they are randomly oriented in a horizontal plane with their long axes parallel to the ground. The relationships between I^{*}_{abs} (or I^{t}) and radiance measured by the NOAA-AVHRR radiometer are discussed. Numerical simulation shows that the type and orientation of the ice crystals cannot be neglected to achieve the accuracy of 10Wm^{-2} that is required for climate understanding.

A method is suggested for deriving cirrus cloud parameters over the oceans using the visible and near-infrared channels (λ = 0.63 μm, 0.86 μm, and 1.61 μm) of the future series of NOAA-AVHRR radiometers. Reflectance and radiance of the upwelling radiation at the top of a model atmosphere-ocean system are computed at the above wavelengths. The computational results show the feasibility of deriving cirrus cloud parameters using the proposed channels. In particular, the following features are noted. (1) It is possible to distinguish the thermodynamic phase of cloud particles using multi-channels that include 1.61 μm. (2) Optical phenomena such as subsun and subparhelic circle are noted only for two-dimensional orientations of ice crystals. (3) Wavelength of 0.86 μm is more suitable for thin cirrus cloud observation than that of 0.63 μm because of the effects produced by absorption by stratospheric ozone and scattering by molecules.

Table of Contents

List of Figures

List of Tables

Chapter 1 Introduction

1.1 Background

Optical characteristics of a cirrus cloud, such as optical thickness, water content, and the shape, dimension, orientation, and thermodynamic phase of the cloud particles, are noted as essential components for understanding the mechanism of climate change or for improving weather forecasts. Evaluation of its characteristics is also required to derive surface parameters remotely from space. But these characteristic are not known precisely, partly because cirrus clouds occur at high altitudes in the atmosphere (sometimes above the lower clouds), and are not easily observable from ground stations, and partly because satellites cannot measure their precise characteristics, particularly if they are thin.

Knowledge of scattering and absorbing properties of atmospheric clouds and aerosols is of vital importance for remote sensing of cloud and aerosol composition. Also, this knowledge is relevant to the radiation budget and, hence, to the climate and climatic changes of the earth-atmosphere system. The radiation budget at the ocean surface is required for several research areas: (1) as a boundary condition for ocean models, (2) to understand the role of radiation in air-sea interactions, (3) to estimate meridional heat transport in the oceans, and (4) to validate coupled ocean-atmosphere models. The accuracy to which incoming shortwave (solar) irradiance must be known for such research areas is, for example, $\sim 10 Wm^{-2}$ for monthly averages in each $2°$ latitude by $10°$ longitude box in the tropical zone for the TOGA (Tropical Ocean and Global Atmosphere) project (WMO, 1984). Accuracy requirements for the surface radiation budget for WOCE (World Ocean Circulation Experiment) project is similar to that for TOGA (WMO, 1986). Effects of cirrus clouds on the radiation budget of the earth-atmosphere are, however, less understood, because of their high location in the troposphere and nonsphericity of ice crystal particles.

For estimating the incident solar radiation at the ocean surface, empirical or simple physical formulae (bulk models) that are based on surface observations such as cloud amount and type have been widely used (Reed, 1977;

Dobson and Smith, 1988; and others). However none of these formulae is able to achieve the $10Wm^{-2}$ accuracy which is needed at a number of stations (Dobson and Smith, 1988). Methods based on satellite data to estimate shortwave irradiance on the earth's surface have recently been developed. These methods could be divided into two categories, statistical and physical. Statistical methods use empirical relationships derived from correlations between global radiation estimates from satellite data and those from nearby stations (Tarpley, 1979; and others). Tarpley (1979) found a standard error in the satellite-derived daily incident solar radiation at the earth's surface of 10% of the mean when compared against pyranometer measurements. Methods based on physical models use satellite data as an indicator of which parameters are necessary for calculations of the radiation using radiative transfer models (Gautier, Diak, and Masse, 1980; Diak and Gautier, 1983; Möser and Raschke, 1983; and others). The accuracy of the incident shortwave irradiance computed by methods that use physical models is, for example, $30Wm^{-2}$ for the monthly mean values at noon by Möser and Raschke (1983). These physical models use simple equations or a two-stream approximation to calculate the radiation, which may be one of the sources of the error of the inferred irradiances.

Theoretical studies of radiation budgets have been reported for an atmosphere-cloud model bounded by a Lambertian surface (Freeman and Liou, 1979) or a cloudless atmosphere-ocean model (Nakajima and Tanaka, 1983). It was found that radiation absorbed in the ocean (I^{*}_{abs}) is closely correlated with reflected radiation at the top of the atmosphere ($I^{\uparrow}$), especially if there is little absorption in the atmosphere (Masuda and Takashima, 1988). To further develop these concepts, the effect of cirrus clouds parameters on the radiation in the atmosphere should be evaluated by numerical simulation using realistic models of atmosphere, cirrus clouds, and earth's surface. In this approach, a single scattering phase function of ice cloud particles is required, and a procedure to calculate radiative field in a realistic atmosphere-ocean model including a cirrus cloud layer is needed.

The most familiar ice crystals are the complicated branching crystal forms, commonly called snowflakes. Although snowflakes occur most frequently near the

ground, other shapes of ice crystals can occur at other heights in the atmosphere given a proper combination of temperature and humidity. Ono (1970) developed a classification of typical crystal shapes according to the temperature ranges (Table 1.1). This classification is based on an examination of more than 10,000 crystals sampled *in situ* by flights through about 120 clouds during three winters (1966-68) in southeast Australia, and on the results of others, As shown in Table 1.1, the fundamental form of the ice crystals is the hexagonal prism. This geometric form can be classified in two basic types, the columnar and the plate ice crystal (Fig.1.1).

A summary of *in situ* aircraft observations undertaken from 1945 to 1980 is given by Liou (1986), where the predominant ice crystal types are nonspherical bullets, columns, and plates. Change of the basic ice crystal form with temperature is also indicated by Ono (1970) (Fig.1.2). Sizes of ice crystals reported before 1975 range from 100 μm to 2000 μm (Liou, 1986). Many crystals with sizes smaller than 100 μm may be missed by the sampling techniques that have been used. Recent aircraft observations reveal that there is a large number of small ice particles, on the order of 10 μm, in cirrus clouds (Varley et al. 1978, Heymsfield and Platt, 1984, Platt et al. 1989). In these observations, however, small ice crystals have been detected by a scatter probe developed for the sizing of spherical water droplets from 2 to 30 μm. Therefore, the size distributions of ice crystal in this range are only very approximate and probably accurate to only a factor of 2 or 3 (Platt et al. 1989).

As for the orientation of ice crystal particles, Ono (1969) indicated by observations that columnar crystals fall with their major axes parallel to the ground, while plates fall with their major axes oriented horizontally. Platt et al. (1978) determined from lidar backscattering measurements that ice crystals in cirrus cloud at approximately -15° C are predominantly plates oriented horizontally. Optical phenomena such as upper and lower tangent arcs, sun dogs (22° parhelia) observed at the ground are produced by reflection and refraction from ice crystals whose major axes are parallel to the ground (Greenler, 1980).

If a particle has a spherical shape, the scattering property such as phase

Table 1.1 Typical crystal forms as functions of temperatures (after Ono, 1970)

Temperature (°C)	Form of ice crystals
≥-3.5	Simple hexagonal plane ice crystals without any internal structure.
-3.5 to -4	Solid/hollow-type columnar ice crystal.
-4 to -6	Needle-type columnar ice crystal.
-6 to -8	Sheath-type columnar ice crystal.
-8 to -9.5	Solid/hollow-type columnar ice crystal.
-9.5 to -12	Thick plate-type ice crystal with or without hollow structure on prism faces.
-12 to -14	Hexagonal plane ice crystals with internal structure, ribs extending along the a axis over the basal faces of the crystals.
-14 to -17	Stellar-type plane ice crystals, including plane crystals dendritic extension, dendritic plane crystals with sector plane at top, and plane crystal with dendritic extensions.
-17 to -19	Hexagonal plane ice crystal with internal structure.
-19 to -22	Thick plane-type ice crystal with hollow structure on prism faces.
-22 to -32	Ice crystals seem to have characteristics of both plane columnar ice crystals. In addition to single columnar or single thick plane ice crystals, irregular aggregates of columns or sectors are common. Scroll, side plane and bullet-type columnar ice crystals are also common crystal forms.

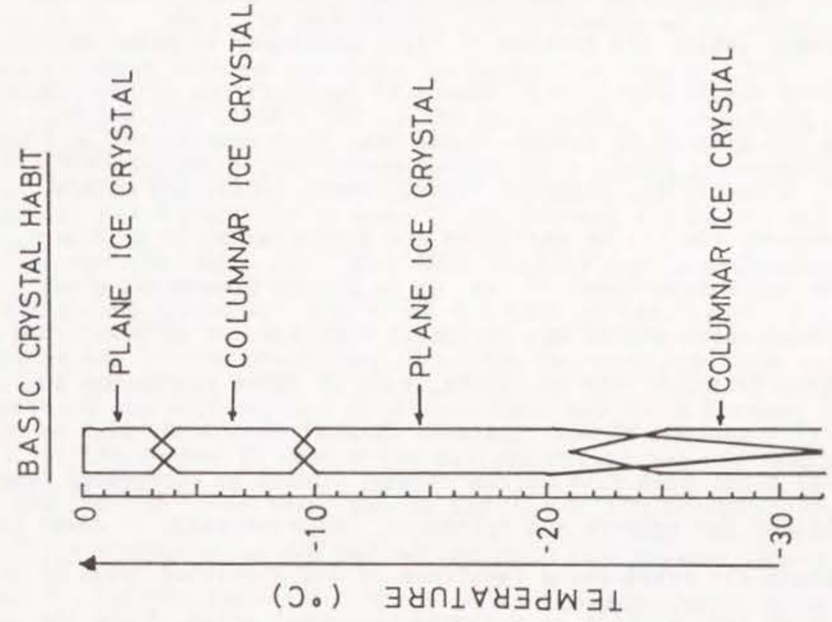

Fig.1.2 Change of the basic ice crystal form with temperature (after Ono, 1970).

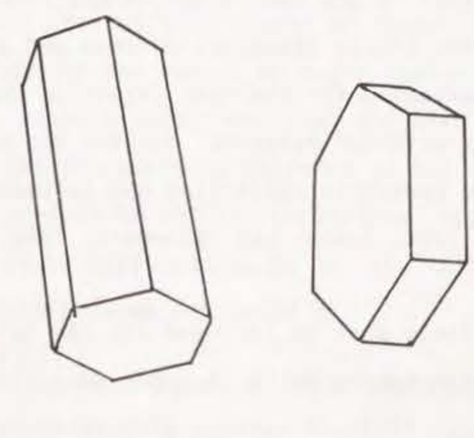

Fig.1.1 Two basic ice crystal types: top, a columnar crystal, bottom, a plate crystal.

function can be precisely evaluated using Mie scattering theory. With the numerical tables (Deirmendjian, 1969) and existing Mie computer programs (e.g., Bohren and Huffman, 1983), the problem of light scattered by water spheres seems to have been completely solved. Numerical computations of the radiation field including the effects of cirrus clouds have been carried out by Plass and Kattawar (1971), Liou (1974), Stephens (1980), Asano (1983) and others. In their works, however, the cirrus particles are approximated by cylinders, by spheres with the refractive index of ice, or by Henyey-Greenstein phase functions. Although these models may represent some aspects of scattering and radiative characteristics of cirrus clouds, none of these approaches account for the hexagonal structure of ice crystals. Optical phenomena, such as halos and numerous arcs associated with cirrus clouds, cannot be reproduced from scattering solutions for spheres and cylinders. Unfortunately, it seems to be difficult to obtain the exact phase functions of ice particles, even if we assume the shape of ice crystals is a simple hexagonal prism. Since the sizes of atmospheric hexagonal ice crystals are normally much larger than or at least comparable to the wavelengths of solar radiation (0.2-$5.0\,\mu m$), the geometrical optics approximation method may be utilized to evaluate their scattering characteristics. Computations of angular scattering patterns for hexagonal ice crystals were first reported by Jacobowitz (1971) assuming infinitely long hexagonal columns. Wendling et al. (1979), Coleman and Liou (1980) undertook a more comprehensive geometrical optics approximation analyses to evaluate the scattering phase function for finite hexagonal columns and plates. More recently, this method was extended for the case involving complete polarization information for arbitrarily oriented hexagonal columns and plates, which includes contributions from geometric reflection and refraction and Fraunhofer diffraction (Cai and Liou, 1982; Takano and Jayaweera, 1985; Takano and Liou, 1989a).

Multiple scattering effects must be included for the calculations of radiation for a realistic atmosphere which includes molecules, aerosols, and clouds (Takashima and Masuda, 1988). A variety of techniques have been developed for computing the radiance and polarization of multiply-scattered light (Chandrasekhar, 1960; Twomey et al., 1966; Hansen, 1971; Plass et al., 1973; Lacis and Hansen, 1974; Takashima, 1975, 1985; Nakajima and Tanaka, 1986; de Haan et al., 1987; Ito and Oguchi, 1987; Stamnes et al. 1988; and others). Reviews of these methods are given by Hansen and Travis (1974), van de Hulst (1980), and Lenoble (1985). One of the most widely used methods is the "adding method". The essence of the adding method is a simple straightforward geometrical ray tracing technique. If the diffuse reflection and transmission functions for the radiation field, which has arisen in consequence of one or more scattering processes, are known for each of two layers, the diffuse reflection and transmission functions from the combined layer can be obtained by computing the successive reflections back and forth between the two layers (Fig. 1.3). Let R_1 and T_1 denote the diffuse reflection and transmission functions for the first layer and R_2 and T_2 for the second layer, D and U for the diffuse transmission and reflection functions between layers 1 and 2, and R_{12} and T_{12} for the combined diffuse reflection and transmission functions. Then equations governing the diffuse reflection and transmission functions for the two layers are written as,

$$S = R_1 R_2 (1 - R_1 R_2)^{-1} \qquad (1.1)$$

$$D = T_1 + ST_1 + S\exp(-\tau_1/\mu_0) \qquad (1.2)$$

$$U = R_2 D + R_2 \exp(-\tau_1/\mu_0) \qquad (1.3)$$

$$R_{12} = R_1 + \exp(-\tau_1/\mu)U + T_1 U \qquad (1.4)$$

$$T_{12} = \exp(-\tau_2/\mu)D + T_2\exp(-\tau_1/\mu_0) + T_2 D \qquad (1.5),$$

where τ_1 and τ_2 are optical thicknesses of layers 1 and 2, respectively, and μ_0 and μ are cosines of the zenith or nadir angles of the incident and emergent radiation, respectively. Note that the directly transmitted radiation without any scattering processes is excluded in Eqs. (1.2) and (1.5). In Eqs. (1.1) - (1.5), the product of any two parameters implies that integration over the solid angle is to be performed so as to take into account all possible multiple-scatter contributions expressed as,

$$AB = \frac{1}{4\pi\mu'}\int_0^{2\pi}\int_0^1 A(\mu,\phi;\mu',\phi')B(\mu',\phi';\mu_0,\phi_0)d\mu' d\phi' \qquad (1.6)$$

in which A and B can be any of the parameters R, T, U, and D. Here, functions A

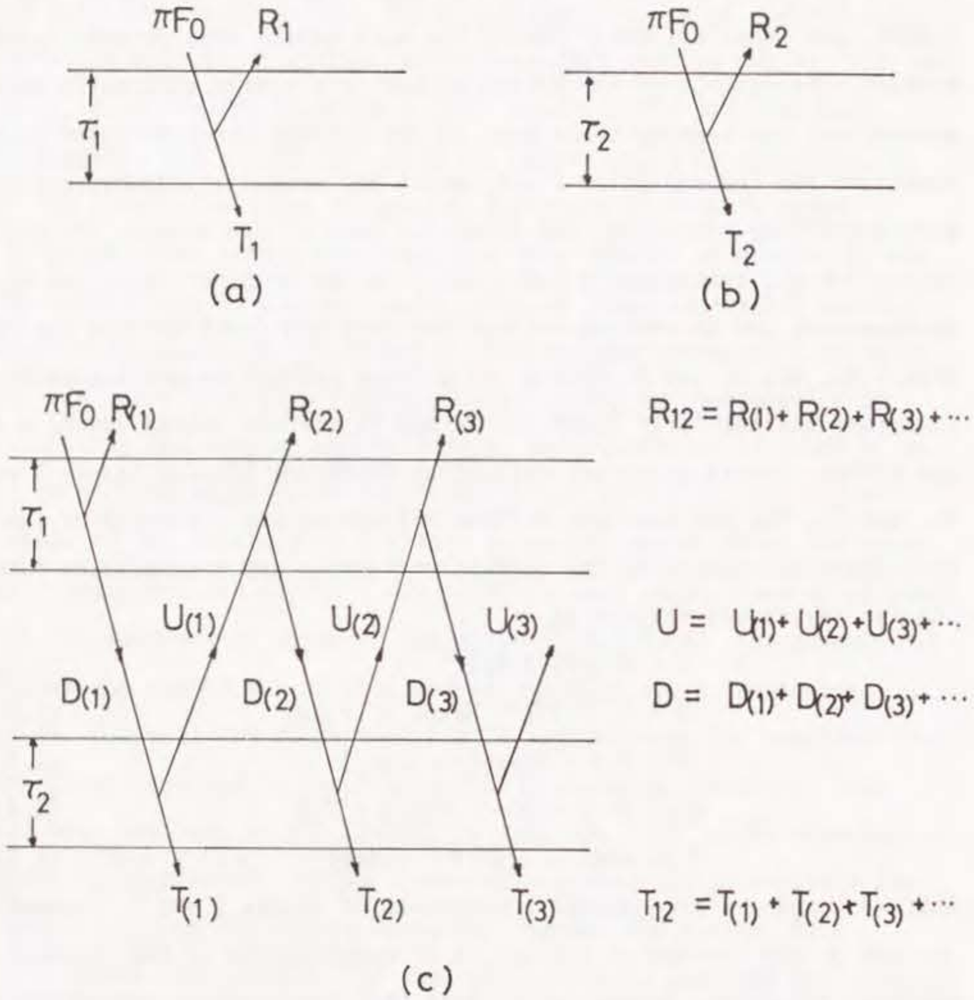

Fig.1.3 Schematic representation of the adding method.
(a) layer 1 of optical thickness τ_1,
(b) layer 2 of optical thickness τ_2,
(c) combined layer of optical thickness τ_1 and τ_2,
where the two layers of the atmosphere are illustrated as if they were physically separated for convenience. πF_0 shows the incident radiation at the top.

and *B* are based on Chandrasekhar's definition where relation between incident (I_{in}) and emergent (I_{em}) radiations is expressed by the form (Chandrasekhar, 1960),

$$I_{em}(\mu,\phi) = \frac{1}{4\pi\mu}\int_0^{2\pi}\int_0^1 A(\mu,\phi;\mu',\phi')I_{in}(\mu',\phi')d\mu' d\phi'. \quad (1.7)$$

It should be noted that these equations are for the radiation that does not include polarization effects. A complete set of equations including polarization effects is given by Hansen (1971). In practice, azimuth-dependent functions are approximated by a Fourier series expansion in $\phi-\phi_0$. Each term in the Fourier series may then be treated independently, allowing savings in computer storage requirements.

The adding procedure is begun for initial layers of such small optical thickness that the single scattering approximations for the diffuse reflection and transmission functions may be sufficiently accurate. Various initialization schemes are summarized by Wiscombe (1976). This procedure may be repeated to evaluate the diffuse reflection and transmission functions until the desirable optical thickness is reached. When the two layers have the same optical depth, the adding method is referred as the doubling method.

As discussed before, ice crystals in nature may have a preferred orientation in which their major axes are horizontal. In this case, the single scattering parameters (phase function, extinction and scattering cross sections) depend on the direction of the incident radiation. Liou (1980) undertook the theoretical formulation for the transfer of radiation in horizontally-oriented ice crystals. Using the doubling method, Asano (1983) carried out a detailed analysis of the transfer of solar radiation in hypothetical cloud models (Henyey-Greenstein phase function) with single scattering properties varying with the incident angle of the light beam. Recently the effects of the shape and orientation of hexagonal ice crystals on the solar radiation were examined by Takano and Liou (1989b) and by Masuda and Takashima (1989) using a realistic ice crystal model (hexagonal ice crystals) with the aid of the doubling-adding method. The former calculated the reflected and transmitted radiance and degree of polarization from a single cloud layer and showed that the spherical model is inadequate for use in the interpretation of bidirectional reflectance from cirrus clouds. The latter calculated the radiance just above and below the cloud layer in an atmosphere-ocean model.

Satellite measurements can provide global coverage of cloud properties such as cloud-top height and temperature, cloud amount, and cloud emissivity. Such data are essential for the inclusion of cloud parameterizations in global radiation budget calculation and general circulation models. The International Satellite Cloud Climatology Project (ISCCP) has been approved as the first project of the World Climate Research Programme (WCRP). The basic objective of the ISCCP is to collect and analyze satellite radiance data to infer the global distribution of cloud effects on climate (Schiffer and Rossow, 1983). The primary data are the two standard visible (0.6 μm) and IR (11 μm) radiance collected from geostationary meteorological satellites and polar-orbiting satellites. However, because of the great variability in the optical properties of high cirrus clouds, it is difficult to obtain accurate information about the geographical distribution of cirrus clouds using conventional visible and IR radiometers.

In recent years, with the advent of multichannel imaging instruments such as the Advanced Very High Resolution Radiometer (AVHRR) and the great increase in computing power, it has become possible to utilize objective techniques to determine cloud amount as well as some vertical structures of cloud. Arking and Childs (1985) used three channels (visible, 3.7 μm, and 11 μm) from the AVHRR to retrieve cloud amount, optical thickness, cloud-top temperature and a microphysical model parameter. Barton (1983) analyzed data from two narrow-band channels in the 2.7 μm band of carbon dioxide and water vapor on board Nimbus 5 to yield the high-cloud amount and height information. The advantage of using this absorption band is that radiation which is reflected by the earth's surface or by cloud at low and middle altitudes is not detected by the radiometer. For this reason, the radiometer is sensitive only to clouds at altitudes above 6km. Advances in research have been made on remote sensing of vertical structure and cloud amount, employing sounding radiometers such as the High-Resolution Infrared Sounder (HIRS) on board Nimbus 6 (Feddes and Liou,

1978; Yeh and Liou, 1983; Yeh, 1984).

In the decade of the 1990s, a large number of satellites are being planned for launch that will carry out new or improved instruments. The AVHRR to be planned on board the NOAA K, L, and M satellites is to be changed beginning with NOAA-K (to be launched in June 1993) so that Channel 1 (0.58-0.68 μm) is slightly modified, the band width of Channel 2 is narrower (0.84-0.89 μm), and Channel 3A (1.56-1.66 μm) is added (Sparkman, 1989). Ahmad et al. (1989) showed the feasibility of estimating the aerosol columnar abundance and size distribution from these three channels using a regression method. Furthermore, since ice exhibits relatively strong absorption at about 1.61 μm wavelength region whereas water shows weak absorption, Channel 3A is expected to be used for determining thermodynamic phase of clouds. The normalized spectral response of AVHRR is shown in Fig. 1.4. Curran and Wu (1982) developed a technique for remotely determining cloud-top thermodynamic phase and particle sizes utilizing the measured reflection functions at 0.83 μm, 1.61 μm, and 2.125 μm from multichannel scanning radiometers on Skylab during December 1973. Recently, Wielicki et al. (1990) estimated effective cirrus particle radius of tropical cloud using the 0.83 μm, 1.65 μm, and 2.21 μm bands of the Thematic Mappers on board Landsat 4 and 5. However, both analyses are based on hypothetical spherical ice particles. Therefore, rapid progress is expected in retrieval techniques of cloud parameters from the visible and near-infrared channels of the modified AVHRR based on more realistic model of cirrus cloud particles.

1.2 Outline of the Thesis

In this thesis, the effects of cirrus parameters (e.g., optical thickness, water content, and shape, dimension, orientation, thermodynamic phase of the cloud particles), on the earth radiation budget are quantitatively estimated, and a method for deriving cirrus cloud information over the ocean using measurements made with the visible and near-IR channels of the future series of NOAA-AVHRR radiometers is suggested. Calculations are carried out with the aid of the doubling-adding method.

Since cirrus clouds exhibit a variability in the optical thickness, the

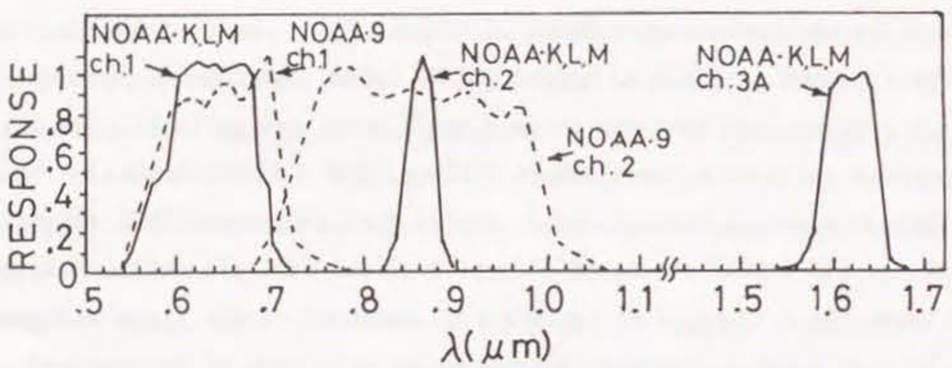

Fig. 1.4 Normalized spectral response of AVHRR channels (after Ahmad et al., 1989).

radiance at the top of the atmosphere may be affected by background aerosols, molecules, and the earth's surface. Therefore, a single cloud layer model is not enough to evaluate the effect of cirrus cloud parameters on the radiation to be measured by satellites. A realistic model including clouds, aerosols, molecules, and earth's surface should be introduced. The atmosphere-ocean system used in the present study is described in Chapter 2, where the plane-parallel, vertically-inhomogeneous atmosphere is simulated by eight homogeneous sublayers. Atmospheric and oceanic components (molecules, aerosols, hydrosols, cloud, and ocean surface) are described.

In Chapter 3, the optical properties of single scattering are examined for (1) hexagonal ice crystals randomly oriented in space; (2) randomly oriented with long axis in the horizontal plane as shown by Ono (1969) and Platt et al. (1978); and (3) spherical water particles. All investigations are done at the effective wavelengths of the future NOAA AVHRR Channels 1 (0.63 μm), 2 (0.86 μm) and 3A (1.61 μm). Single scattering properties of hexagonal ice crystals are calculated using the geometrical optics approximation method whereas those of spherical particles are calculated from the Mie scattering theory. The phase function, extinction cross section, albedo for single scattering, and asymmetry factor are compared. In particular, the dependence of these optical properties on the direction of the incident radiation is discussed in detail for the hexagonal ice crystals randomly oriented with long axis in the horizontal plane.

Dependence of shortwave radiation absorbed in the ocean (I^{w}_{abs}) and upward irradiance at the top of the atmosphere (I^{t}) on atmospheric and oceanic parameters is estimated in Chapter 4 for cloudless atmosphere-ocean system. Effects of aerosols, water vapor content, ozone amount, sea surface roughness, whitecaps, and hydrosols on I^{w}_{abs} and I^{t} are evaluated quantitatively by simulating radiative transfer process in a model atmosphere-ocean system. An appropriate method to estimate I^{w}_{abs} from space is investigated.

In Chapter 5, equations of radiative transfer are derived for the atmosphere model which contains both horizontally-oriented ice crystals and spherical particles such as aerosols. Next, a dependence of I^{w}_{abs} together with

I^{t} on cirrus cloud parameters is estimated. The effects of the thermodynamic phase of the cloud particles and the shape and orientation of the hexagonal ice crystals on I^{*}_{abs} and I^{t} are especially examined. Further, a method to infer I^{*}_{abs} and I^{t} from the NOAA-AVHRR radiometer, together with its accuracy, are discussed.

In Chapter 6, the effects of the water content and optical thickness of the cloud layer, thermodynamic phase of the cloud particles, and the shape and orientation of the hexagonal ice crystals on the radiation at the top of the atmosphere are estimated at the effective wavelengths of AVHRR Channels 1 (0.63 μm), 2 (0.86 μm) and 3A (1.61 μm) using the single scattering phase functions and albedo for single scattering which are described in Chapter 3. A retrieval technique of cloud parameters using multichannels that include Channel 3A (1.61 μm) of the future series NOAA meteorological satellite is then suggested.

Chapter 2 Atmosphere-Ocean Model

2.1 Introduction

Figure 2.1 shows the diagram of the atmosphere-ocean system used in the present computation. The plane-parallel, vertically inhomogeneous atmosphere is simulated by eight homogeneous sublayers (0-2km, 2-5km, 5-10km, 10-11km, 11-13km, 13-20km, 20-30km, and 30-100km). The optical thicknesses of the atmospheric molecular scattering constituents and absorbent constituents such as ozone, water vapor, and oxygen are obtained by the LOWTRAN6 (Kneizys et al., 1983) for the summer midlatitude region. The vertical aerosol distributions by Selby and McClatchey (1972) are modified so that the optical thickness (τ) of aerosols equals 0.250 and 0.873, respectively, for the clear and the hazy models at $\lambda = 0.555\,\mu$m, which correspond to the visibility of 23km and 5km, respectively, at the surface. The cirrus cloud is assumed to be in the fourth layer (10-11km). In the present computation, six cases of vertical water content (VWC=0.0gm^{-2}, 2.5gm^{-2}, 10gm^{-2}, 40gm^{-2}, 160gm^{-2}, and 640gm^{-2}) are considered.

The ocean surface is simulated by multiple facets whose slopes vary according to the isotropic Gaussian distribution with respect to surface wind speed (Cox amd Munk, 1955).

The ocean is assumed to be homogeneous and its bottom is also assumed to absorb all radiation incident on it. The optical thickness of the ocean (τ) is assumed to be 20.0 at 0.555μm; the corresponding geometrical depth varies from 28m to 387m with the change of the turbidity condition and the refractive index of hydrosols. Note that the ocean model with this optical thickness could in practice be considered to have infinite optical thickness (Masuda and Takashima, 1988). Reflection by the ocean surface is considered in the entire wavelength region (0.285-5.0μm). The radiation from below the ocean surface is considered in the wavelength region ranging from 0.285μm to 1.0μm. In the wavelength region longer than 1.0μm, the radiation from below the ocean surface is neglected.

In order to calculate the solar radiation, which is discussed in Chapters 4

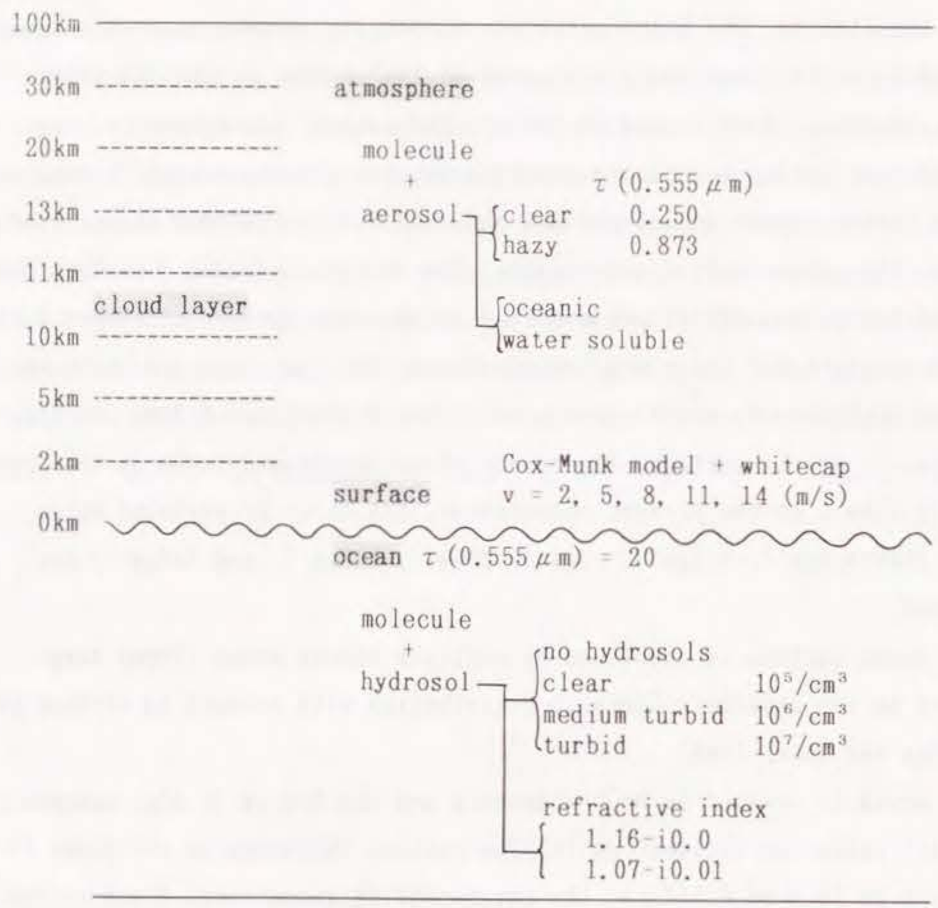

Fig.2.1 Diagram showing the atmosphere-ocean system.

and 5, the extraterrestrial solar spectrum compiled by Iqbal (1983) is adopted. We have divided the extraterrestrial solar spectrum from 0.285 μm to 2.5 μm into 83 unequal intervals over each of which the optical properties of the atmosphere are assumed to remain constant (Rao and Takashima, 1986). Beyond 2.5 μm, the interval of 0.1 μm is adopted.

The radiation at the top of and in the atmosphere-ocean system is computed by the doubling-adding method (Hansen, 1971; Lacis and Hansen, 1974; Takashima, 1985). The extended diamond initialization is adopted for doubling procedure (Wiscombe, 1976). For the number of discrete directions, the region in the atmosphere is covered by quadrature points determined as zeros of a shifted 15th Legendre polynomial of range (0,1). The quadrature points in the region from the nadir to the critical angle in the ocean are connected with those for the atmosphere by Snell's law. An additional set of nine quadrature points is mapped into the region from the critical angle to the horizon.

2.2 Molecules

The phase function by the atmospheric and oceanic molecules is expressed by the Rayleigh's law given by

$$P(\Theta)=(3/4)\cdot(1+\cos^2\Theta)\ , \tag{2.1}$$

where Θ is the scattering angle.

As for the ocean, a pure water model is assumed for molecular scattering and absorption, where the effect of the dissolved salts is ignored. The scattering coefficient of pure water is given by Morel (1974). The absorption coefficient is obtained from the imaginary part of the refractive index of water given by Hale and Querry (1973).

2.3 Aerosols

Two types of aerosol models, the "oceanic" aerosols and the "water soluble" aerosols given by Radiation Commission (1986) are considered. The oceanic particles are sea spray particles generated at the sea surface by the action of the wind; they consist of 30% sea salt and 70% liquid water. The water soluble particles are continental origin particles composed of ammonium and calcium sulfate and also organic components (Shettle and Fenn, 1979). The size distributions of these aerosol models are represented by the log-normal distribution functions.

$$dn(r)/dr = \frac{1}{(2\pi)^{1/2} r \ln(\sigma)} e^{-(\ln(r)-\ln(\bar{r}))^2/(2\ln^2(\sigma))} \tag{2.2}$$

where the parameters $\bar{r}$ and σ represent geometric mean radius and standard deviation, respectively. Aerosols are assumed to be spherical and $\bar{r}$ and σ are $0.3\,\mu$m and $2.51\,\mu$m for the oceanic aerosols and $0.005\,\mu$m and $2.99\,\mu$m for the water soluble aerosols, respectively. The single scattering phase functions are calculated from Mie scattering theory for $0.001\,\mu\mathrm{m} < r < 10\,\mu$m. Phase function is shown in Fig.2.2(a) for $\lambda = 0.63\,\mu$m, where the refractive indices are $1.377 - i1.54\times10^{-8}$ for the oceanic aerosols and $1.53 - i0.006$ for the water soluble aerosols, respectively. Note that the imaginary part of the water soluble aerosols should be looked upon as effective values as discussed by Bohren and Huffman (1983) in detail. Maritime aerosol model is specified as a mixture of the oceanic and water soluble aerosols (Radiation Commission, 1986). The relative proportions of aerosols of oceanic and water soluble aerosols will vary with the distance from the coast, wind speed and so on. Radiation Commission (1986) selected an aerosol model which is composed of 95% oceanic aerosols and 5% water soluble aerosols by volume as a basic maritime aerosols model. In this thesis, however, two extreme cases, a complete oceanic model and a complete water soluble model, are considered.

2.4 Hydrosols

Knowledge of hydrosols, such as size distribution, refractive index and turbidity condition, has not yet been established for radiative transfer calculations. Therefore, in the present work, the data compiled by Tanaka and Nakajima (1977) are adopted. Hydrosols are assumed to be spherical and the size distribution is given by the form

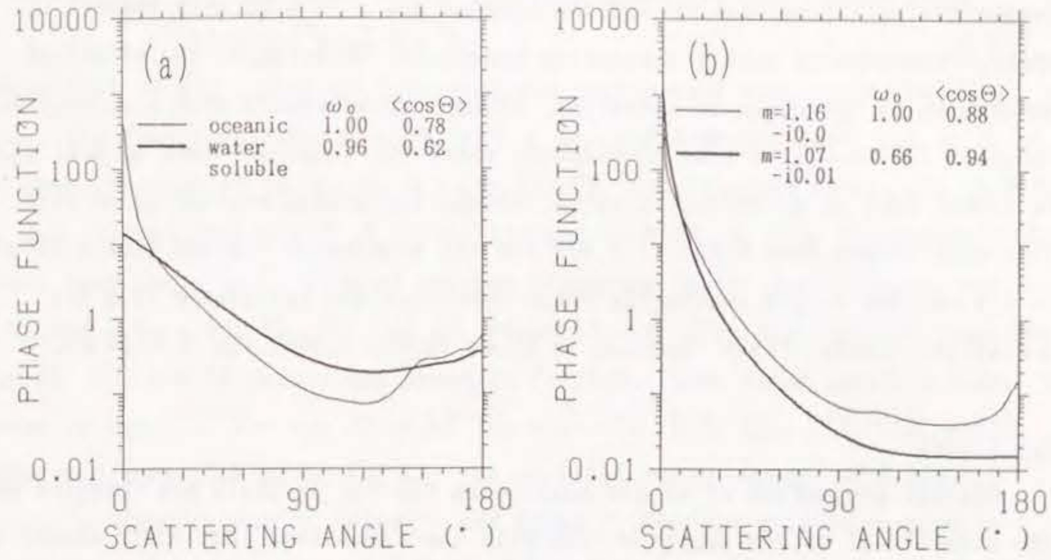

Fig.2.2 Phase function for single scattering for (a) aerosols and (b) hydrosols, respectively, at $\lambda = 0.63\,\mu$m.

$$dn(r)/dr = c \cdot r^{-4} \quad (0.1\mu m < r < 22\mu m), \tag{2.3}$$

where c is a constant representing the turbidity condition. For the pure water ocean model without hydrosols, c=0. For the clear ocean model (C) c=300, corresponding to the hydrosol's number density of 10^5 particles/cm^3. Similarly c=3000, 30000 for the medium turbid (M) and the turbid (T) ocean models, respectively. The refractive indices adopted are 1.16-0.0i with respect to water, representing purely scattering hydrosols. To estimate the effect of absorption by hydrosols on radiation, absorptive hydrosols with a refractive index of 1.07-0.01i is also considered, where the imaginary part of 0.01 should be looked upon as an effective value. Albedo for single scattering of this hydrosols ranges from 0.693 to 0.639 for the wavelength regions from 0.285μm to 1.0μm. The single scattering phase functions are calculated from Mie scattering theory. Phase function is shown in Fig.2.2(b) for λ=0.63μm.

2.5 Clouds

Optical properties of single scattering for ice crystals are computed using the geometrical optics approximation with the assumption that their shapes are hexagonal columns or plates. The refractive index of ice compiled by Warren (1984) is adopted. The polarization effect is neglected. Two cases of orientation of ice crystals are considered. One is three-dimensional (3D) in type wherein the crystal long axes are assumed to be randomly oriented in three dimensions (PL3 and CL3). The other is two-dimensional (2D) in type wherein the crystal long axes are randomly oriented only in the horizontal plane (PL2 and CL2) as discussed by Ono (1969) and Platt et al. (1978) based on measurements. Lengths (l) and radii (a) of hexagonal ice crystals are assumed to be 245μm and 35μm for the column type and 30μm and 100μm for the plate type, respectively, on reference to Figs.5 and 6 by Ono (1969). The volume of a single particle is $7.80\times10^5\mu m^3$ for either case.

For comparison purposes, mass equivalent spherical water particles are considered (LL), where the single scattering phase matrices are calculated from Mie scattering theory. The radius of particles is 55.5μm assuming that the density of ice is 0.92, but uniform size distributions ($53.0<r<58.0\mu m$) are

adopted mainly to smooth out the fluctuation characteristics of scattering by a single particle. The refractive index of water by Hale and Querry (1973) is adopted. To evaluate the effect of the refractive index, spherical ice particles with the same radius are also considered (LS). Furthermore, cloud models C1, C2, and C3 by Deirmendjian (1969) are also compared, whose size distributions are expressed by the modified gamma function in the form,

$$n(r) = a \cdot r^{\alpha} \exp(-b \cdot r^{\gamma}), \tag{2.4}$$

where n(r) is the number of particles per unit volume with radius between r and r+dr. The four constants a, α, b, and γ are positive and real, and α is an integer. Parameters (a, α, b, γ) for C1, C2, and C3 cloud models are (2.3730, 6, 3/2, 1), (1.0851×10^{-2}, 8, 1/24, 3), and (5.5556, 8, 1/3, 3), respectively. Their mode radii (r_c), size of maximum frequency in the distribution, are 4.0, 4.0, and 2.0μm for C1, C2, and C3, respectively. Size distribution functions for C1, C2, and C3 models are shown in Fig.2.3. These cloud particle models are shown in Fig.2.4. For the cloud of ice crystals (PL3, CL3, PL2, CL2) and spherical particles of LL and LS, the vertical water content of $0.0gm^{-2}$, $2.5gm^{-2}$, $10gm^{-2}$, $40gm^{-2}$, $160gm^{-2}$, and $640gm^{-2}$ (Section 2.1) correspond to particle number densities of $0.0m^{-3}$, $3.48\times10^3m^{-3}$, $1.39\times10^4m^{-3}$, $5.58\times10^4m^{-3}$, $2.23\times10^5m^{-3}$, and $8.92\times10^5m^{-3}$. The optical properties of single scattering by these cloud models are discussed in detail in Chapter 3.

2.6 Ocean Surface

The ocean surface is simulated by multiple facets whose slopes vary according to the isotropic Gaussian distribution with respect to wind speed (Cox and Munk, 1955). Cox and Munk made measurements of the sun glitter from aerial photographs. Their measurements covered a wind speed ranging from 0m/s to 14m/s. Let us consider the average brightness of the sea surface over a sufficiently long time and sufficiently wide surface area to smooth out fluctuations due to individual glitter sparkles of sunglint. The avarage is then essentially independent of time but varies smoothly with the azimuth and the inclination of the portion of sea surface under consideration. Thus the model surface can numerically be simulated by many facets, whose slope

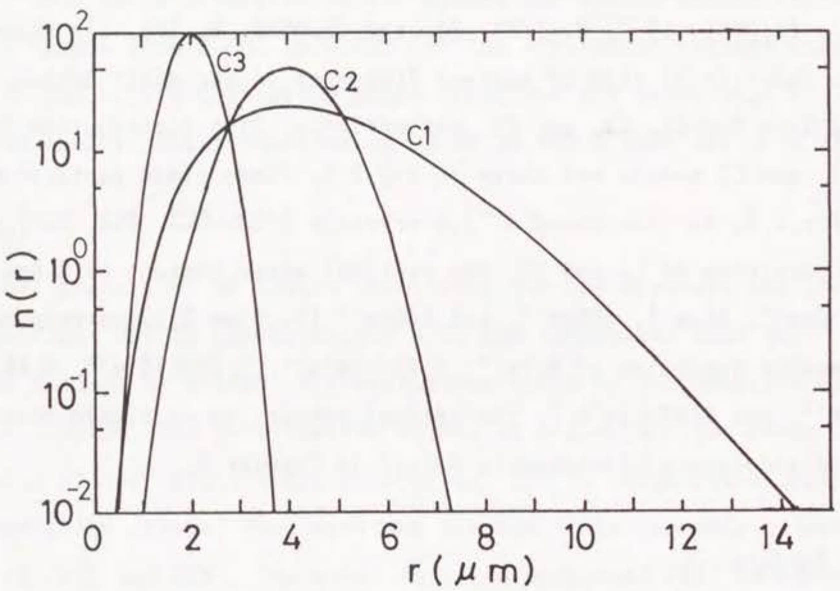

Fig.2.3 Size distribution functions of C1, C2, and C3 cloud models (after Deirmendjian, 1969).

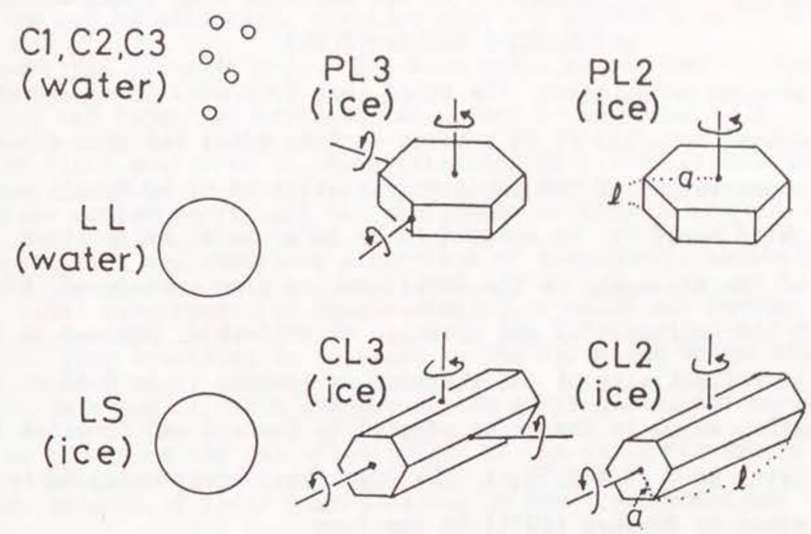

Fig.2.4 Cloud particle models.

components are expressed according to a Gaussian distribution with respect to surface wind. It is isotropic in the case of the distribution independent of wind direction. In this case, the distribution function is expressed as

$$P(z_x, z_y) = (\pi \sigma^2)^{-1} \exp\{-(z_x^2 + z_y^2)/\sigma^2\}, \tag{2.5}$$

where z_x and z_y represent the slope components in orthogonal x and y directions in mean sea surface plane, respectively. They found from the airplane photographs that the mean square slope, regardless of direction, $\sigma^2 = \langle z_x^2 + z_y^2 \rangle_{average}$, increase with the masthead wind speed v(m/s) according to

$$\sigma^2 = 0.003 + 0.00512v \pm 0.004. \tag{2.6}$$

In the present computation, the third term (± 0.004) is neglected. Computational accuracy of this ocean surface model has been discussed using the energy conservation of the incident radiation on it by Masuda and Takashima (1986). Wind speed (v) is assumed to be 2m/s, 5m/s, 8m/s, 11m/s, and 14m/s. The effect of the whitecaps on the irradiance is also considered. Wide variations exist in the reflectivity and coverage of whitecaps. However in the present work, the reflectivity of the whitecap is assumed to be 0.45 at all wavelengths, which is the value adopted by Quenzel and Kaestner (1980) as the reflectivity at $\lambda = 0.4-0.75\mu m$. The fractional areas occupied by the whitecaps, S, are given by Monahan (1971) in the form

$$S = 1.2 \times 10^{-3} \times v^{3.3} (\%). \tag{2.7}$$

Chapter 3 Optical Properties of Single Scattering by Hexagonal Ice Crystals

3.1 Introduction

The angular scattering behavior of water droplet cloud may be precisely described by the Mie scattering theory for a representative polydispersion of homogeneous water sphere. Based on the exact Mie scattering theory, the optical properties of water droplets for any wavelength in the solar, infrared, and microwave spectra can be evaluated, provided that the droplet size distribution is given. However, the changing atmosphere also contains micrometer-sized aerosol particles and large ice crystals, which are nonspherical. The determination of light scattered by these irregular particles is made very difficult by their nonsphericity and the consequent problem of orientation. Knowledge of scattering and absorbing properties of atmospheric clouds and aerosols is of vital importance for remote sensing of cloud and aerosol composition. Also this knowledge is relevant to the radiation budget and, hence, to the climate and climatic changes of the earth-atmosphere system. Effect of cirrus clouds on the radiation budget of the earth-atmosphere is less understood, because of their high location in the troposphere and nonsphericity of ice crystal particles. The nonspherical shapes of ice crystals depend upon such variables as temperature, saturation ratio, and atmospheric conditions. Under normal circumstances, ice crystals have the basic hexagonal structure. The fact that we see halos in cirrus cloudy atmosphere is one of examples that cirrus clouds is composed of hexagonal ice crystals. Moreover, according to a number of *in situ* observations (e.g., Ono, 1969) the sizes of hexagonal crystals normally are on the order of several hundred microns. Thus the geometrical optics approximation may be applicable for the scattering study. Using a geometrical optics approximation, the phase functions of single scattering of nonspherical ice crystals have been reported for simple hexagonal ice crystals (Jacobowitz, 1971; Wendling et al., 1979; Coleman and Liou, 1980; Cai and Liou, 1982; Takano and Jayaweera, 1985; Takano and Liou, 1989a; Muinonen et al., 1989)

In this chapter, the optical properties of single scattering are examined for (1) hexagonal ice crystals randomly oriented in space (PL3 and CL3 in Fig.2.4); (2) randomly oriented with long axis in the horizontal plane (PL2 and CL2 in Fig.2.4) as shown by Ono (1969) and Platt et al. (1978); and (3) spherical water particles (C1, C2, C3, LL, and LS in Fig.2.4). All investigations are done at the effective wavelengths of the future NOAA-AVHRR Channels 1 (0.63 μm), 2 (0.86 μm), and 3A (1.61 μm).

3.2 Phase Function

Single scattering phase function and extinction cross section (σ_e), albedo for single scattering (ω_0), and asymmetry factor ($\langle\cos\Theta\rangle$) were computed using the geometrical optics approximation, including Fraunhofer diffraction effect (Born and Wolf, 1964) for ice crystals on the assumption that their shapes are hexagonal columns (CL) or plates (PL). For the 3D type (PL3 and CL3), scattered energy was averaged over 1° increments in the scattering angle. For the 2D type (PL2 and CL2), the phase function is a function of zenith angle and the difference of the azimuth angles of the incident and scattered radiation. Therefore, 15 different phase functions were calculated for the incident angles corresponding to the discrete directions for quadrature points. Scattered energy was averaged over the solid angles, which were divided into 900 directions of the hemisphere[(30:from the zenith to the nadir) $\times$ (30:azimuth angle from 0 to π)]. For comparison purposes, spherical water particles are also calculated from Mie scattering theory (Deirmendjian, 1969). The refractive indices for ice and liquid water used in the present computation are shown in Table 3.1.

Figure 3.1 shows, for $\lambda = 0.63\,\mu$m, phase functions of (a) spherical water particles and (b) hexagonal ice crystals oriented randomly in space (3D) and mass equivalent ice spheres (LS). The phase functions of C1 and C2 are almost the same, whereas that of C3 is larger than those at $60° < \Theta < 120°$ and $150° < \Theta$. The phase function of LL is different from those of C1, C2, and C3 except for $15° < \Theta < 60°$. A sharp peak is noted at $\Theta \sim 140°$. Generally speaking, the phase function of ice crystals in the form of columns shows similar features to those in the form of plates. Remarkable peaks are shown at the scattering angle

Table 3.1 Refractive indices for ice and liquid water

Wavelength (μm)	Ice*	Water**
0.63	$1.309-i1.04\times10^{-8}$	$1.332-i1.44\times10^{-8}$
0.86	$1.304-i2.15\times10^{-7}$	$1.329-i3.29\times10^{-7}$
1.61	$1.289-i3.41\times10^{-4}$	$1.317-i8.69\times10^{-5}$

*Warren(1984), **Hale and Querry(1973)

Because of the small magnitude of the imaginary parts for 0.63 and 0.86 μm, they are assumed to be zero in the present study.

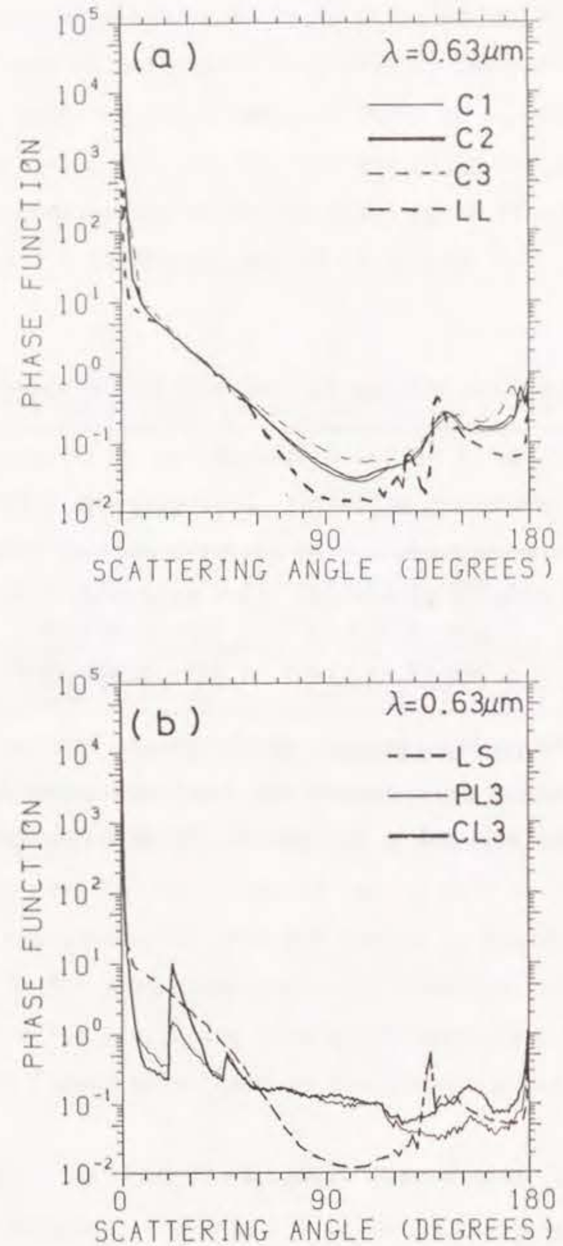

Fig.3.1 Phase functions of (a) spherical water cloud particles and (b) hexagonal ice crystals randomly oriented in space and mass equivalent ice spheres. $\lambda=0.63\,\mu m$.

(Θ) $\sim 22°$ and $\sim 46°$, which correspond to the halo phenomenon. However, there are differences of intensity near 22° halo and at $\Theta > 120°$. The phase function of LS is larger than those of CL3 for $\Theta < 60°$ except for the 22° halo, whereas it is smaller for $60° < \Theta < 120°$. It is similar to that of LL except for the small fluctuations at $100° < \Theta < 130°$, the sharp peak at $\Theta \sim 135°$, and the intensity at $\Theta > 150°$. Similar characteristics were shown for the phase functions of the larger particles (LL, LS, PL3, CL3) at $\lambda=0.86\,\mu m$ and $1.61\,\mu m$ (not shown). For the smaller particles (C1, C2, C3), the phase functions for $\lambda=0.86\,\mu m$ were similar to those for $\lambda=0.63\,\mu m$, but they showed differences to some extent for $\lambda=1.61\,\mu m$.

Figures 3.2(a) and (b) show examples of single scattering phase functions of hexagonal ice crystals with long axes randomly oriented in the horizontal plane (2D) for $\lambda=0.63\,\mu m$. Zenith angle of incident radiation is 60°; and azimuth difference, $\phi-\phi_0$, are 0°, 90°, and 180°, where ϕ_0 and ϕ are azimuth angle of the incident and scattered radiations, respectively. Optical phenomena caused by hexagonal ice crystals in 2D orientation are discussed in detail by Greenler (1980) and Takano and Liou (1989a). Intensity peaks corresponding to some of those phenomena are shown in Fig.3.2 by the symbols A-I. It should be noted that because 2D plates (PL2) turn on only one axis, the radiation could not be smoothed out. Consequently, the radiation is scattered into only limited directions.

3.3 Extinction Cross Section, Albedo for Single Scattering, and Asymmetry Factor

For 2D type, σ_e, ω_0 and $\langle\cos\Theta\rangle$ are functions of zenith angle of incident radiation. Figure 3.3 shows σ_e of the hexagonal ice crystals and mass equivalent spheres considered in the present work for $\lambda=0.63\,\mu m$. For the ice crystals, the efficiency factor is assumed to be 2.0. For the spheres, σ_e values are computed from Mie scattering theory, which are $1.963\times10^4\,\mu m^2$ and $1.969\times10^4\,\mu m^2$ for LL and LS, respectively. The σ_e values for the 2D ice crystals are equal to those for 3D ice crystals at $\theta_0 \sim 60°$.

Figures 3.4(a) and (b) are $\langle\cos\Theta\rangle$ for $\lambda=0.63\,\mu m$ and $1.61\,\mu m$,

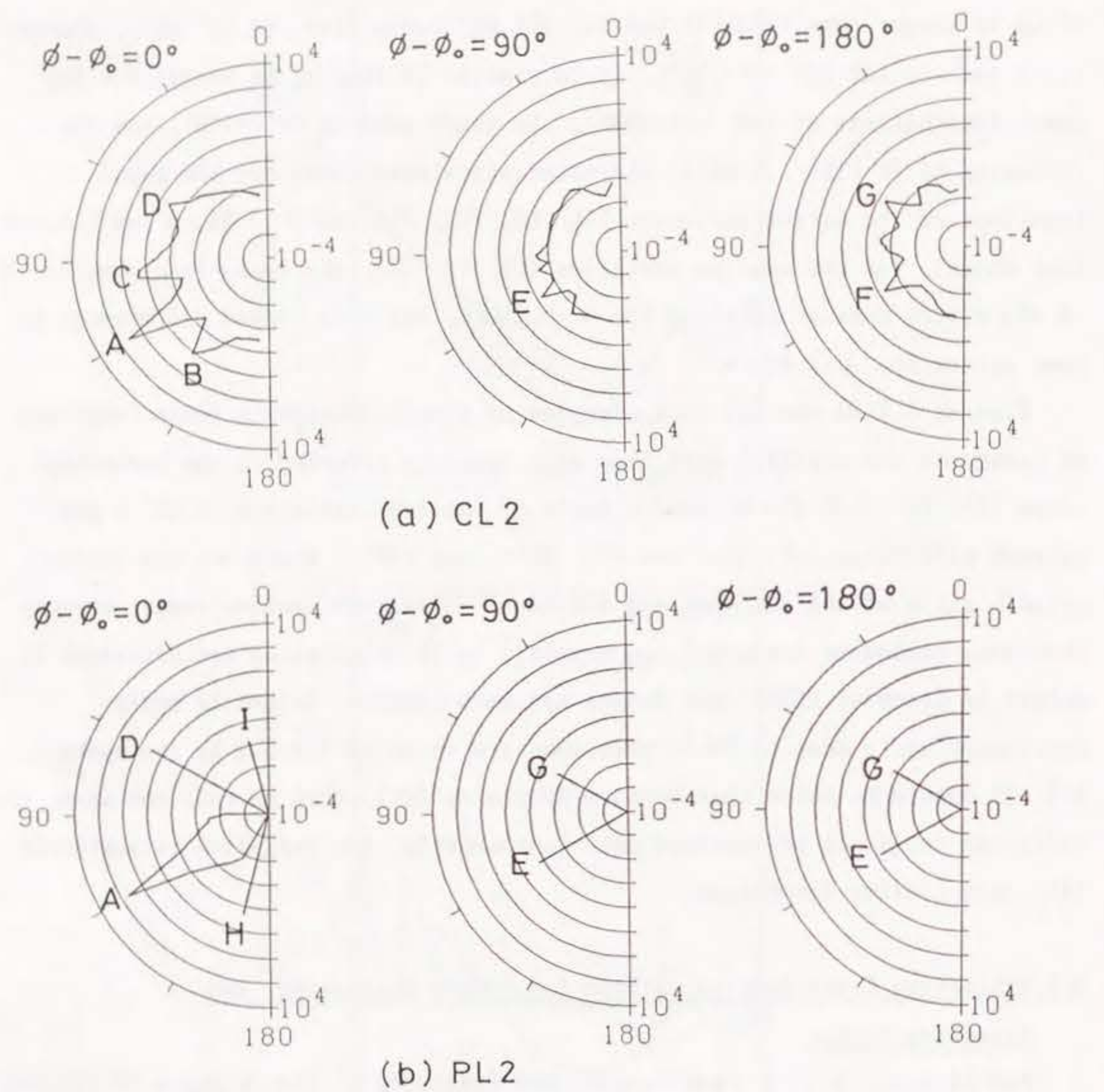

Fig.3.2 Phase functions of hexagonal ice crystals with long axes randomly oriented in the horizontal plane. (a) columns, (b) plates. $\lambda=0.63\,\mu m$. $\theta_0=60°$, $\phi-\phi_0=0°, 90°, 180°$.

A:diffraction peak, B:upper tangent arc, C:lower tangent arc, D:subsun, E:parhelic circle, F:antehelion and parhelic circle, G:subparhelic circle, H:circumzenithal arc, I:subcircumzenithal arc.

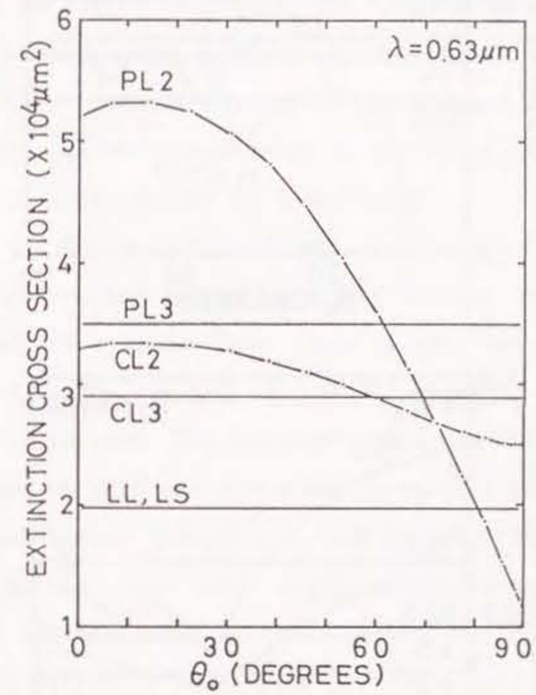

Fig.3.3 Extinction cross section (σ_e) of hexagonal ice crystals and mass equivalent ice and water spheres. Efficiency factor for hexagonal ice crystals is assumed to be 2.0. $\lambda=0.63\,\mu m$.

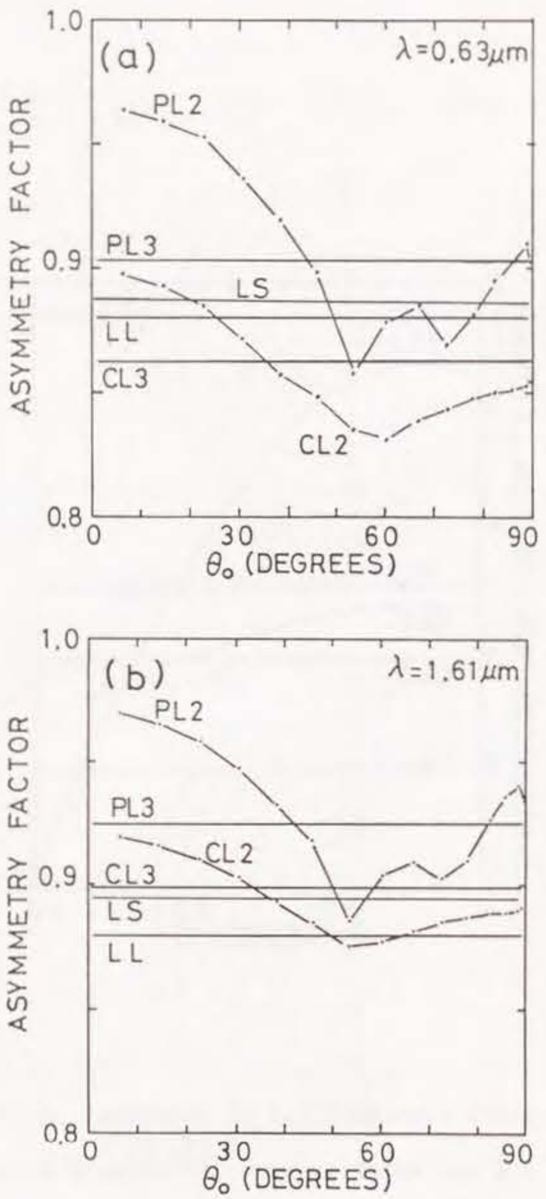

Fig.3.4 Asymmetry factor (⟨cosΘ⟩) of hexagonal ice crystals and mass equivalent ice and water spheres. (a) $\lambda=0.63\,\mu$m, (b) $\lambda=1.61\,\mu$m.

respectively. ⟨cosΘ⟩ for $\lambda=0.86\,\mu$m is similar to that for $\lambda=0.63\,\mu$m, therefore it is not shown. ⟨cosΘ⟩ for 2D ice crystals depends on the direction of incident radiation (θ_0), and especially ⟨cosΘ⟩ for 2D plates shows an irregular variation with θ_0. This is mainly attributed to the fact that the radiation, which is calculated by geometrical optics, is scattered to limited directions for the 2D plates (Fig.3.2). The ⟨cosΘ⟩ values for ice crystals are larger at $\lambda=1.61\,\mu$m than at $\lambda=0.63\,\mu$m. At $\lambda=1.61\,\mu$m, absorption occurs for ice crystals, and then the contribution of the forward diffraction becomes greater in the total radiation scattered by particles. Therefore, ⟨cosΘ⟩ becomes larger at $\lambda=1.61\,\mu$m than at $\lambda=0.63\,\mu$m.

Figure 3.5 is ω_0 for $\lambda=1.61\,\mu$m. The ω_0 values for ice crystals are smaller than those for water, which is mainly because the imaginary part of refractive index of ice is about four times larger than that of water at $\lambda=1.61\,\mu$m (Table 3.1). In Fig.3.5, ω_0 of PL2 suddenly decreases at $\theta_0\sim35°$; this is explained as follows. The incident radiation through the vertical side faces are attenuated in part and go to the horizontal bottom face. There, some of the radiation can emerge through the face for $\theta_0 < 35.6°$; consequently, it makes ω_0 larger. On the other hand, total reflection occurs there for $\theta_0 >$ 35.6° ,which makes ω_0 smaller.

Note that it is difficult to compute ω_0 precisely for $\lambda=0.63\,\mu$m and 0.86 μm because the imaginary parts of the refractive indices are almost zero (Table 3.1). In fact, 1.7% and 0.5% of incident radiations remained in the PL3 and CL3 ice crystals, respectively, after 8 internal reflections under the assumption of zero imaginary part of the refractive indices. Therefore, ω_0 of the ice crystals are assumed to be unity for 0.63 μm and 0.86 μm in the present computation. Similarly, Mie scattering computation in this chapter was carried out for the spherical particles with the zero imaginary part of refractive indices for $\lambda=0.63\,\mu$m and 0.86 μm. For comparison purposes, ω_0 were computed using the refractive indices shown in Table 3.1 for C1, C2, C3, LL, and LS. They were 1.00000 for all particles at $\lambda=0.63\,\mu$m and 0.999965, 0.999976, 0.999990, 0.999931, and 0.999952 for C1, C2, C3, LL, and LS, respectively, at $\lambda=0.86\,\mu$m. Relative difference between the monochromatic reflectances (Appendix

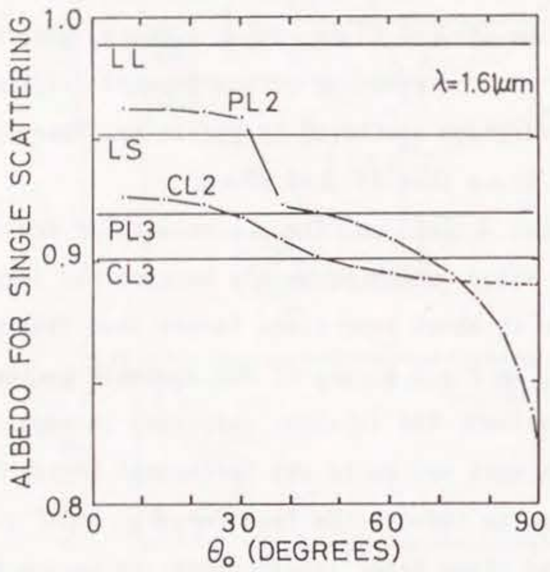

Fig.3.5 Albedo for single scattering (ω_0) of hexagonal ice crystals and mass equivalent ice and water spheres. λ=1.61 μm.

A) computed using unity of ω_0 and those computed using the above ω_0 were 0.94%, 0.89%, 0.74%, 0.67%, and 0.34% for C1, C2, C3, LL, and LS, respectively, under the condition of VWC=640gm^{-2} and θ_0=30°.

Chapter 4 Dependence of Shortwave Radiation Absorbed in the Ocean(I^{*}_{abs}) and Upward Irradiance at the Top of the Atmosphere ($I^{\uparrow}$) on Atmospheric and Oceanic Parameters - Cloudless Atmosphere -

4.1 Introduction

The radiation budget at the ocean surface is required for several research areas: (1) as a boundary condition for ocean models, (2) to understand the role of radiation in air-sea interactions, (3) to estimate meridional heat transport in the oceans, and (4) to validate coupled ocean-atmosphere models. The accuracy to which incoming shortwave irradiance must be known for such research areas is, for example, $\sim 10 Wm^{-2}$ for monthly averages in each 2° latitude by 10° longitude box in the tropical zone for the TOGA (Tropical Ocean and Global Atmosphere) project (WMO, 1984). Accuracy requirements for the surface radiation budget for WOCE (World Ocean Circulation Experiment) project is similar to that for TOGA (WMO, 1986).

For estimating the incident solar radiation at the ocean surface, empirical or simple physical formulae (bulk models) that are based on surface observations such as cloud amount and type have been widely used (Reed, 1977; Dobson and Smith, 1988; and others). However none of these formulae is able to achieve the $10 Wm^{-2}$ accuracy which is needed at a number of stations (Dobson and Smith, 1988). Methods based on satellite data to estimate shortwave irradiance on the earth's surface have recently been developed. These methods could be divided into two categories, statistical and physical. Statistical methods use empirical relationships derived from correlations between global radiation estimates from satellite data and those from nearby stations (Tarpley, 1979; and others). Results from these methods may be applicable only for particular areas. Methods based on physical models use satellite data as an indicator of which parameters are necessary for calculations of the radiation using radiative transfer models (Gautier, Diak, and Masse, 1980; Diak and Gautier, 1983; Möser and Raschke, 1983,; and others). The accuracy of the incident shortwave irradiance computed by methods that use physical models is, for example, $30 Wm^{-2}$ for the monthly mean values at noon by Möser and Raschke

(1983). These physical models use simple equations or a two-stream approximation to calculate the radiation, which may be one of the sources of the error of the inferred irradiances.

Theoretical studies of radiation budgets have been reported for an atmosphere-cloud model bounded by a Lambertian surface (Freeman and Liou, 1979). Nakajima and Tanaka (1983) evaluated the transfer of solar radiation in the model atmosphere-ocean system and discussed the dependence of reflectivity at the top and just above the ocean surface on the wind speed and optical properties of the atmosphere and ocean. Rao and Takashima (1986) examined the effect of the eruption of the volcano El Chichon on the shortwave irradiance (0.285-2.5μm) at the top and bottom of the atmosphere bounded by a Lambert surface.

It is the purpose of this chapter to search for an appropriate method to estimate I^{*}_{abs} from space by simulating radiative transfer process in a model atmosphere-ocean system (Masuda and Takashima, 1988). As a first step, dependence of I^{*}_{abs} and the upward irradiance at the top of the atmosphere ($I^{\uparrow}$) on various atmospheric and oceanic parameters is computed using a model atmosphere-ocean system under cloudless condition.

4.2 Spectral Distribution of Solar Radiation

We have computed the shortwave irradiances between 0.285μm and 5.0μm (Appendix A) at the top and just above the ocean in a realistic model of a cloud-free, plane-parallel, vertically inhomogeneous atmosphere-ocean system (Fig.4.1). The parameters used in this model have been described in Chapter 2. The accuracy requirement for shortwave irradiance at the ocean surface is specified for monthly averaged incoming irradiance ($I^{*}\downarrow$) (WMO, 1984, 1986). Here, the net irradiance, I^{*}_{abs}(=$I^{*}\downarrow$-$I^{*}\uparrow$), is also required for the climatological application. In this thesis, therefore, the accuracy of the I^{*}_{abs} is investigated for space observations. The extraterrestrial solar spectrum has been compiled by Iqbal (1983). We have divided the extraterrestrial solar spectrum from 0.285μm to 2.5μm into 83 unequal intervals over each of which the optical properties of the atmosphere are assumed to remain constant (Rao

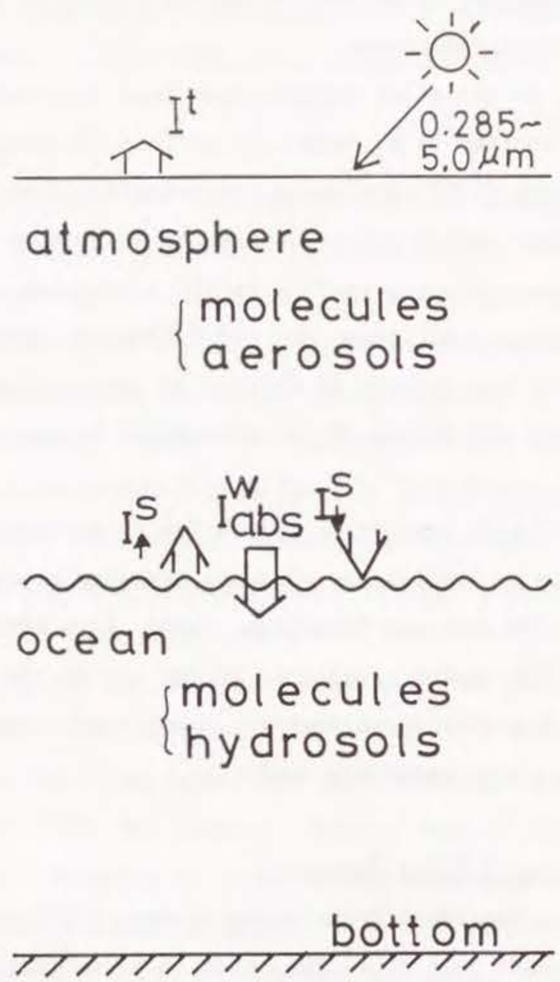

Fig.4.1 Diagram showing the atmosphere-ocean system.
The upward irradiances in the spectral region (0.285-5.0μm) are computed at the top (I^t) and just above the surface ($I^s\uparrow$), together with the downward irradiance just above the surface ($I^s\downarrow$). I^w_{abs} represents the radiation absorbed in the ocean, which is defined by $I^s\downarrow - I^s\uparrow$.

and Takashima, 1986). Beyond 2.5μm, the interval of 0.1μm is adopted.

First, a comparison of reflectivity just above the ocean surface (defined by $I^s\uparrow/I^s\downarrow$) computed by the present study with those by Nakajima and Tanaka(1983) was carried out as a function of the solar zenith angle θ_0 for nonaerosol model with v=7.49m/s. The refractive index of hydrosols is m=1.16-i0.0 (medium turbid condition; Fig.4.2). A general trend of reflectivity in the present study agreed well with those of Nakajima and Tanaka (1983). The case of a Lambert surface with a reflectivity of 0.0602, which is the average reflectivity of the above mentioned ocean model, is also shown as a reference.

Figure 4.3 shows the wavelength dependence of the total optical thickness of molecules and aerosols in the wavelength region (0.285-5.0μm). The case of the clear condition ($\tau^a_{sct}+\tau^a_{abs}$=0.25 at λ=0.555μm) is shown, where τ^m_{sct} and τ^m_{abs} represent molecular optical thickness due to scattering and absorption processes, respectively, whereas, τ^a_{sct} and τ^a_{abs} correspond to those of aerosol scattering and absorption. τ^m_{abs} exhibits spectral characteristics according to the absorption bands mainly water vapor and ozone, whereas τ^m_{sct} decreases monotonically with increase of wavelength; beyond 1μm, it is practically negligible. For the oceanic aerosols, τ^a_{sct} is reasonably independent of wavelength, whereas τ^a_{abs} is small in the spectral region considered here, except at 3μm (τ^a_{abs}=0.1). For the water soluble aerosols, τ^a_{sct} decreases monotonically with increase of wavelength and τ^a_{abs} ranges from 0.001 to 0.01 for almost entire wavelength region considered in this thesis.

Figure 4.4 shows spectral distributions of the incident solar radiation (I^{sol}) and the upward irradiance (I^t) at the top of the atmosphere, the downward ($I^s\downarrow$) and upward ($I^s\uparrow$) irradiances just above the ocean surface, and the radiation absorbed in the ocean ($I^w_{abs}=I^s\downarrow-I^s\uparrow$) for solar zenith angle θ_0 =45.8° . The incident solar irradiance normal to the incident direction is 1351.9Wm^{-2} for 0.285-5.0μm (98.9% of the solar constant of 1367Wm^{-2}, Iqbal, 1983), so that the irradiance normal to the horizontal plane becomes 942.4Wm^{-2} for θ_0=45.8° . The atmosphere is the clear aerosol model in the case of the oceanic type aerosols with the surface wind v=5m/s without whitecaps. Furthermore, the ocean is free from hydrosols. For simplicity, this model

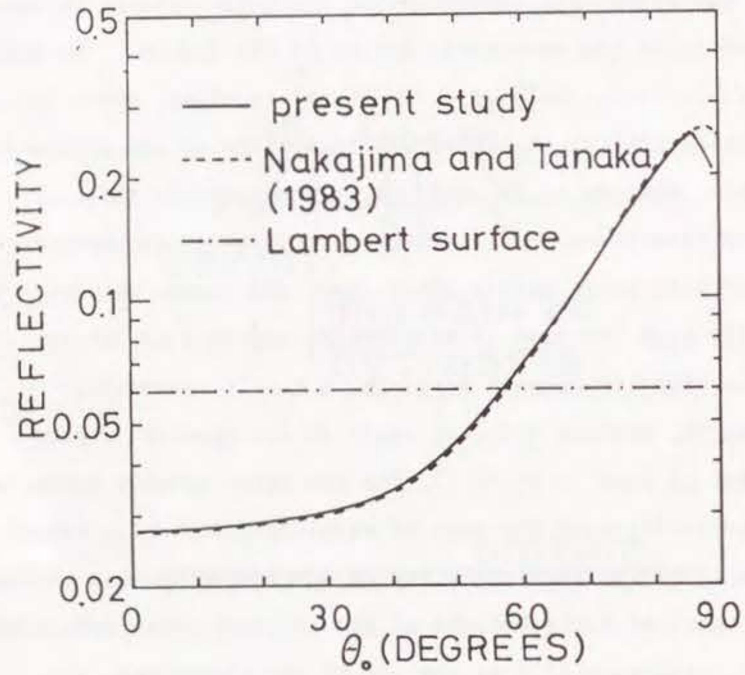

Fig. 4.2 Total reflectivities for solar radiation just above the ocean surface for atmosphere-ocean system with no aerosols, v=7.49m/s, and purely scattering hydrosol (m=1.16-i0.0) in the medium turbid condition. The case of the Lambert surface of reflectivity of 0.0602 is also shown.

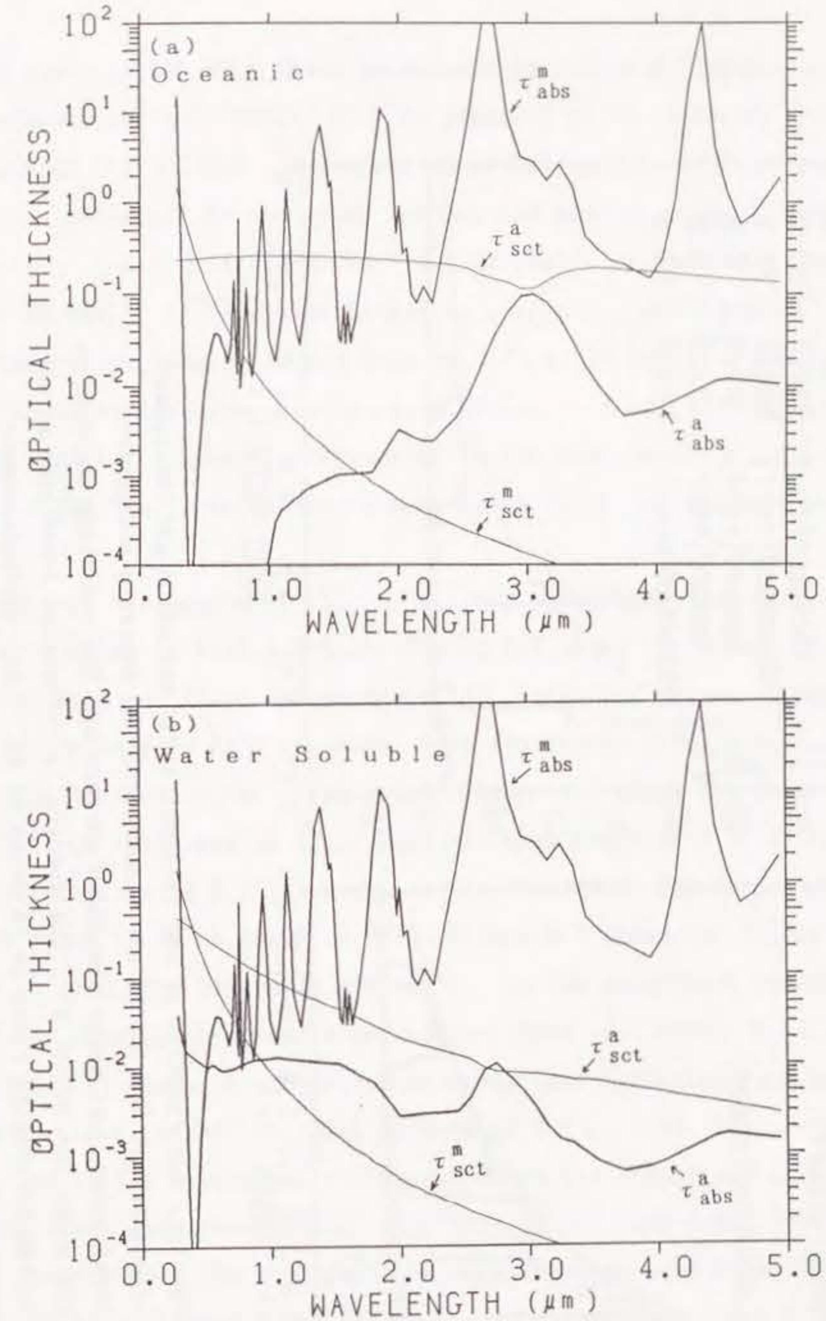

Fig. 4.3 Wavelength dependence of the total optical thickness of (a) oceanic aerosols and (b) water soluble aerosols (clear condition); the total optical thickness of molecules is also shown.

τ^a_{sct} : scattering by aerosols, τ^a_{abs} : absorption by aerosols,

τ^m_{sct} : scattering by molecules, τ^m_{abs} : absorption by molecules.

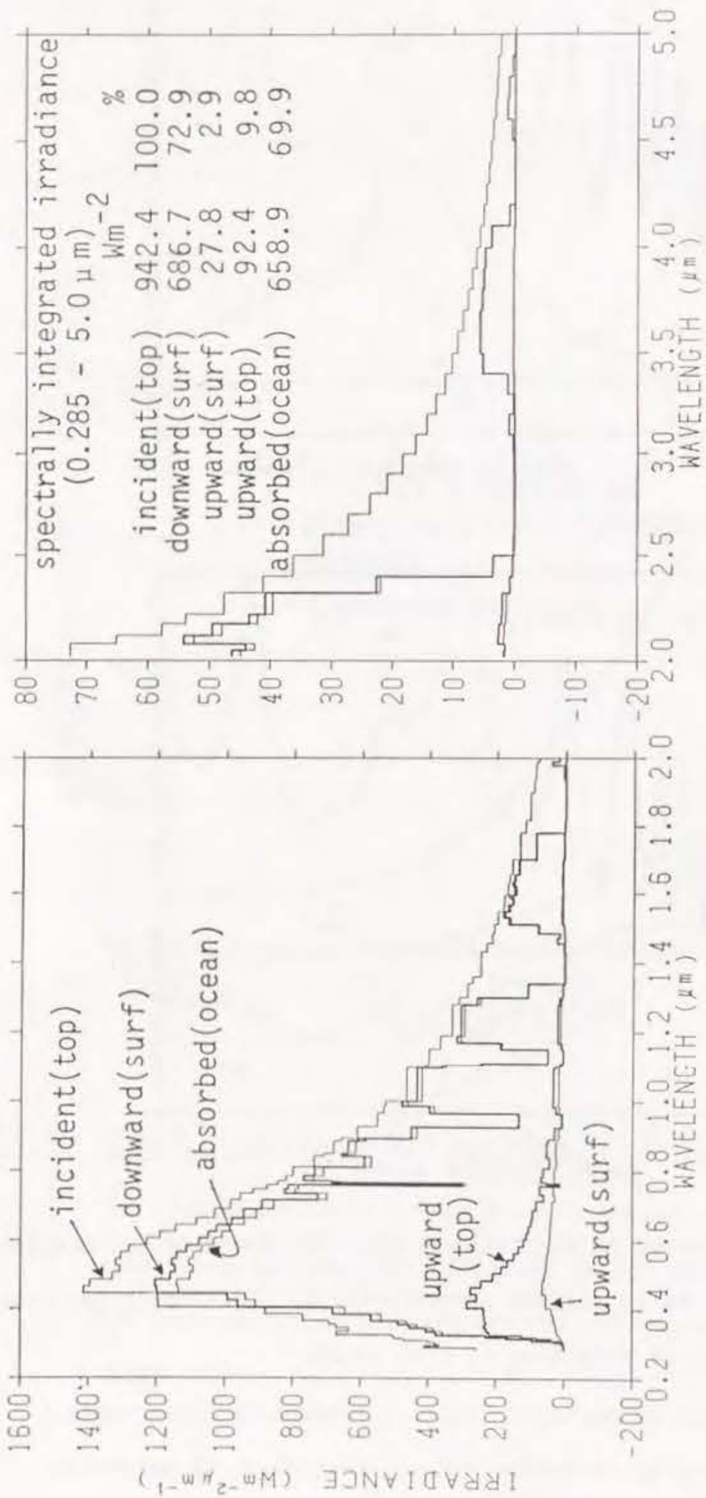

Fig. 4.4 Spectral distribution of the incident solar radiation and the upward irradiance at the top of the atmosphere, the downward and upward irradiances just above the ocean surface and the radiation absorbed in the ocean for θ_0=45.8°. The spectrally integrated irradiance normal to the horizontal plane is in units of Wm^{-2} (mid-latitude summer atmosphere, oceanic aerosol model with clear condition, v=5m/s, no whitecaps and no hydrosols: RAOS in the text).

atmosphere-ocean system with these parameters is called a "reference atmosphere-ocean system" (RAOS). $I^s\downarrow$ is composed of the directly transmitted solar radiation ($I^s_{dr}\downarrow$) and the diffuse skylight ($I^s_{df}\downarrow$). $I^s\uparrow$ is composed of the radiation reflected by the ocean surface and the radiation transmitted from the ocean. $I^s\downarrow$ and $I^s\uparrow$ are 686.7Wm^{-2} and 27.8Wm^{-2} , respectively, whereas I^t amounts to 92.4Wm^{-2}. $I^s\uparrow$ is significant only in the visible region. I^*_{abs} is large in the region ranging from 0.4μm to 0.7μm. It exhibits small absorption in the ocean at wavelengths λ=0.75μm, 0.95μm, 1.15μm, 1.4μm, 1.8-2.0μm, 2.5-3.4μm, and 4.2-4.5μm, corresponding to the atmospheric absorption bands. I^*_{abs} becomes 658.9Wm^{-2}, which corresponds to 69.9% of the incident solar irradiance.

The spectral dependence of I^*_{abs} on various atmospheric and oceanic parameters is shown in Figs.4.5-4.10. Figure 4.5 shows the effect of the surface wind speed on I^*_{abs}, the change of I^*_{abs} with the change of the surface wind speed from 5m/s to 8m/s is shown. Here the change of I^*_{abs} is 0.3Wm^{-2} (0.03% of the incident solar irradiance). Figure 4.6 shows the gross estimation of the effect of whitecaps on I^*_{abs}. Here whitecap coverage S is 0.24% at v=5m/s and the reflectivity is 0.45 as mentioned in Chapter 2. The effect of whitecaps on I^*_{abs} is found to be -0.6Wm^{-2} (0.07%). Figure 4.7 shows the effect of hydrosols on I^*_{abs}. The hydrosols affect I^*_{abs} in the wavelength region up to about 0.8μm. When the hydrosol's refractive index is 1.07-i0.01 ($\omega_0\sim$0.7), I^*_{abs} increases slightly in comparison with the case excluding such hydrosols (RAOS). When their refractive index is 1.16-i0.0 (ω_0=1.0), I^*_{abs} decreases with the turbidity of the hydrosols. Figure 4.8 shows the comparison of I^*_{abs} in the case of the clear atmosphere (RAOS) with that of the hazy condition. I^*_{abs} decreases greatly when the atmosphere becomes the hazy condition. The effect of the amount of precipitable water vapor on I^*_{abs} is shown in Fig.4.9. With the 20% increase of water vapor from 2.98cm to 3.58cm, I^*_{abs} decreases by 6.6Wm^{-2} (0.70%). Similarly an examination for ozone is shown in Fig.4.10. I^*_{abs} increases by 1.0Wm^{-2} (0.10%) with a 10% decrease of ozone from 0.324atm-cm to 0.298 atm-cm.

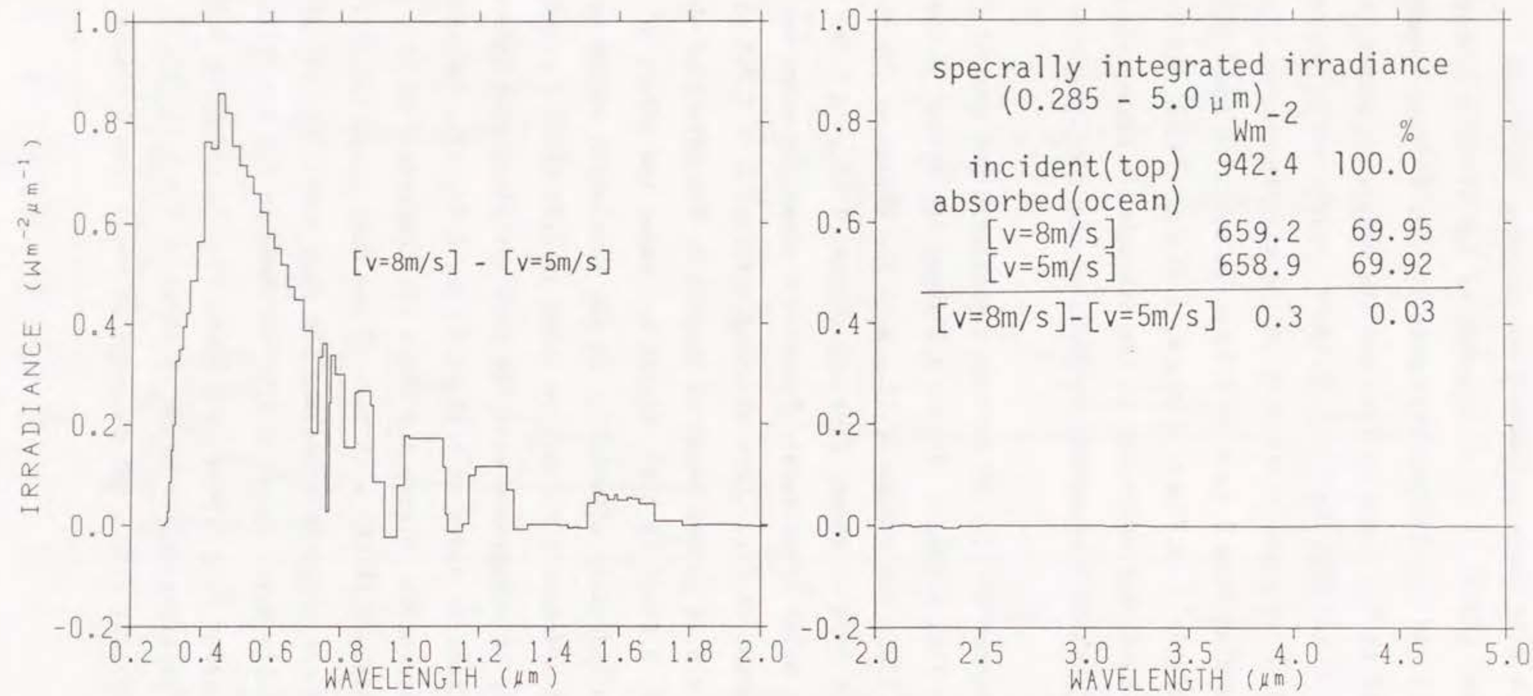

Fig. 4.5 Effect of the surface wind speed on the radiation absorbed in the ocean. The ordinates shows the change of the absorbed radiation resulted from changing the parameter from v=5m/s to 8m/s. Parameters except wind are in the RAOS. θ_0=45.8° .

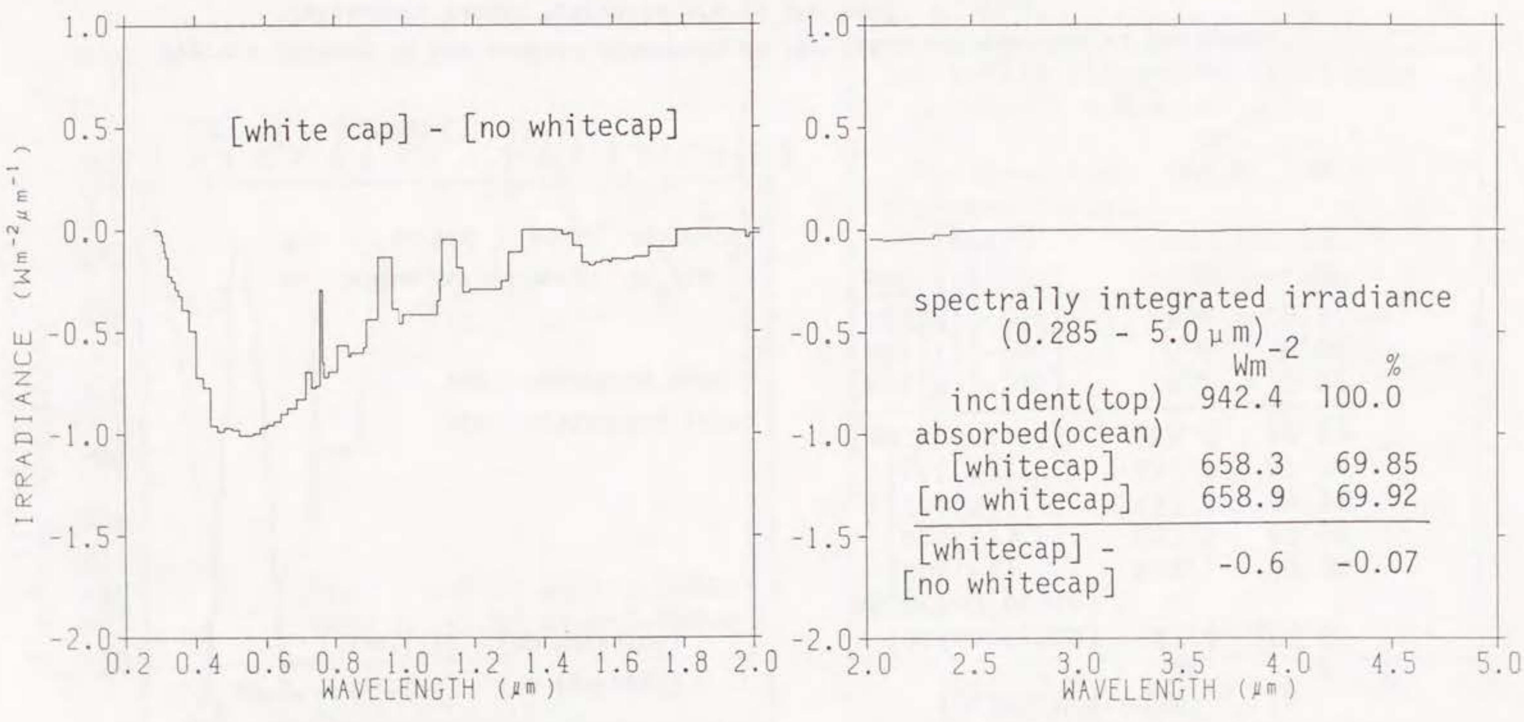

Fig. 4.6 Effect of the whitecaps on the radiation absorbed in the ocean. The ordinates shows the change of the absorbed radiation resulted from including the effect of the whitecaps in the system. Parameters except whitecaps are in the RAOS. θ_0=45.8° .

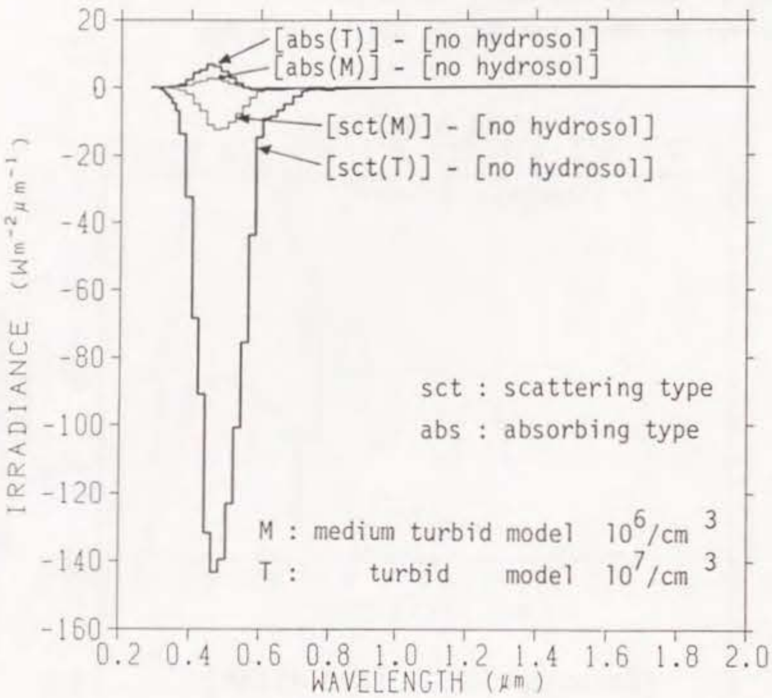

spectrally integrated irradiance (0.285 - 5.0 μm)

	Wm^{-2}	%
incident(top)	942.4	100.0
absorbed(ocean)		
[abs(M)]	659.1	69.94
[abs(T)]	659.5	69.98
[sct(M)]	657.3	69.75
[sct(T)]	638.4	67.74
[no hydrosol]	658.9	69.92
[abs(M)]-[no]	0.2	0.02
[abs(T)]-[no]	0.6	0.06
[sct(M)]-[no]	-1.6	-0.17
[sct(T)]-[no]	-20.5	-2.18

Fig.4.7 Effect of the oceanic hydrosols on the radiation absorbed in the ocean. Parameters except hydrosols are in the RAOS. θ_0=45.8° .

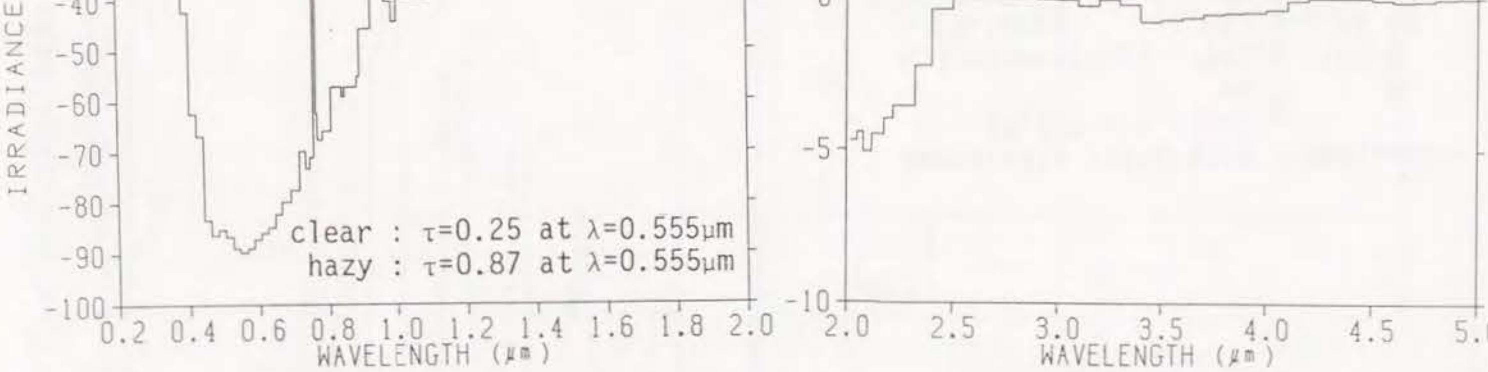

Fig.4.8 Effect of the atmospheric condition on the solar radiation absorbed in the ocean. Parameters except hydrosols are in the RAOS.
The difference resulting from changing atmospheric condition from clear to hazy condition for the oceanic aerosols is shown. θ_0=45.8° .

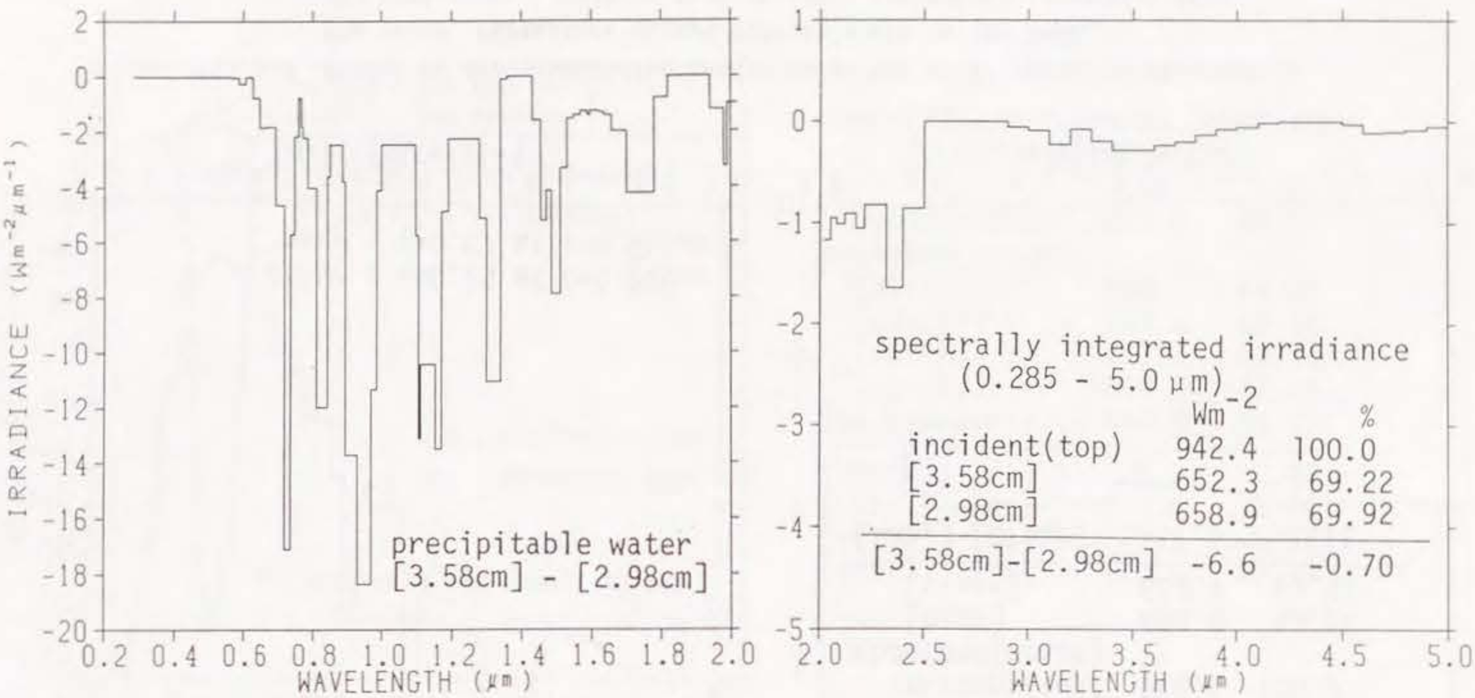

Fig.4.9 Effect of the amount of the water vapor on the solar radiation absorbed in the ocean. Parameters except water vapor are in the RAOS. The difference resulting from changing the amount from 2.98 cm to 3.58cm is shown. θ_0=45.8° .

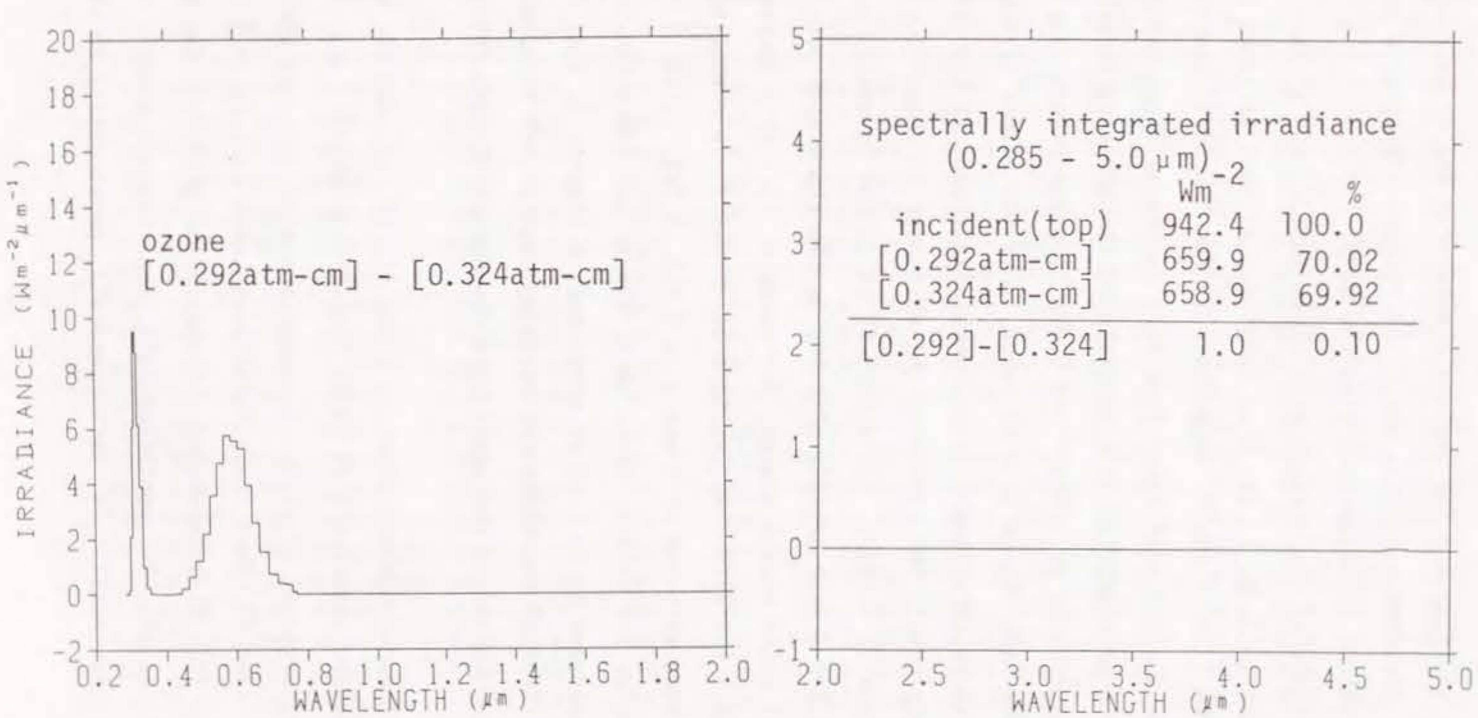

Fig.4.10 Effect of the amount of ozone on the solar radiation absorbed in the ocean. Parameters except ozone are in the RAOS. The difference resulting from changing the amount from 0.324 atm-cm to 0.292 atm-cm is shown. θ_0=45.8° .

4.3 Dependence of I^{*}_{abs} and I' on Atmospheric and Oceanic Parameters

Dependence of I^{*}_{abs} and I' on atmospheric and oceanic parameters for five θ_0 values is summarized in Table 4.1. Spectrally integrated irradiances for θ_0 =45.8° are shown in Table 4.2 for various atmospheric and oceanic conditions. In this section, dependence of I^{*}_{abs} and I' on various atmospheric and oceanic parameters is examined in comparison with the RAOS.

First, the effect of the surface wind speed on I^{*}_{abs} and I' is discussed on reference to lines 1, 3, 5, 7, and 9 in Table 4.1 without whitecap effect. I^{*}_{abs} increases by 1.0Wm^{-2} and 7.2Wm^{-2}, respectively, for θ_0=14.4° and 72.4° with the change of the surface wind speed from 2m/s to 14m/s. These values are less than 10Wm^{-2}, which is suggested as a guidance of the accuracy for the measurement. I' decreases by 1.0Wm^{-2} and 5.7Wm^{-2}, respectively, for θ_0=14.4° and 72.4° with the same change of wind speed. Thus the effect of the isotropic surface wind on these irradiances is not very significant if the effect of the whitecaps were neglected. The effect of the whitecaps is shown in lines 1-10. When the wind speed is $<$10m/s, the effect of whitecaps is small, but when it is $>$10m/s, I^{*}_{abs} and I' are greatly affected by the whitecaps, particularly in the case of small solar zenith angles. For example, I^{*}_{abs} (I') decreases (increases) by 28.1 (24.9)Wm^{-2} for v=14m/s at θ_0=14.4° in comparison with no whitecap cases. Here whitecap coverage S is 0.01%, 0.24%, 1.15%, 3.28%, and 7.27%, respectively, for v=2m/s, 5m/s, 8m/s, 11m/s, and 14m/s (Eq.2.7). The reflectivity is assumed to be 0.45 as mentioned in Chapter 2. When v is so large that the effect of the whitecaps may play significant role, more detailed reflectivity value including the wavelength dependency (Koepke,1984) should be used.

The effect of hydrosols are shown in Lines 11, 12, 13, and 14. When the hydrosol's refractive index is 1.07-i0.01 [abs(M) and abs(T): $\omega_0 \sim 0.7$], I^{*}_{abs} (I') increases (decreases) slightly in comparison with the case excluding such hydrosols (RAOS: line 3). When their refractive index is 1.16-i0.0 [sct(M) and sct(T): ω_0=1.0], I^{*}_{abs} (I') decreases (increases) slightly for the medium turbid condition [sct(M): 10^6 particles/cm^3], but they are greatly affected for the turbid condition [sct(T): 10^7 particles/cm^3], particularly in the case of

Table 4.1 Spectrally integrated irradiances (I^{*}_{abs} and I') as a function of the solar zenith angle

	H_2O (cm)	O_3 (atm-cm)	Aerosols		Wind (m/s)	Whitecap	Hydrosol	I^{*}_{abs}* Solar Zenith Angle 14.4°	30.4°	45.8°	60.0°	72.4°	I'* Solar Zenith Angle 14.4°	30.4°	45.8°	60.0°	72.4°
(1)	2.98	0.324	oceanic	clear	2.0	no	no	986.9	858.4	658.6	422.8	204.8	92.6	91.7	92.7	95.9	90.7
(2)	2.98	0.324	oceanic	clear	2.0	yes	no	986.9	858.3	658.6	422.7	204.8	92.6	91.8	92.8	95.9	90.7
(3)**	2.98	0.324	oceanic	clear	5.0	no	no	987.3	858.7	658.9	424.0	207.6	92.3	91.5	92.4	94.7	88.5
(4)	2.98	0.324	oceanic	clear	5.0	yes	no	986.3	857.9	658.3	423.6	207.4	93.1	92.2	93.0	95.0	88.7
(5)	2.98	0.324	oceanic	clear	8.0	no	no	987.5	858.9	659.2	425.3	209.4	92.0	91.2	92.1	93.5	87.0
(6)	2.98	0.324	oceanic	clear	8.0	yes	no	983.1	855.0	656.3	423.5	208.6	95.9	94.7	94.7	95.2	87.8
(7)	2.98	0.324	oceanic	clear	11.0	no	no	987.7	859.0	659.6	426.5	210.8	91.8	91.1	91.6	92.5	85.9
(8)	2.98	0.324	oceanic	clear	11.0	yes	no	975.1	848.0	651.3	421.2	208.4	103.0	100.9	99.1	97.3	88.2
(9)	2.98	0.324	oceanic	clear	14.0	no	no	987.9	859.1	660.1	427.5	212.0	91.6	90.9	91.2	91.7	85.0
(10)	2.98	0.324	oceanic	clear	14.0	yes	no	959.8	834.8	641.6	415.8	206.4	116.5	112.6	107.9	102.4	90.2
(11)	2.98	0.324	oceanic	clear	5.0	no	sct(M)	985.3	856.8	657.3	422.8	207.0	94.2	93.3	94.0	95.8	89.1
(12)	2.98	0.324	oceanic	clear	5.0	no	abs(M)	987.7	859.0	659.1	424.1	207.7	91.9	91.1	92.2	94.5	88.4
(13)	2.98	0.324	oceanic	clear	5.0	no	sct(T)	960.1	833.9	638.4	409.8	200.2	118.8	115.8	112.4	108.6	95.7
(14)	2.98	0.324	oceanic	clear	5.0	no	abs(T)	988.3	859.5	659.5	424.4	207.8	91.3	90.6	91.8	94.3	88.3
(15)	2.98	0.324	oceanic	hazy	5.0	no	no	934.7	803.1	601.0	371.2	173.5	136.2	138.3	142.3	142.6	123.1
(16)	2.98	0.324	water soluble	clear	5.0	no	no	970.2	841.7	642.9	410.7	199.0	95.5	94.9	95.5	96.0	86.1
(17)	2.98	0.324	water soluble	hazy	5.0	no	no	875.7	746.8	551.6	334.4	152.7	143.8	144.9	145.4	139.1	113.7
(18)	0.87	0.324	oceanic	clear	5.0	no	no	1036.0	903.2	696.2	451.4	223.7	94.6	94.0	95.4	98.7	93.3
(19)	3.58	0.324	oceanic	clear	5.0	no	no	978.6	850.8	652.3	419.1	204.7	91.8	91.0	91.9	93.9	87.6
(20)	4.20	0.324	oceanic	clear	5.0	no	no	970.5	843.4	646.1	414.6	201.9	91.4	90.6	91.3	93.3	86.8
(21)	2.98	0.162	oceanic	clear	5.0	no	no	993.5	864.6	664.3	428.6	211.1	94.6	93.9	94.9	97.4	91.4
(22)	2.98	0.292	oceanic	clear	5.0	no	no	988.4	859.8	659.9	424.9	208.3	92.7	91.9	92.9	95.2	89.0
(23)	2.98	0.648	oceanic	clear	5.0	no	no	976.7	848.6	649.6	415.9	201.3	89.0	88.1	88.8	90.6	83.9
(24)	2.98	0.324	oceanic	clear	Lambert surface (r=0.0598)			957.4	834.6	645.9	425.6	217.1	118.0	112.5	104.1	94.1	81.1
(25)***								1309.5	1165.6	942.4	675.9	409.5	1309.5	1165.6	942.4	675.9	409.5

*Irradiance are in units of Wm^{-2}.

**Results for the RAOS.

***The irradiance of the incident solar radiation.

Table 4.2 Spectrally integrated irradiance for $\theta_0=45.8°$

	H_2O (cm)	O_3 (atm-cm)	Aerosols		Wind (m/s)	Whitecap	Hydrosol	$I^{t\downarrow}$	$I^{s}_{dr}\downarrow$	$I^{s}_{df}\downarrow$	$I^{s}\downarrow$	$I^{s}\uparrow$	I^{t}	I^{s}_{abs}	I^{a}_{abs}	I_{abs} *
(1)	2.98	0.324	oceanic	clear	2.0	no	no	942.4	459.8	227.1	686.9	28.3	92.7	658.6	191.1	849.6
(2)	2.98	0.324	oceanic	clear	2.0	yes	no	942.4	459.8	227.1	686.9	28.3	92.8	658.6	191.1	849.6
(3)**	2.98	0.324	oceanic	clear	5.0	no	no	942.4	459.8	227.0	686.7	27.8	92.4	658.9	191.1	850.0
(4)	2.98	0.324	oceanic	clear	5.0	yes	no	942.4	459.8	227.0	686.8	28.5	93.0	658.3	191.1	849.4
(5)	2.98	0.324	oceanic	clear	8.0	no	no	942.4	459.8	226.9	686.7	27.5	92.1	659.2	191.1	850.3
(6)	2.98	0.324	oceanic	clear	8.0	yes	no	942.4	459.8	227.3	687.1	30.8	94.7	656.3	191.4	847.7
(7)	2.98	0.324	oceanic	clear	11.0	no	no	942.4	459.8	226.9	686.7	27.0	91.6	659.6	191.1	850.8
(8)	2.98	0.324	oceanic	clear	11.0	yes	no	942.4	459.8	227.9	687.7	36.4	99.1	651.3	191.9	843.2
(9)	2.98	0.324	oceanic	clear	14.0	no	no	942.4	459.8	226.9	686.6	26.5	91.2	660.1	191.1	851.2
(10)	2.98	0.324	oceanic	clear	14.0	yes	no	942.4	459.8	229.1	688.9	47.3	107.9	641.6	192.9	834.5
(11)	2.98	0.324	oceanic	clear	5.0	no	sct(M)	942.4	459.8	227.3	687.1	29.8	94.0	657.3	191.1	848.4
(12)	2.98	0.324	oceanic	clear	5.0	no	abs(M)	942.4	459.8	226.9	686.7	27.5	92.2	659.1	191.1	850.2
(13)	2.98	0.324	oceanic	clear	5.0	no	sct(T)	942.4	459.8	231.3	691.1	52.7	112.4	638.4	191.5	830.0
(14)	2.98	0.324	oceanic	clear	5.0	no	abs(T)	942.4	459.8	226.8	686.6	27.1	91.8	659.5	191.1	850.6
(15)	2.98	0.324	oceanic	hazy	5.0	no	no	942.4	186.8	443.9	630.7	29.7	142.3	601.0	199.1	800.1
(16)	2.98	0.324	water soluble	clear	5.0	no	no	942.4	508.7	161.1	669.8	26.9	95.5	642.9	204.0	846.9
(17)	2.98	0.324	water soluble	hazy	5.0	no	no	942.4	286.5	291.0	577.4	25.9	145.4	551.6	245.4	797.0
(18)	0.87	0.324	oceanic	clear	5.0	no	no	942.4	487.2	238.3	725.5	29.3	95.4	696.2	150.7	847.0
(19)	3.58	0.324	oceanic	clear	5.0	no	no	942.4	455.0	224.9	679.9	27.6	91.9	652.3	198.2	850.5
(20)	4.20	0.324	oceanic	clear	5.0	no	no	942.4	450.4	223.0	673.5	27.3	91.3	646.1	204.9	851.0
(21)	2.98	0.162	oceanic	clear	5.0	no	no	942.4	463.0	229.4	692.4	28.1	94.9	664.3	183.2	847.5
(22)	2.98	0.292	oceanic	clear	5.0	no	no	942.4	460.4	227.4	687.8	27.9	92.9	659.9	189.6	849.5
(23)	2.98	0.648	oceanic	clear	5.0	no	no	942.4	453.9	223.1	677.0	27.4	88.8	649.6	204.0	853.6
(24)	2.98	0.324	oceanic	clear	Lambert surface (r=0.0598)			942.4	459.8	227.2	687.0	41.1	104.1	645.9	192.3	838.3

* Irradiance are in units of Wm^{-2}. Parameters $I^{t\downarrow}$, I^{t}, $I^{s}_{dr}\downarrow$, $I^{s}_{df}\downarrow$ and $I^{s}\downarrow$ represent incident solar and upward irradiance at the top of the atmosphere, respectively, downward irradiance at the surface, direct and diffuse components, respectively, and their sum. $I^{s}\uparrow$ represents the upward irradiance at the surface. Parameters I^{s}_{abs}, I^{a}_{abs}, and I_{abs} represent radiation absorbed in the ocean and in the atmosphere and their sum.

** Results for the RAOS.

small solar zenith angles. For example, I^{s}_{abs} (I^{t}) decreases (increases) by 27.2 (26.5)Wm^{-2} at $\theta_0=14.4°$ in comparison with RAOS. Thus only when the hydrosols are purely scattering under a turbid condition, should the effect of the hydrosols on I^{s}_{abs} and I^{t} be taken into account.

The effect of aerosols are shown in Lines 3, 15, 16, and 17. I^{s}_{abs} and I^{t} are largely affected by the turbidity of the aerosols; both for the oceanic and water soluble aerosols. For the change from clear to hazy conditions, I^{s}_{abs} decreases by 52.6Wm^{-2} and 94.5Wm^{-2}, respectively, for the oceanic and the water soluble aerosols at $\theta_0=14.4°$; 34.1Wm^{-2} and 46.3Wm^{-2} at $\theta_0=72.4°$. I^{t} increases by 43.9Wm^{-2} and 48.3Wm^{-2}, respectively, for the oceanic and the water soluble aerosols at $\theta_0=14.4°$; 34.6Wm^{-2} and 27.6Wm^{-2} at $\theta_0=72.4°$. The difference of I^{s}_{abs} and I^{t} due to types of aerosols (lines 3 and 16 for the clear condition 15 and 17 for the hazy condition) cannot be neglected particularly for I^{s}_{abs}. Thus an appropriate aerosol model should be prepared for the investigation of I^{s}_{abs} and I^{t}.

The effect of the amount of precipitable water vapor on I^{s}_{abs} and I^{t} is shown in lines 3, 18, 19, and 20. To cover the range of climatic variabilities in the tropics and midlatitudes, the water vapor amounts for midlatitude winter and tropical model in LOWTRAN6 (Kneizys et al., 1983) are used for lines 18 and 20, respectively. I^{t} changes slightly with the change of precipitable water from 0.87cm to 4.2cm. However, I^{s}_{abs} is greatly affected by the amount of precipitable water. Roughly speaking, the sensitivity of I^{s}_{abs} to the amount of precipitable water is 20Wm^{-2}, 15Wm^{-2}, and 7Wm^{-2} per 1 cm, respectively, for θ_0 =14.4° ,45.8° , and 72.4° within the range of precipitable water considered here. Thus the accuracy better than 0.5 cm of precipitable water is desired for estimation of I^{s}_{abs} for the accuracy better than 10Wm^{-2}.

The effect of the ozone on I^{s}_{abs} and I^{t} is shown in lines 3, 21, 22, and 23. Ozone amount in RAOS is multiplied by factors 0.5 and 2.0, respectively, for lines 21 and 23. I^{t} changes slightly with the change of amount of ozone from 0.162 atm-cm to 0.648 atm-cm. I^{s}_{abs} is fairly affected by the amount of ozone. Roughly speaking, the sensitivity of I^{s}_{abs} to the amount of ozone is 4Wm^{-2}, 3Wm^{-2}, and 2Wm^{-2} per 0.1 atm-cm, respectively, for $\theta_0=14.4°$,45.8° , and 72.4°

within the range of ozone amount considered here. Thus, the accuracy of 0.1 atm-cm of ozone amount is enough for estimation of I^{w}_{abs} for the accuracy better than $10 Wm^{-2}$.

So far effect of the stratospheric aerosols was not considered. Radiation Commission (1986) used aerosol particles which consist of a 75% solution of sulfuric acid in water as the stratospheric aerosol model. The size distribution is represented by the modified gamma function (Eq.2.4), where parameters (a, α, b, γ) are (324.0, 1.0, 18, 1.0). This aerosol model was inserted in RAOS. The optical thickness of stratospheric aerosol was selected following the Radiation Commission (1986) with minor change (τ =0.001744 and 0.003 for the layers of 13-20km and 20-30km, respectively, at λ=0.555μm). These values are for the normal condition without volcanic stratospheric aerosols. The increase (decrease) of I^{t} (I^{w}_{abs}) due to the stratospheric aerosols were < $0.5 Wm^{-2}$ for the solar zenith angles considered here.

As for the solar zenith angles θ_0, I^{w}_{abs} is a strong function of θ_0 and decreases monotonically. For example, it is $987.3 Wm^{-2}$, $658.9 Wm^{-2}$, and $207.6 Wm^{-2}$ respectively for θ_0=14.4°, 45.8°, and 72.4° for the RAOS. In the zenith angles ranging from 30.4° to 60.0°, I^{w}_{abs} changes $14.7 Wm^{-2}$ per degree on the average. Thus a precise solar zenith angles is also required for the remote investigation of I^{w}_{abs}. The dependence of I^{t} on θ_0 is smaller than that of I^{w}_{abs}. For the RAOS, it is $92.3 Wm^{-2}$, $92.4 Wm^{-2}$, and $88.5 Wm^{-2}$ respectively for θ_0 =14.4°, 45.8°, and 72.4°.

As stated earlier, the atmosphere aerosols and precipitable water mostly affects I^{w}_{abs} and I^{t}. Therefore the usefulness of the model atmosphere bounded by a Lambert surface (MAL) is examined by neglecting the detail contribution of the oceanic parameters. The result for a Lambert surface of reflectivity of 0.0598, which is the average reflectivity of the ocean model in RAOS, is also shown in line 24. For θ_0=60.0°, I^{w}_{abs} and I^{t} differ only $1.6 Wm^{-2}$ and $0.6 Wm^{-2}$, respectively from the corresponding values in RAOS. Thus this MAL is practical for θ_0=60.0°. However, for θ_0 away from 60.0°, there are larger differences numerically between RAOS and MAL models. For θ_0=14.4°, I^{w}_{abs} and I^{t} differ $29.9 Wm^{-2}$ and $25.7 Wm^{-2}$, respectively in the above comparisons. Thus in this

case, an appropriate value of reflectivity should be introduced.

To search for an appropriate method for evaluating I^{w}_{abs} from satellite measurements, the computational results are examined using Table 4.2 for θ_0 =45.8° as follows. I^{t}, I^{w}_{abs}, and the radiation absorbed in the atmosphere (I^{a}_{abs}) change by $49.9 Wm^{-2}$, $-57.9 Wm^{-2}$ and $8.0 Wm^{-2}$, respectively, with the change of the atmospheric condition from the clear to the hazy condition for the oceanic aerosols (line 3 and 15); $-0.5 Wm^{-2}$, $-6.6 Wm^{-2}$ and $7.1 Wm^{-2}$, respectively, with a 20% increase of water vapor amount (line 3 and 19); $0.5 Wm^{-2}$, $1.0 Wm^{-2}$ and $-1.5 Wm^{-2}$, respectively, with a 10% decrease of ozone amount (line 3 and 22). Purely scattering hydrosols in the turbid condition affect I^{t}, I^{w}_{abs}, and I^{a}_{abs} by $20.0 Wm^{-2}$, $-20.5 Wm^{-2}$, and $0.4 Wm^{-2}$ (line 3 and 13), respectively. The ocean surface condition exhibits little effect on I^{t}, I^{w}_{abs}, and I^{a}_{abs} when surface wind speed is <10m/s. Therefore, I^{w}_{abs} may be roughly evaluated using I^{t} obtained from satellite measurements by neglecting I^{a}_{abs}. But in this procedure, I^{a}_{abs} remains as an error. To improve the accuracy of I^{w}_{abs}, therefore, I^{a}_{abs} should be simultaneously evaluated. I^{a}_{abs} is affected by water vapor and ozone amount, but I^{t} is not very sensitive to their change. Water vapor and ozone amount may be evaluated using their strong spectral characteristics. However, I^{a}_{abs} is also affected by the atmospheric aerosols, so their effect should be estimated as well. In evaluating aerosol characteristics using I^{t}, I^{t} is also affected greatly by purely scattered hydrosols under turbid condition. Thus to refine the accuracy of measuring I^{w}_{abs}, a precise investigation of the optical characteristics and turbidity of hydrosols would also be required.

To validate I^{w}_{abs} derived from satellite measurements, it may be compared with that measured from ship. More precisely, the atmospheric and oceanic parameters used for deriving I^{w}_{abs} from satellite measurements should also be compared with those measured from ship. For this purpose, dependence of $I^{s}\uparrow$ and $I^{s}\downarrow$ on the various atmospheric and oceanic parameters is examined using Table 4.2 for θ_0=45.8°. $I^{s}\downarrow$ exhibits a strong dependence on the atmospheric condition. It is $686.7 Wm^{-2}$ and $630.7 Wm^{-2}$, respectively in the clear and hazy conditions for the oceanic aerosols (line 3 and 15), showing that with the corresponding atmospheric change, the directly transmitted solar radiation decreases by 273.0Wm^{-2}, whereas the diffusely transmitted radiation increases by 216.9Wm^{-2}. The other parameters do not show any significant change of $I^s\downarrow$. The purely scattering hydrosols affect the diffuse skylight (4.4Wm^{-2} in the turbid condition: lines 3 and 13), whereas they do not affect the directly transmitted radiation. Thus to derive the atmosphere turbidity, combined measurements of the directly and diffusely transmitted radiations might be preferable. The upward irradiance just above the ocean, $I^s\uparrow$ mainly exhibits dependence on the characteristics and turbidity of hydrosols. If they are purely scattering type under the turbid condition, $I^s\uparrow$ increases by 24.9Wm^{-2} (lines 3 and 13), whereas, $I^s\uparrow$ decreases by 0.7Wm^{-2} with hydrosols which are partially absorptive type(lines 3 and 14). The change of atmospheric condition from clear to hazy increases $I^s\uparrow$ by 1.9Wm^{-2} (lines 3 and 15). Therefore the purely scattering hydrosols could be evaluated using $I^s\uparrow$ but the partially absorbing hydrosols seem to be difficult to evaluate precisely using $I^s\uparrow$.

4.4 Summary and Conclusions

The present computation in the atmosphere-ocean system show the following results. (1) Absorbed radiation in the ocean (I^w_{abs}) and irradiance at the top of the atmosphere (I^t) depends mainly on the atmospheric turbidity. For the change from clear to hazy conditions, I^w_{abs} decreases by 52.6Wm^{-2} and 94.5Wm^{-2}, respectively, for the oceanic and the water soluble aerosols at θ_0=14.4° ; 34.1Wm^{-2} and 46.3Wm^{-2} at θ_0=72.4° . I^t increases by 43.9Wm^{-2} and 48.3Wm^{-2}, respectively, for the oceanic and the water soluble aerosols at θ_0=14.4° ; 34.6Wm^{-2} and 27.6Wm^{-2} at θ_0=72.4° . Different aerosols types also affect I^w_{abs}. (2) Precipitable water also affects I^w_{abs}, but have little effect on I^t. Roughly speaking, the sensitivity of I^w_{abs} to the amount of precipitable water is 20Wm^{-2}, 15Wm^{-2}, and 7Wm^{-2} per 1 cm, respectively, for θ_0=14.4° , 45.8° , and 72.4° within the range of precipitable water from 0.87cm to 4.20cm. (3) Ozone amount has some effect on I^w_{abs}, but very little I^t. Roughly speaking, the sensitivity of I^w_{abs} to the amount of ozone is 4Wm^{-2}, 3Wm^{-2}, and 2Wm^{-2} per 0.1 atm-cm, respectively, for θ_0=14.4° ,45.8° , and 72.4° within the range of ozone amount from 0.162 atm-cm to 0.648 atm-cm. (4) The surface roughness

without whitecaps shows little effect on I^w_{abs} and I^t. (5) Whitecaps affect I^w_{abs} and I^t by >10Wm^{-2} when v >10m/s, particularly in cases of small solar zenith angles. (6) The oceanic hydrosols show little effect on I^w_{abs} and I^t, except when they are of the pure scattering type in a turbid condition. For example, I^w_{abs} (I^t) decreases (increases) by 27.2 (26.5)Wm^{-2} θ_0=14.4° in comparison with no hydrosol case.

I^w_{abs} may be roughly evaluated using I^t obtained from satellite observations by neglecting absorption by the atmospheric constituents (I^a_{abs}), but in this procedure I^a_{abs} remains as an error. Therefore, to improve the accuracy of I^w_{abs}, I^a_{abs} should be evaluated simultaneously. Here I^a_{abs} is affected by water vapor and ozone amount, where these effects could be evaluated using their strong spectral characteristics. However I^a_{abs} is affected by the atmospheric aerosols, and their effect should be estimated as well. Moreover, a precise investigation of the optical characteristics and turbidity of hydrosols would also be required to improve the accuracy of I^w_{abs}. To validate I^w_{abs} derived from satellite observations, the atmospheric and oceanic parameters should also be compared with those derived by ship. The effect of the cloud layer on I^w_{abs} and I^t is discussed in the next Chapter.

Chapter 5 Dependence of Shortwave Radiation Absorbed in the Ocean(I^w_{abs}) and Upward Irradiance at the Top of the Atmosphere (I^t) on Cirrus Cloud Parameters

5.1. Introduction

In the previous chapter, dependence of shortwave radiation absorbed in the ocean (I^w_{abs}) and upward irradiance at the top of the atmosphere (I^t) on atmospheric and oceanic parameters is computed under cloudless condition. For improvement a method to estimate I^w_{abs} and I^t from space, it is desired that simulation of the radiation field should be carried out using more realistic models that include cloud models. As for cloud, cirrus is located at high altitudes, thus it plays an important role in the Earth radiation budget. The cirrus cloud is in general composed of crystals in various shapes. Recently the effects of the shape and orientation of the hexagonal ice crystals on solar radiation were examined by Takano and Liou (1989b) and Masuda and Takashima (1989) using the doubling-adding method.

In this chapter, first, dependence of I^w_{abs}, together with I^t, on cirrus cloud parameters is estimated using a realistic plane-parallel, vertically inhomogeneous atmosphere-ocean model in which a cirrus cloud layer is included (Masuda and Takashima, 1990b). The effects of the thermodynamic phase of the cloud particles and the shape and orientation of the hexagonal ice crystals on I^w_{abs} and I^t are examined especially where the hexagonal ice crystals are assumed to be (1) randomly oriented in the space or (2) randomly oriented with their long axis in the horizontal plane. Further, a method to infer I^w_{abs} and I^t from the NOAA-AVHRR radiometer, together with its accuracy, are discussed.

5.2 Computational Method

The upward irradiance at the top of the atmosphere (I^t) and radiation absorbed in the ocean (I^w_{abs}) defined by $I^s\downarrow - I^s\uparrow$ were computed for the atmosphere-ocean model including cirrus cloud layer. Diagram showing the atmosphere-ocean system is shown in Fig.5.1. In addition to the "reference

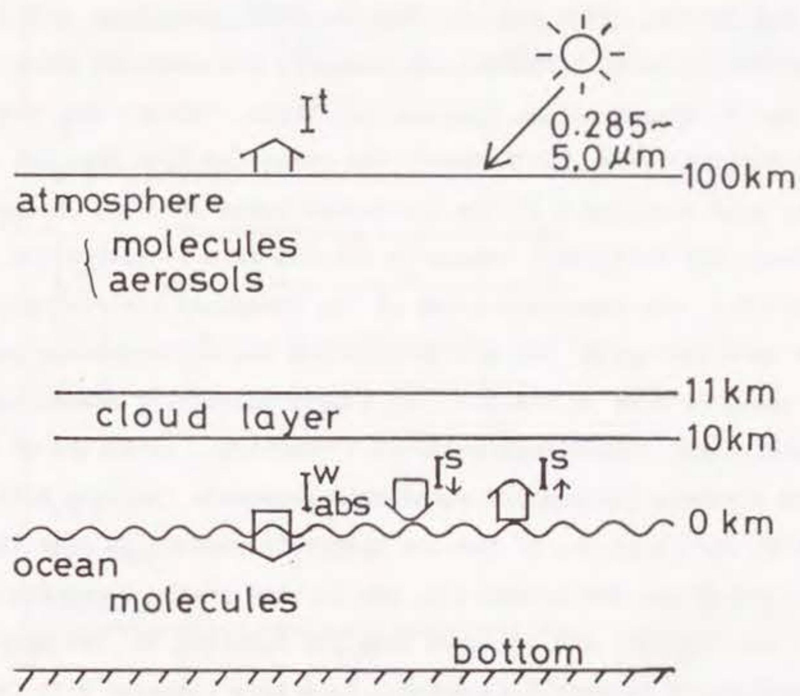

Fig.5.1 Diagram showing the atmosphere-ocean system.
I^t : Upward irradiance at the top of the atmosphere.
$I^s\uparrow$: Upward irradiance just above the ocean surface.
$I^s\downarrow$: Downward irradiance just above the ocean surface.
I^w_{abs}: Radiation absorbed in the ocean which is defined by $I^s\downarrow - I^s\uparrow$.

atmosphere-ocean system" (RAOS) used in Chapter 4, a cirrus cloud layer is included in the layer between 10km and 11km. Cloud models and single scattering properties of cloud particles have been described in Chapters 2 and 3, respectively. The vertical optical thicknesses of the cloud layer together with aerosols and molecules are shown in Fig.5.2. The refractive indices of liquid water (Hale and Querry, 1973) and ice (Warren, 1984) are shown in Fig.5.3.

The phase functions of hexagonal ice crystals are computed using the geometrical optics approximation (Chapter 3). These computations, however, consume much computer time. Furthermore, the phase function does not vary significantly with wavelength if the refractive index does not change very much. Therefore, the wavelength region is divided into 10 subregions, which are shown in Table 5.1, and phase functions of the hexagonal ice crystals are computed for each subregion. The wavelengths and the corresponding refractive indices are shown by dots in Fig.5.3. The single scattering albedo (ω_0), on the other hand, might significantly affect I' and I^*_{abs}. Here, ω_0 of the hexagonal ice crystals for the 108 wavelength intervals (Section 4.2) are approximated by modifying ω_0 of the ice sphere (LS model) so that they are identical to ω_0 of the ice crystals at the 10 wavelengths where the phase functions of ice crystals are computed (see the Appendix B). The approximated ω_0 at 69 wavelengths between 0.4μm and 2.5μm were compared with the ω_0 computed using Eq.(12) in Takano and Liou (1989a). Means and standard deviations of the difference were (0.00056, 0.00452) and (-0.00267, 0.00930) for PL3 and CL3 models, respectively. Figure 5.4 shows ω_0 of PL3, CL3, ice spheres, and water spheres. The same procedure was applied for PL2 and CL2. Irradiances are first computed by the doubling-adding method for the 108 wavelengths, and then they are numerically integrated into broad band (0.285-5.0μm) irradiances.

Since the extinction cross section (σ^e), scattering cross section (σ^s), and albedo for single scattering ($\omega_0 = \sigma^s/\sigma^e$) depend on the direction of the incident radiation in the case of the hexagonal ice crystals randomly oriented with the long axis in the horizontal plane (Chapter 3), the basic equation describing the transfer of solar radiation should be modified.

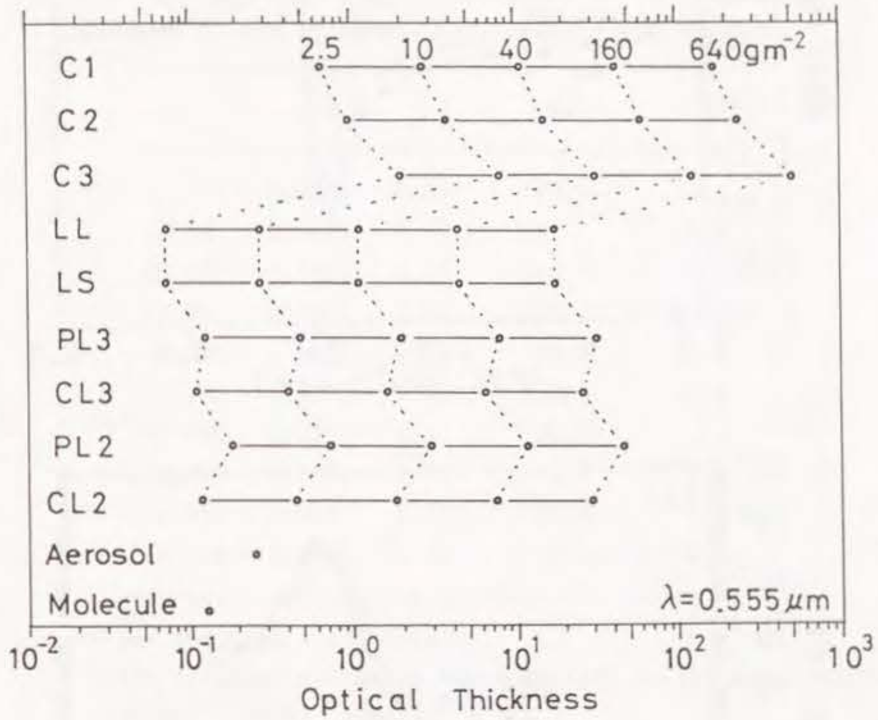

Fig.5.2 Vertical optical thicknesses of the cloud layer adopted in the present computation. Vertical water or ice content of cloud are assumed to be 2.5gm^{-2}, 10gm^{-2}, 40gm^{-2}, 160gm^{-2}, and 640gm^{-2}. Optical thickness of aerosols and molecules are also shown. The case of λ=0.555μm is shown.

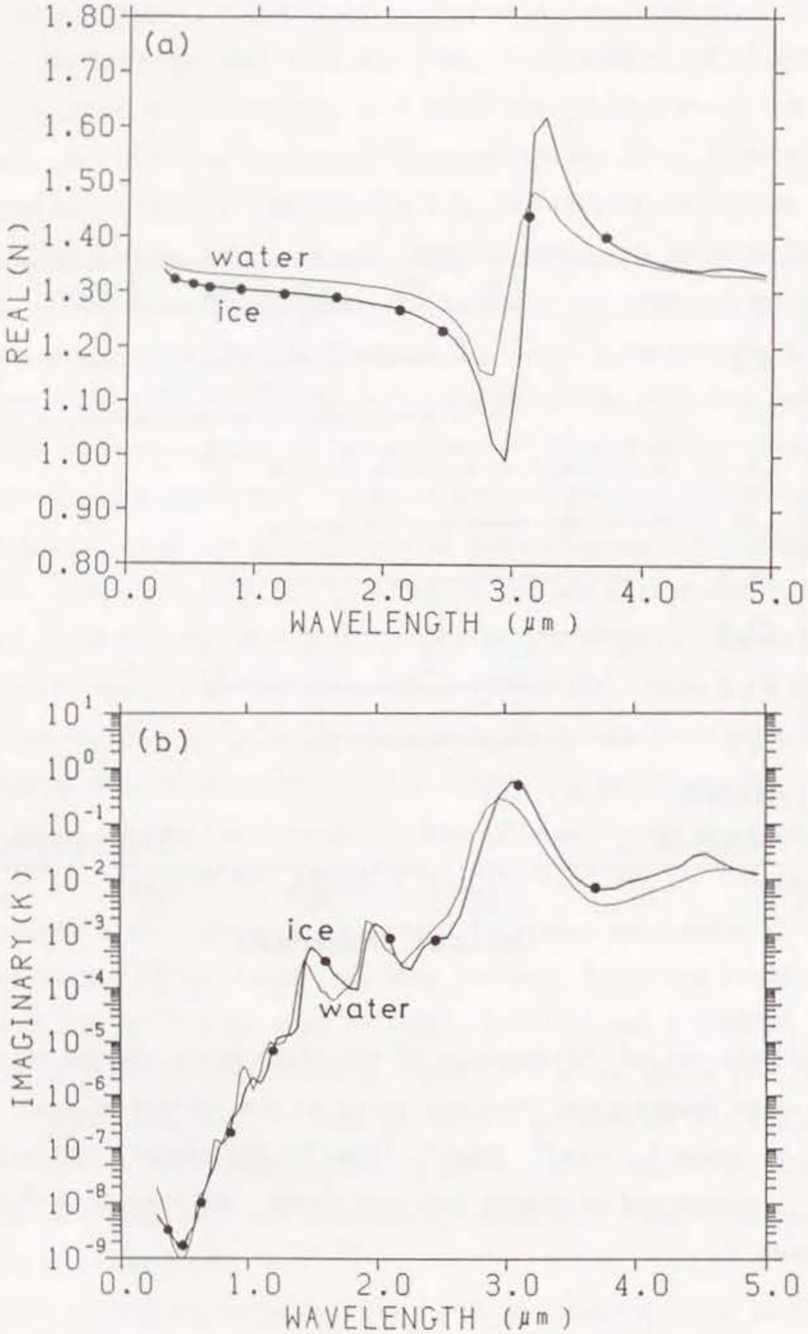

Fig.5.3 (a)Real and (b)imaginary parts of the refractive index of water (Hale and Querry, 1973) and ice (Warren, 1984). Dots show the wavelength where the phase functions of the hexagonal ice crystals are computed.

Table 5.1 Wavelength subregions and representative wavelengths where phase functions of the hexagonal ice crystals are computed

μm	μm	Wm^{-2}*	%**
(0.285 - 0.445)	0.37	177.9	13.0
(0.445 - 0.565)	0.50	231.7	16.9
(0.565 - 0.691)	0.63	208.6	15.3
(0.691 - 1.000)	0.86	322.1	23.6
(1.000 - 1.300)	1.20	168.6	12.3
(1.300 - 1.900)	1.61	155.5	11.4
(1.900 - 2.320)	2.10	39.8	2.9
(2.320 - 2.600)	2.46	14.4	1.1
(2.600 - 3.500)	3.10	22.3	1.6
(3.500 - 5.000)	3.70	11.1	0.8

*Solar spectral irradiance.

**Ratio of solar energy in the subregion to the solar constant ($1367Wm^{-2}$; Iqbal, 1983).

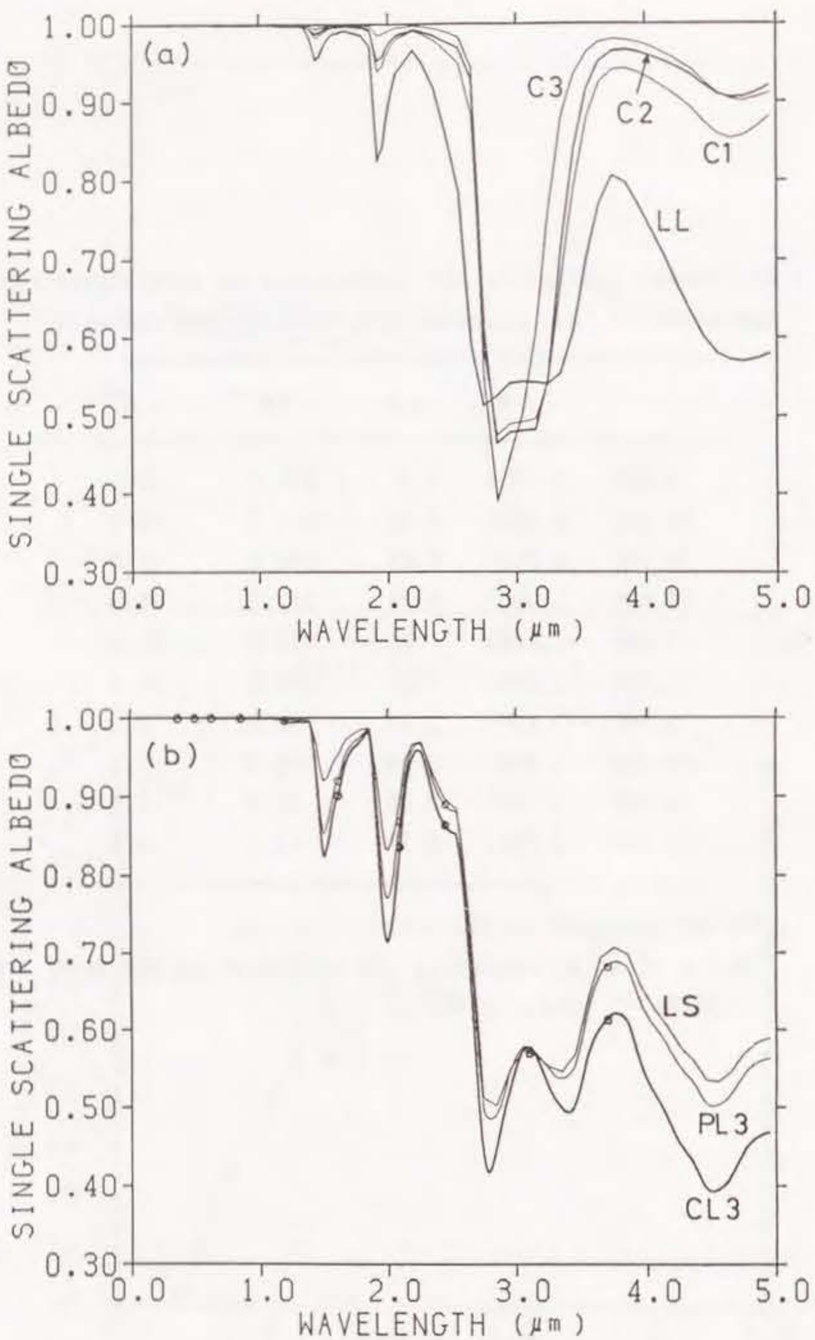

Fig.5.4 Single scattering albedo (ω_0) of the 3D type hexagonal ice crystals, ice sphere and water sphere cloud particles.
(a) C1, C2, C3, LL, (b) LS, PL3, CL3. In PL3 and CL3, circles and solid lines are, respectively, ω_0 from the geometrical optics approximation and those which are inferred based on them and the LS model values (see the Appendix B).

Consider a plane-parallel homogeneous atmospheric layer which contains n kind of particles such as molecules, aerosols, hexagonal ice crystals and so on. If the intensity of radiation I becomes $I+dI$ after traversing a thickness dz/μ in the direction of its propagation, then

$$
\begin{aligned}
dI(z,\Omega) = & -\sum_{i=1}^{n} N_i(z)\,\frac{dz}{\mu}\,\sigma_i^e(\mu)I(z,\Omega) \\
& +\sum_{i=1}^{n} N_i(z)\,\frac{dz}{\mu}\,\frac{1}{4\pi}\int_{4\pi}\sigma_i^s(\mu')P_i(\Omega,\Omega')I(z,\Omega')\,d\Omega' \\
& +\sum_{i=1}^{n} N_i(z)\,\frac{dz}{\mu}\,\frac{\sigma_i^s(-\mu_0)}{4\pi}P_i(\Omega,-\Omega_0)\,\pi F_0\,\exp\{-\int_{z}^{z_1}\sum_{i=1}^{n} N_i(z')\,\sigma_i^e(-\mu_0)\frac{dz'}{\mu_0}\}.
\end{aligned}
\tag{5.1}
$$

where N_i, σ_i^e, σ_i^s, and P_i are the number of particles per unit volume, extinction cross section, scattering cross section, and phase function of the ith component, respectively. $\Omega=(\mu,\phi)$ is the directional element of the solid angle that represents the pencil of radiation where μ and ϕ are cosine of the zenith angle and the azimuth angle, respectively, and $d\Omega=d\mu d\phi$. πF_0 is the flux density of incident solar radiation normal to its direction. z is the vertical path length measured upwardly, with z_1 being the top height of the layer. Note that σ_i^e and σ_i^s are functions of μ of incident radiation for nonspherical particles oriented randomly in a horizontal plane, and P_i is normalized to unity in the manner,

$$\frac{1}{4\pi}\int_{4\pi}P_i(\Omega,\Omega')\,d\Omega = 1. \tag{5.2}$$

In order to describe the transfer equation in terms of the optical thickness, we introduce a distribution function $m_i(\mu)$ according to Asano(1983), defined as

$$m_i(\mu)=\sigma_i^e(\mu)/\sigma_i^{e*}. \tag{5.3}$$

where σ_i^{e*} is the extinction coefficient associated with the vertical direction, i.e., $\sigma_i^{e*}=\sigma_i^e(\mu=1)$. Using $m_i(\mu)$, σ_i^{e*} and single scattering albedo, $\omega_{0i}(\mu)$, $\sigma_i^s(\mu)$ can be expressed as

$$\sigma_i^s(\mu)=\omega_{0i}(\mu)\,\sigma_i^e(\mu)=\omega_{0i}(\mu)\,\sigma_i^{e*}m_i(\mu). \tag{5.4}$$

Note that for nonspherical particles oriented randomly in a horizontal plane, $\sigma_i^e(-\mu)=\sigma_i^e(\mu)$, $\sigma_i^s(-\mu)=\sigma_i^s(\mu)$, $m_i(-\mu)=m_i(\mu)$, and $\omega_{0i}(-\mu)=\omega_{0i}(\mu)$ where $-\mu$ denotes a downward direction with a positive μ value varying between 0 and 1. For spherical particles or nonspherical particles oriented randomly in a space, these functions are independent of μ, and $m_i(\mu)=1$.
Total optical thickness of the layer is expressed as

$$\tau=\sum_{i=1}^{n}\tau_i\ , \tag{5.5}$$

where τ_i is the optical thickness of the ith component. Here, τ and τ_i are measured downwardly from the top of the layer($\tau=0$). By assuming homogeneity of the layer,

$$d\tau=\sum_{i=1}^{n}d\tau_i\ , \tag{5.6}$$

where

$$d\tau_i=-\sigma_i^{e*}N_i(z)dz\ , \tag{5.7}$$

$$d\tau/\sum_{i=1}^{n}m_i(\mu)d\tau_i=\tau/\sum_{i=1}^{n}m_i(\mu)\tau_i\ , \tag{5.8}$$ and

$$\sum_{i=1}^{n}m_i(\mu')\omega_{0i}(\mu')P_i(\Omega,\Omega')d\tau_i\ /\ \sum_{i=1}^{n}m_i(\mu)d\tau_i$$
$$=\sum_{i=1}^{n}m_i(\mu')\omega_{0i}(\mu')P_i(\Omega,\Omega')\ \tau_i\ /\ \sum_{i=1}^{n}m_i(\mu)\ \tau_i\ . \tag{5.9}$$

Using Eqs. (5.3) - (5.9), Eq.(5.1) can now be expressed as follows:

$$M(\mu)\frac{dI(\tau,\Omega)}{d\tau}=I(\tau,\Omega)-\frac{1}{4\pi}\int_{4\pi}WP(\mu,\phi;\mu',\phi')I(\tau,\Omega')d\Omega'$$
$$-\frac{1}{4\pi}WP(\mu,\phi;-\mu_0,\phi_0)\pi F_0\exp(-\tau/M(\mu_0)), \tag{5.10}$$

where $M(\mu)=\mu\tau\ /\ \sum_{i=1}^{n}m_i(\mu)\ \tau_i\ ,$ (5.11) and

$$WP(\mu,\phi;\mu',\phi')=\sum_{i=1}^{n}m_i(\mu')\omega_{0i}(\mu')P_i(\mu,\phi;\mu',\phi')\tau_i\ /\ \sum_{i=1}^{n}m_i(\mu)\tau_i$$
$$=\sum_{i=1}^{n}m_i(\mu')\omega_{0i}(\mu')P_i(\Omega,\Omega')\tau_i\ /\ \sum_{i=1}^{n}m_i(\mu)\tau_i. \tag{5.12}$$

Equation (5.10) is the same as the basic transfer equation for the optically

isotropic case of one particle component, for example Eq.(6.5) in Liou (1980), except for the replacement of terms μ and $\omega_0P(\Omega,\Omega')$ with $M(\mu)$ and $WP(\mu,\phi;\mu',\phi')$, respectively.

The phase function for cloud particles has a sharp forward peak. In order to properly account for this peak in numerical integrations, thousands of Fourier components are needed in the phase function expansion. To optimize the computational effort, the truncation procedure of the forward peak, which is similar to Takano and Liou (1989b), is adopted as follows:

$\delta_i=1-\dfrac{1}{4\pi}\displaystyle\int_{4\pi}P_i'(\Omega,\Omega')d\Omega$, where P_i' is the truncated phase function.

$P_i^*(\Omega,\Omega')=P_i'(\Omega,\Omega')/(1-\delta_i)$, $m_i^*(\mu)=m_i(\mu)(1-\delta_i\omega_{0i}(\mu))$,
$\omega_{0i}^*(\mu)=\omega_{0i}(\mu)(1-\delta_i)/(1-\delta_i\omega_{0i}(\mu))$.
$P_i(\Omega,\Omega')$, $m_i(\mu)$, and $\omega_{0i}(\mu)$ in Eqs. (5.11) and (5.12) are replaced by $P_i^*(\Omega,\Omega')$, $m_i^*(\mu)$, and $\omega_{0i}^*(\mu)$, respectively.

5.3 Dependence of I^*_{abs} and I^t on Cirrus Cloud Parameters

Figure 5.5 shows I^t and I^*_{abs} as a function of the solar zenith angle (θ_0). The cases of VWC=10gm^{-2} for C1, C2, and C3, and VWC=160gm^{-2} for LL, LS, PL3, CL3, PL2, and CL2, are shown. For comparison purposes, the cloudless case (RAOS in Chapter 4) is also shown. I^t for the cloudless case is almost the same as for θ_0<70° . On the other hand, I^*_{abs} monotonically decreases with θ_0. For example, I^t is 93Wm^{-2}, 91Wm^{-2}, and 95Wm^{-2}, respectively, for θ_0=6.3° , 30.4° , and 60.0° , whereas I^*_{abs} is 1018Wm^{-2}, 859Wm^{-2}, 424Wm^{-2}, respectively. In the cloudy cases, I^t is larger than that in the cloudless case, but an opposite trend is shown for I^*_{abs}. It should be noted that I^t and I^*_{abs} are not monotonical functions of optical thickness of the cloud layer (τ). For example, although τ for LL is larger than that for C2, I^t (I^*_{abs}) for LL is smaller (larger) than that for C2. Similar features are also seen between PL3 and CL3. This is because I^t and I^*_{abs} are also functions of ω_0 and the shape of the phase function (asymmetry factor as a first approximation) in addition to τ. For the 2D cases (PL2 and CL2), τ, ω_0 and the shape of the phase function depend on the direction of the incident radiation. Consequently, I^t and I^*_{abs}

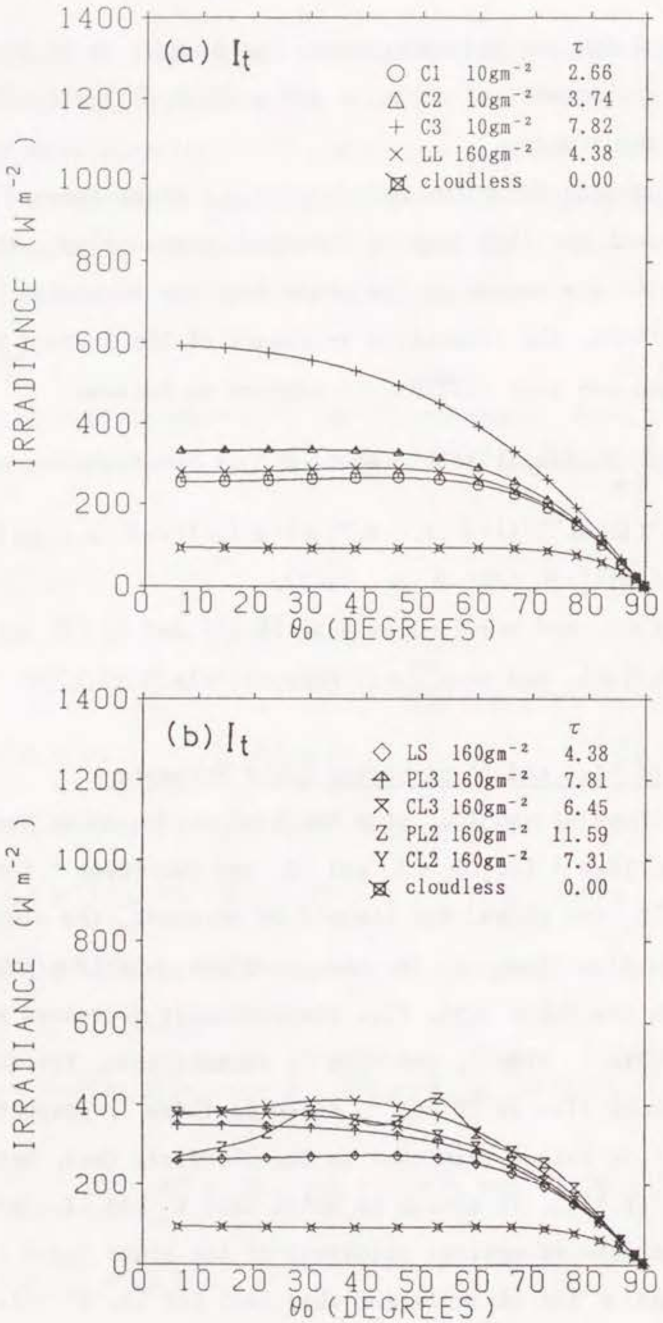

Fig.5.5 I_t(a and b) and I^w_{abs}(c and d) as a function of the solar zenith angle (θ_0).
τ : Vertical optical thicknesses of the cloud layer.
The cases of VWC=10gm^{-2} for C1, C2, and C3 and VWC=160gm^{-2} for LL, LS, PL3, CL3, PL2, and CL2 are shown.

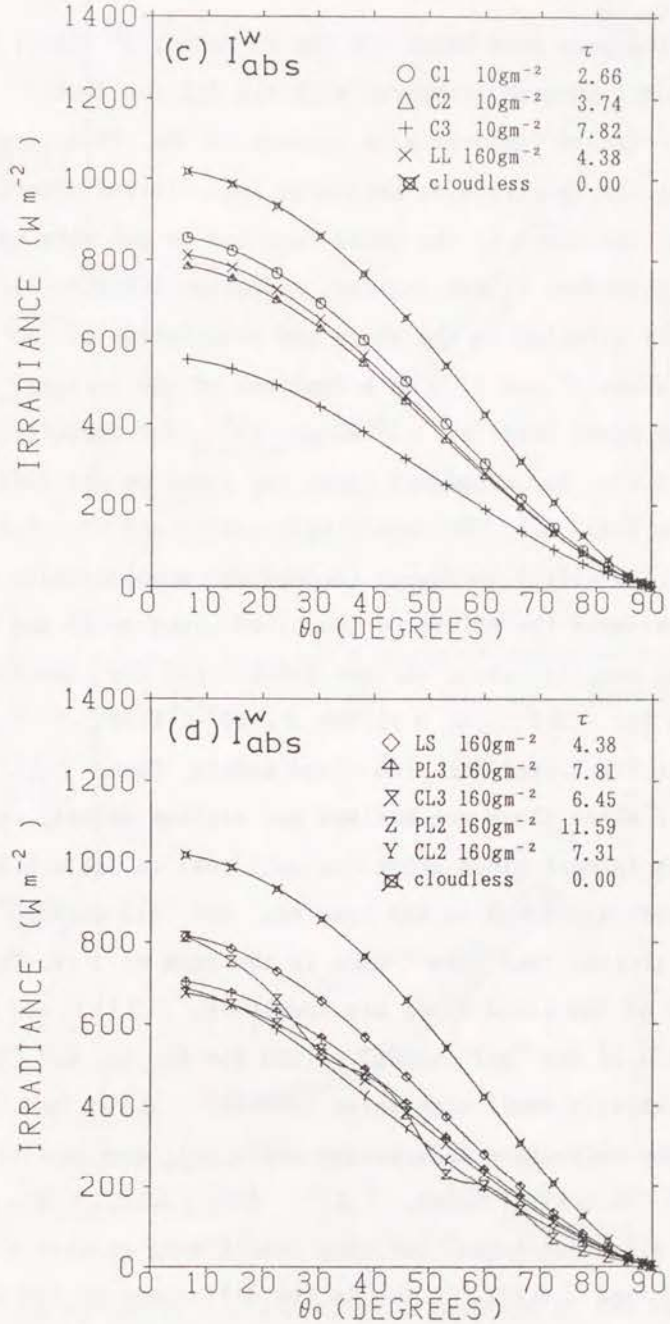

Fig.5.5 (continued)

show different features from those for the 3D cases. I^{t} (I^{*}_{abs}) for CL2 shows a trend of decrease (increase) compared with the CL3 for θ_0<10° . For PL2, I^{t} and I^{*}_{abs} show irregular features with respect to θ_0. This is mainly attributed to the fact that the radiation is scattered into limited directions for the PL2, and ω_0 and the shape of the phase function do not vary smoothly with respect to the direction of the incident radiation (Chapter 3). Thus I^{t} and I^{*}_{abs} are significantly affected by the shape and orientation of the ice crystals.

Figure 5.6 shows I^{t} and I^{*}_{abs} as a function of the vertical optical thickness of the cloud layer at θ_0=30° and 60° . For comparison purposes, ranges of I^{t} and I^{*}_{abs} for cloudless cases are shown on the left side of the figures based on Table 4.1. The center bars are I^{t} and I^{*}_{abs} for the RAOS (line 3 in Table 4.1). I^{t} (I^{*}_{abs}) increases (decreases) monotonically with the optical thickness. To estimate the effect of the cloud types on I^{t} and I^{*}_{abs}, the dispersion of I^{t} and I^{*}_{abs} among various cloud types are computed at τ=1 and 10 (Table 5.2). As for $|\Delta I^{t}|$ at τ=1 for θ_0=30° , first, I^{t} is interpolated from the data in Fig.5.6(a) for nine cloud models. Then, $|\Delta I^{t}|$ is defined as I^{t}(max)-I^{t}(min), where these are maximum and minimum values, respectively, for the cloud models in each cloud group (in each row) in Table 5.2. Values of the other columns are calculated in the same way. For "all clouds," $|\Delta I^{t}|$ and $|\Delta I^{*}_{abs}|$ are greater than 30Wm^{-2} even in the case of τ=1. This dispersion becomes smaller as the cloud types are specified. $|\Delta I^{t}|$ and $|\Delta I^{*}_{abs}|$ decrease to <1/3 of the "all clouds" values for C1, C2, and C3, which are composed of relatively small size water spheres. $|\Delta I^{t}|$ and $|\Delta I^{*}_{abs}|$ for LL and LS, where the refractive indices are different, are smaller than any of the others. For all ice crystal cases, $|\Delta I^{t}|$ and $|\Delta I^{*}_{abs}|$ are rather smaller than those for all cloud cases, but they have a much greater dispersion than 10Wm^{-2}. $|\Delta I^{t}|$ and $|\Delta I^{*}_{abs}|$, due to the difference of the shape of the ice crystals (PL3, CL3), is reduced to about half of those for all ice crystal case (PL3, CL3, PL2, CL2). $|\Delta I^{t}|$ and $|\Delta I^{*}_{abs}|$ due to the difference of the orientation of the ice crystals (PL3, PL2) and (CL3, CL2) are smaller than those due to the difference of the shape, however, they are not always <10Wm^{-2}. Thus the dispersion of I^{t} and I^{*}_{abs} due to the cloud types are generally greater

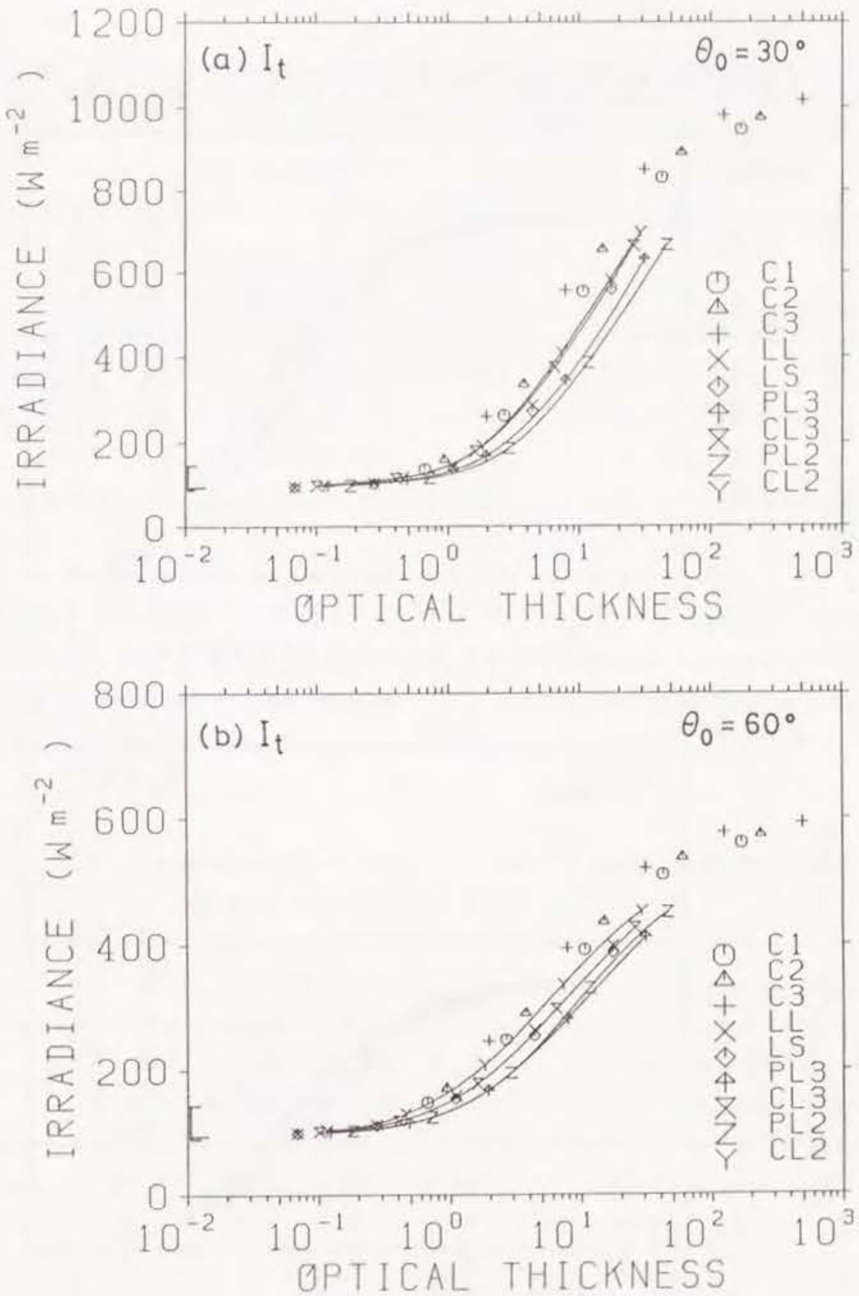

Fig.5.6 I^{t}(a and b) and I^{*}_{abs}(c and d) as a function of the vertical optical thickness of cloud layer at θ_0=30° and 60° .
Symbols for the ice crystals (PL3, CL3, PL2, and CL2) are connected by solid curves. Ranges of I^{t} and I^{*}_{abs} for cloudless cases are shown on the left side of the figures based on Table 4.1. The center bars are I^{t} and I^{*}_{abs} for the RAOS (line 3 in Table 4.1).

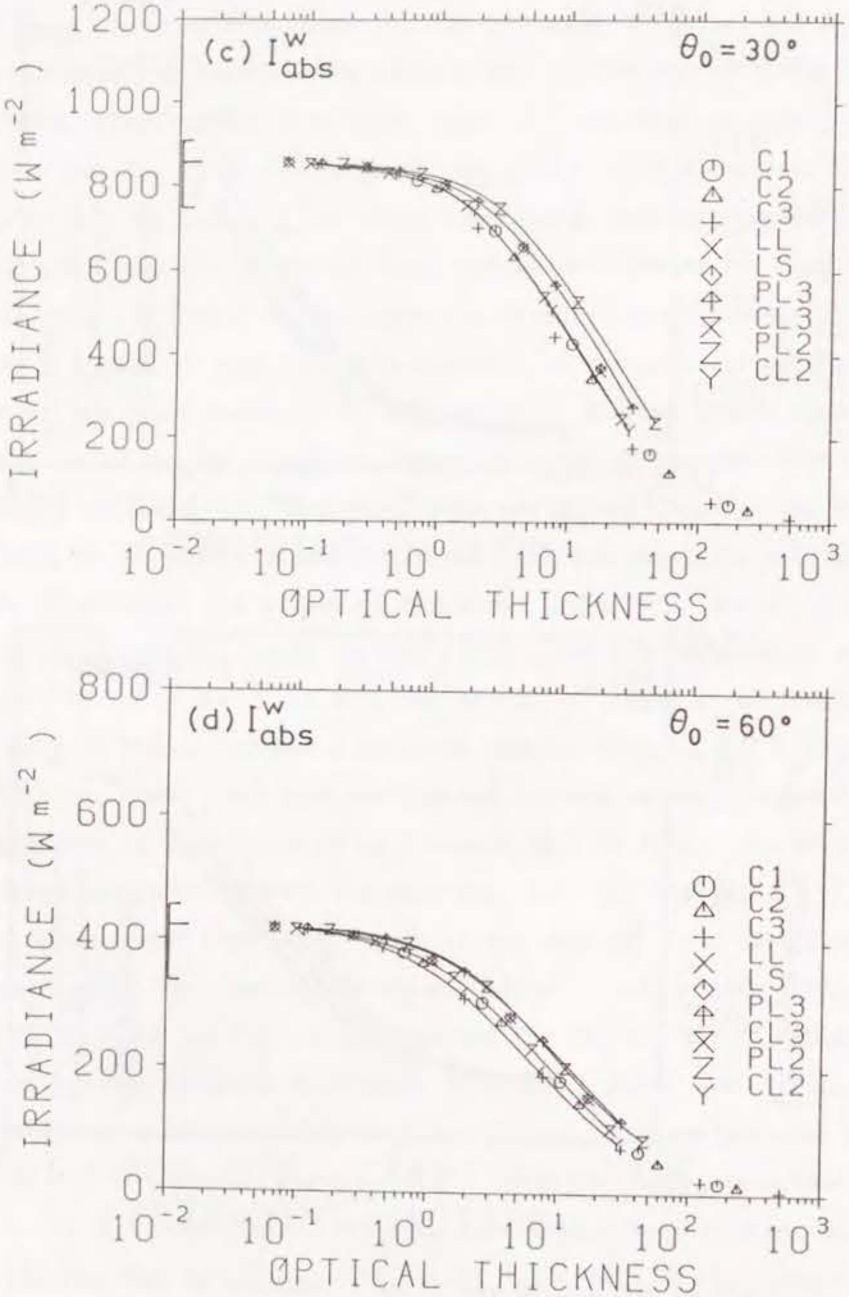

Fig.5.6 (continued)

Table 5.2 Dispersion of I^t and I^w_{abs} (Wm^{-2}) among various cloud types

	θ_0=30°				θ_0=60°			
	$\|\Delta I^t\|$		$\|\Delta I^w_{abs}\|$		$\|\Delta I^t\|$		$\|\Delta I^w_{abs}\|$	
	τ=1	τ=10	τ=1	τ=10	τ=1	τ=10	τ=1	τ=10
All clouds	41	245	32	155	37	113	32	53
C1, C2, C3*	5	68	6	43	2	32	2	18
LL, LS	4	18	1	4	4	10	1	2
PL3, CL3, PL2, CL2	28	110	31	107	33	59	32	50
PL3, CL3	15	71	17	68	15	33	14	30
PL3, PL2	9	31	14	37	1	12	4	6
CL3, CL2	4	9	1	3	17	25	14	20

* C3 cloud is omitted in the case of τ=1 because minimum optical thickness of C3 cloud is greater than 1.

Table 5.3 Dispersion of I^t and I^w_{abs} (Wm^{-2}) among various cloud types at radiance (0.63 μm) = 0.05

	$\|\Delta I^t\|$				$\|\Delta I^w_{abs}\|$			
	θ_0=30° θ = 6°	θ_0=30° θ =46°	θ_0=60° θ = 6°	θ_0=60° θ =46°	θ_0=30° θ = 6°	θ_0=30° θ =46°	θ_0=60° θ = 6°	θ_0=60° θ =46°
All clouds	25	70	65	63	52	96	57	84
C1, C2, C3	16	7	8	9	10	4	1	10
LL, LS	6	3	5	4	17	12	13	10
PL3, CL3, CL2	24	49	65	47	30	47	57	40
PL3, CL3	24	19	1	19	30	24	3	19
CL3, CL2	11	49	65	47	6	47	57	40

than $10Wm^{-2}$. Therefore, it is essential to give the thermodynamic phase of cloud particles, the shape and orientation of the ice crystals as cirrus cloud parameters for improving the accuracy of simulations that include the cirrus cloud layers.

5.4 Relationship between Radiance at the Top of the Atmosphere and I^{w}_{abs} and I^{t}

To develop a monitoring technique for estimating I^{t} and I^{w}_{abs} from the radiance observed by the satellites, relationships between radiance (R) at the top of the atmosphere and I^{t} (or I^{w}_{abs}) are investigated for different vertical water contents (Figs.5.7 and 5.8). The result from a cloudless model is indicated by the symbol A. Results for the cases of $\theta_0=30°$, 60° and $\theta=6°$, 46° at $\phi-\phi_0=180°$ are shown. The effective wavelength of $0.63\mu m$ is adopted for the radiance, which corresponds to Channel 1 of AVHRR onboard the NOAA meteorological satellite or the visible channel onboard the GMS satellite. The incident irradiance at $\lambda=0.63\mu m$ per unit area normal to itself is normalized to unity. The traces for PL2 are obviously different from the others. To evaluate the accuracy of I^{t} and I^{w}_{abs} derived from the radiance (R), the dispersion of I^{t} and I^{w}_{abs} among various cloud types at a fixed radiance value (R=0.05) are computed (Table 5.3). Here, $|\Delta I^{t}|$ and $|\Delta I^{w}_{abs}|$ are obtained in a similar way to Table 5.2. For example, I^{t} at R=0.05 is interpolated from the data in Fig.5.7 for cloud models except for PL2. Then, $|\Delta I^{t}|$ is defined as $I^{t}(max)-I^{t}(min)$, where these are maximum and minimum values, respectively, for the cloud models in each cloud group. For all cloud types, $|\Delta I^{t}|$ and $|\Delta I^{w}_{abs}|$ are $25-100Wm^{-2}$ for the θ_0, θ, and $\phi-\phi_0$ values presented here. It shows that when I^{t} and I^{w}_{abs} are inferred from R without any information on cloud type, errors of these magnitudes could be contained. The radiances near θ_0, θ and $\phi-\phi_0$ presented here show relatively smooth changes (Fig.6.3). The error could be larger in θ_0, θ, and $\phi-\phi_0$ where radiance changes greatly with respect to these angles. $|\Delta I^{t}|$ and $|\Delta I^{w}_{abs}|$ for C1, C2, and C3 are mostly smaller than $10Wm^{-2}$ except for $|\Delta I^{t}|$ at $\theta_0=30°$ and $\theta=6°$. $|\Delta I^{t}|$ and $|\Delta I^{w}_{abs}|$ for LL and LS are of the same order as those for C1, C2, and C3. For ice crystal clouds, except for PL2, they could be larger than $50Wm^{-2}$. Thus even

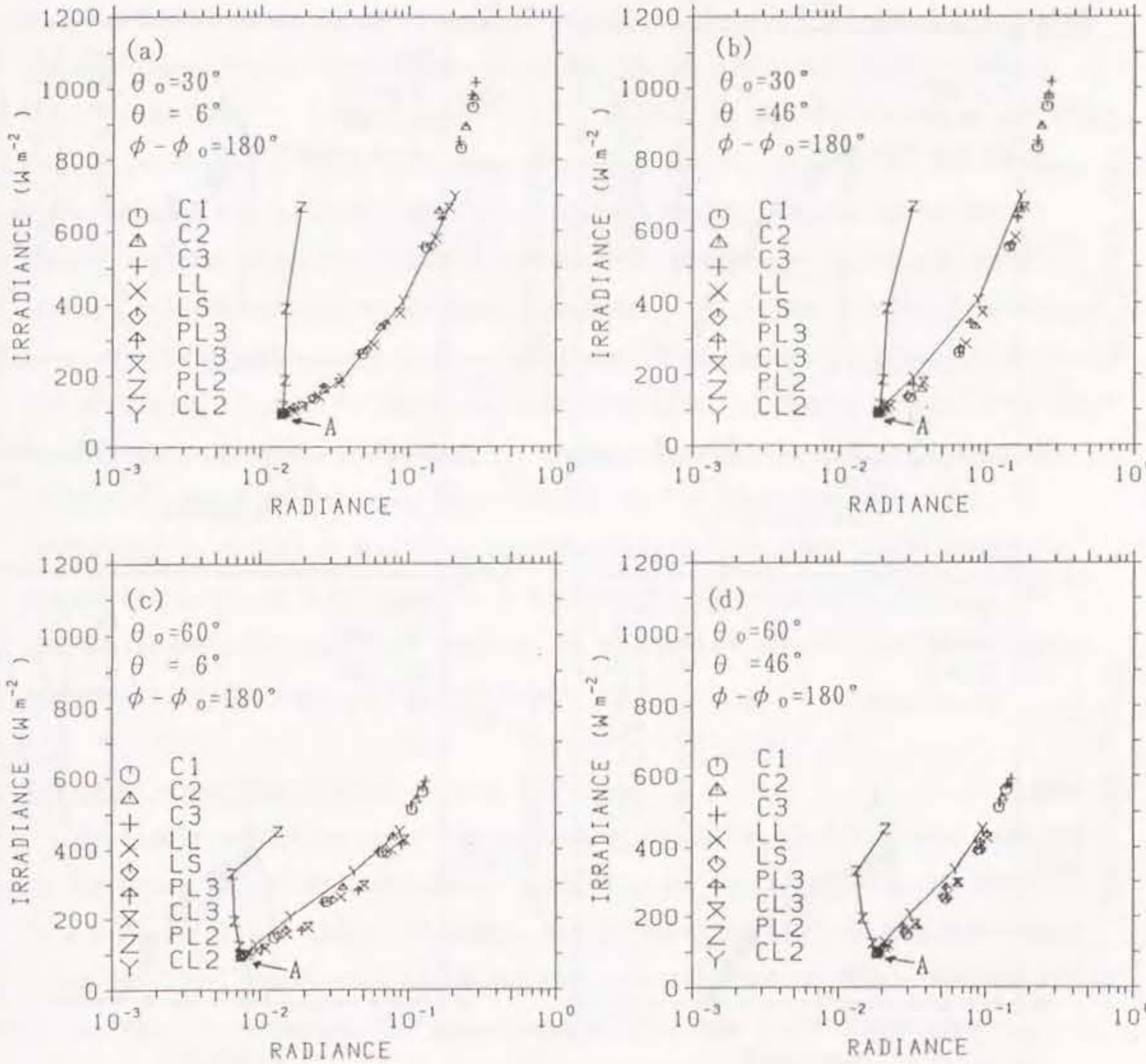

Fig.5.7 Relationship between radiance at the top of the atmosphere and I^{t} with changing vertical water content.
θ_0: solar zenith angle. θ : observation nadir angle.
$\phi-\phi_0$: azimuth difference between the incident and emergent radiation.
The incident irradiance at $\lambda=0.63\mu m$ per unit area normal to itself is normalized to unity. Cloudless model is indicated by A. Symbols for PL2 and CL2 are connected by solid lines.

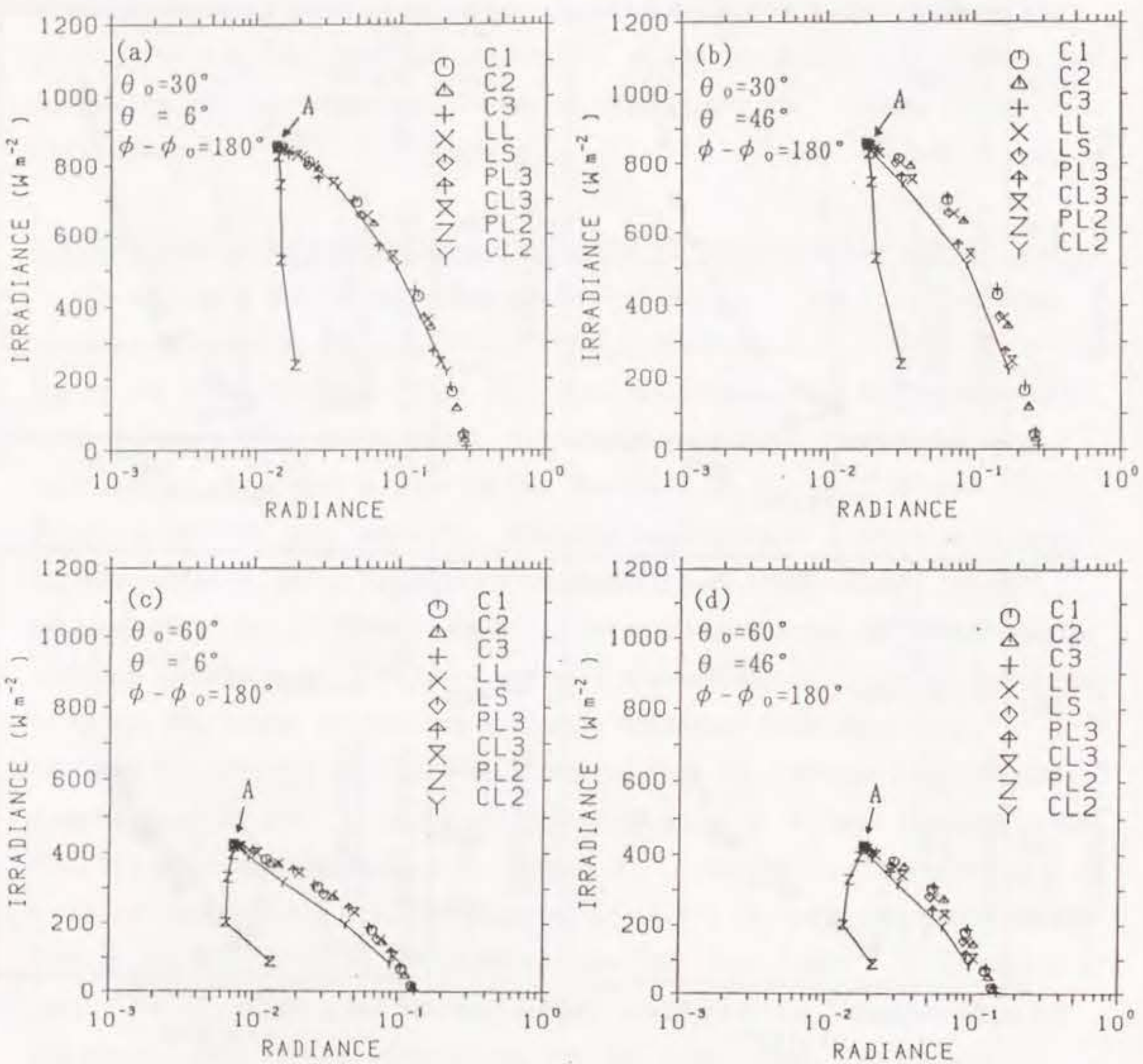

Fig.5.8 Relationship between radiance at the top of the atmosphere and I^{*}_{abs} with changing vertical water content.
θ_0: solar zenith angle. θ : observation nadir angle.
$\phi-\phi_0$: azimuth difference between the incident and emergent radiation. The incident irradiance at λ=0.63μm per unit area normal to itself is normalized to unity. Cloudless model is indicated by A. Symbols for PL2 and CL2 are connected by solid lines.

if information about thermodynamic phase (discrimination between ice and water cloud) is available, irradiances would not be retrieved having an accuracy better than 10Wm^{-2}. $|\Delta I^t|$ and $|\Delta I^{*}_{abs}|$, due to the difference in the shape of the ice crystals (PL3, CL3), are generally smaller than those due to the difference of the orientation (CL3, CL2), but neither can be neglected. It should be noted that the required accuracy of irradiance is for the monthly average over relatively broad areas, whereas $|\Delta I^t|$ and $|\Delta I^{*}_{abs}|$ discussed here are the dispersion of the instantaneous irradiance at a given location. If the errors in I^t and I^{*}_{abs} have the characteristics of random errors, they could be reduced by averaging. However, it seems probable that differences in the cloud type would produce systematic errors rather than random errors. Therefore, to derive I^t and I^{*}_{abs} more accurately than 10Wm^{-2} from satellite measurements, it is first necessary to know the thermodynamic phase of the cloud, second, the shape and orientation of the ice crystals are essential parameters in the case of the ice cloud.

5.5 Summary and Conclusions

To find a method to infer the shortwave radiation (0.285-5.0μm) absorbed in the ocean (I^{*}_{abs}) and the upward irradiance at the top of the atmosphere (I^t) from meteorological satellites, I^{*}_{abs} and I^t were computed using a realistic plane-parallel, vertically inhomogeneous atmosphere-ocean model, where a cirrus cloud layer is included. The dependence of I^{*}_{abs} and I^t on cirrus cloud parameters, such as the thermodynamic phase of the cloud particles and the shape and orientation of the hexagonal ice crystals, was especially investigated to discuss the contribution of these parameters to measurement accuracy.

The dispersion of I^t and I^{*}_{abs} ($|\Delta I^t|$ and $|\Delta I^{*}_{abs}|$) among all nine cloud types considered in this paper are >30Wm^{-2} and >150 Wm^{-2} for the cloud optical thickness of τ=1 and 10, respectively, for θ_0=30°. For all hexagonal ice crystal types (PL3, CL3, PL2, and CL2), both $|\Delta I^t|$ and $|\Delta I^{*}_{abs}|$ are ~30Wm^{-2} and ~100 Wm^{-2} at τ=1 and 10, respectively for θ_0=30°. These values have much more than an accuracy of 10Wm^{-2} that is required for climatological applications (for example, WMO, 1984, 1986). Therefore, it is essential to give the shape and orientation of the ice crystals as cirrus cloud parameters for improving the accuracy of simulation for the atmosphere model in which a cirrus cloud layer is included.

To develop a monitoring technique for estimating I^{t} and I^{*}_{abs} from the radiance observed by the satellites, the relationship between radiance (λ=0.63 μm) at the top of the atmosphere (R) and I^{t} (or I^{*}_{abs}) was investigated for θ_0=30°, 60° and θ=6°, 46° at $\phi-\phi_0$=180°. R for PL2 shows small change with τ, and it seems difficult to derive I^{t} and I^{*}_{abs} from R. Except for PL2, the dispersion of I^{t} and I^{*}_{abs} due to the cloud types ($|\Delta I^{t}|$ and $|\Delta I^{*}_{abs}|$) range from 25Wm^{-2} to 100Wm^{-2} at R=0.05. For ice crystal (except for PL2), they could be larger than 50Wm^{-2}. $|\Delta I^{t}|$ and $|\Delta I^{*}_{abs}|$ due to the difference of the shape of the ice crystals (PL3, CL3) and those due to the difference of the orientation (CL3, CL2) could be ~30Wm^{-2} and ~65Wm^{-2}, respectively. These seem to be systematic errors that cannot be reduced by averaging. Therefore, to derive I^{t} and I^{*}_{abs} accurately from satellite measurements, it is necessary to know the shape and orientation of the ice crystals in addition to the thermodynamic phase of the cloud. Note that results shown in this chapter are for a particular cloud model. The ice crystal particles are assumed to be hexagonal columns or plates, the orientation is randomly oriented in space (PL3, CL3) or randomly oriented in the horizontal plane (PL2, CL2), the size of the ice crystals is fixed, the cloud consists of a homogeneous single layer, and so on. An actual cloud would not necessarily satisfy such conditions. In particular, the effect of size and ratio of radius to length of particles should also be considered.

Chapter 6 Deriving Cirrus Information Using the Visible and Near-IR Channels of the Future NOAA-AVHRR Radiometer

6.1 Introduction

Optical characteristics of a cirrus cloud, such as optical thickness, water content, and the shape, dimension, orientation and thermodynamic phase of the cloud particles, are noted as essential components for understanding the mechanism of climate change or for improving weather forecasts. Evaluation of its characteristics is also required to derive surface parameters remotely from space. But these characteristics are not known precisely partly because cirrus clouds occur at high altitudes in the atmosphere (sometimes above the lower clouds), and are not easily observable from ground stations, and partly because satellites cannot measure their precise characteristics, particularly if they are thin.

For these investigations, first of all, the effect of parameters of cirrus clouds on the radiation in the atmosphere should be evaluated by numerical simulation using realistic models of atmosphere, cirrus clouds, and earth's surface. Numerical computations of the radiation field including the effects of cirrus clouds have been carried out by Plass and Kattawar (1971), Liou (1974), Stephens (1980), Asano (1983) and others. In their works, however, the cirrus particles are approximated by cylinders, by spheres with the refractive index of ice, or by Henyey-Greenstein phase functions. Tränkle and Greenler (1987) showed the multiple scattering effect of hexagonal ice crystals in halo phenomena by the Monte Carlo method. However, due to the limited memory space and CPU time of computer, a precise evaluation of phase functions used for radiative transfer equation has not yet been made, especially for ice crystals randomly oriented in a horizontal plane. Recently the effects of the shape and orientation of hexagonal ice crystals on the solar radiation were examined by Takano and Liou (1989b) and by Masuda and Takashima (1989, 1990a) using the doubling-adding method.

From the measurement point of view, many cloud radiation experimental studies, such as the International Cirrus Experiment (Raschke and Rockwitz, 1989), have evolved during the past several years. Curran and Wu (1982) analyzed data observed from Skylab to determine cloud top thermodynamic phase and particle size using the fact that ice exhibits relatively strong absorption at about 1.61 μm whereas water shows weak absorption. Furthermore, this wavelength is proposed as Channel 3A (1.56-1.66 μm) for the AVHRR of the NOAA K, L and M satellites (Sparkmam, 1989; Ahmad et al., 1989); therefore, rapid progress is expected in retrieval technique of cloud parameters using this wavelength together with the modified AVHRR Channels 1 (0.58-0.68 μm) and 2 (0.84-0.89 μm).

In this chapter, the reflectance and radiance of the upwelling radiation at the top of the atmosphere are computed at the effective wavelengths of AVHRR Channels 1 (0.63 μm), 2 (0.86 μm) and 3A (1.61 μm) using the single scattering phase functions and albedo for single scattering for (1) hexagonal ice crystals randomly oriented in space; (2) randomly oriented with long axis in the horizontal plane as shown by Ono (1969) and Platt et al. (1978); and (3) spherical water particles, which have been shown in Chapter 3. The effects of the water content and optical thickness of the cloud layer, thermodynamic phase of the cloud particles, and the shape and orientation of the hexagonal ice crystals on the radiation at the top are firstly estimated for the above wavelengths. A retrieval technique of cloud parameters for the next generation NOAA meteorological satellite is then discussed. Finally, comparison of the computational results of radiance with the Skylab observations is shown.

6.2 Reflectance of the Atmosphere-Ocean System

In this chapter the reflectance (ρ) of the upwelling radiation at the top of the atmosphere-ocean system are computed at the effective wavelengths of 0.63 μm, 0.86 μm, and 1.61 μm for the visible and near-infrared channels of the future NOAA-AVHRR radiometer. The atmosphere-ocean system used in this chapter is slightly changed compared with that in Chapters 4 and 5. The changed parameters are as follows: (1) the inhomogeneous atmosphere is simulated by four homogeneous sublayers (0-5km, 5-10km, 10-11km, 11-100km), (2) the vertical aerosol optical thickness is normalized to 0.250 and 0.873, respectively, for

the clear and the hazy models at λ=0.55 μm (aerosol type is fixed to the oceanic type), (3) the ocean is assumed to be homogeneous with an optical thickness of 10.0 at 0.63 μm, and 0.86 μm. The atmospheric optical thicknesses for extinction are shown in Table 6.1.

The ρ values (Appendix A) for λ=0.63 μm, 0.86 μm, and 1.61 μm are shown in Figs.6.1 (a), (b), and (c), respectively, as a function of solar zenith angle (θ_0) for nine cloud particle types. VWC is assumed to be 40gm^{-2}. Because of unity of ω_0 at λ=0.63 μm and 0.86 μm, ρ is mainly affected by the optical thickness of the cloud layer and the shapes of the single scattering functions. For the 2D plates (PL2), ρ varies rather irregularly with θ_0. As discussed in Chapter 3, this is mainly attributed to the fact that the radiation is scattered in limited directions for the 2D plates. The ρ values for CL2 are relatively smaller at θ_0~0° and 90° than those for PL3, CL3, LL and LS. This is mainly caused by the fact that $\langle\cos\Theta\rangle$ is larger for CL2 in these region [Fig.3.4(a)]. The ρ values for PL3, CL3, LL and LS show similar trends with respect to θ_0. The scaled optical thickness $\tau^*[=(1-\langle\cos\Theta\rangle)\times\tau]$ is often used to describe the radiation properties of clouds (Curran and Wu, 1982). For PL3, CL3, LL, and LS, τ^* is 0.1884, 0.2219, 0.1306, and 0.1237, respectively, at λ=0.63 μm. The magnitude of ρ shows good correspondence to that of τ^*. For example, it is 0.255, 0.274, 0.235 and 0.229 respectively for PL3, CL3, LL and LS at θ_0=60°. The ρ values for C1, C2 and C3 are larger than the others. For example, it is 0.573, 0.636 and 0.760 respectively for C1, C2 and C3 at θ_0=60°. The corresponding τ^* values are 1.608, 2.375 and 5.857.

The ρ at λ=0.63 μm shows similar characteristics to that at 0.86 μm except at θ_0>~70°. The ρ at λ=0.63 μm decreases at θ_0~90°. Such a decrease was not noted in the case of the cloud alone (not shown). Therefore, this decrease seems to be caused by the absorption by ozone in the stratosphere above the cirrus cloud (τ_{abs}=0.0258 at altitudes 11-100km in the present model). On the other hand, this decrease at θ_0~90° is not seen at λ=0.86 μm. The main absorbing constituent at λ=0.86 μm is water vapor, which is mostly below the cloud layer. Above the cloud layer, τ_{abs} due to water vapor is practically negligible (9.20×10^{-5}). At λ=1.61 μm, the ρ is also a function

Table 6.1 Atmospheric optical thicknesses for extinction

Wavelength (μm)		0.63	0.86	1.61
Molecules*		0.090	0.072	0.057
Aerosol	clear	0.254	0.260	0.252
	hazy	0.885	0.907	0.879
Cloud**	C1	10.708	10.877	11.373
	C2	15.077	15.378	16.655
	C3	31.517	33.416	43.508
	LL	1.095	1.098	1.112
	LS	1.098	1.101	1.112
	PL3	1.951	1.951	1.951
	CL3	1.612	1.612	1.612
	PL2	2.899	2.899	2.899
	CL2	1.826	1.826	1.826

* Optical thicknesses for molecules are mean values over the wavelength$\pm$0.04μm.

** Optical thicknesses for VWC of 40gm^{-2} are shown for clouds. Factors 1/16, 1/4, 4 and 16 should be multiplied for VWC of 2.5gm^{-2}, 10gm^{-2}, 160gm^{-2}, and 640gm^{-2}, respectively.

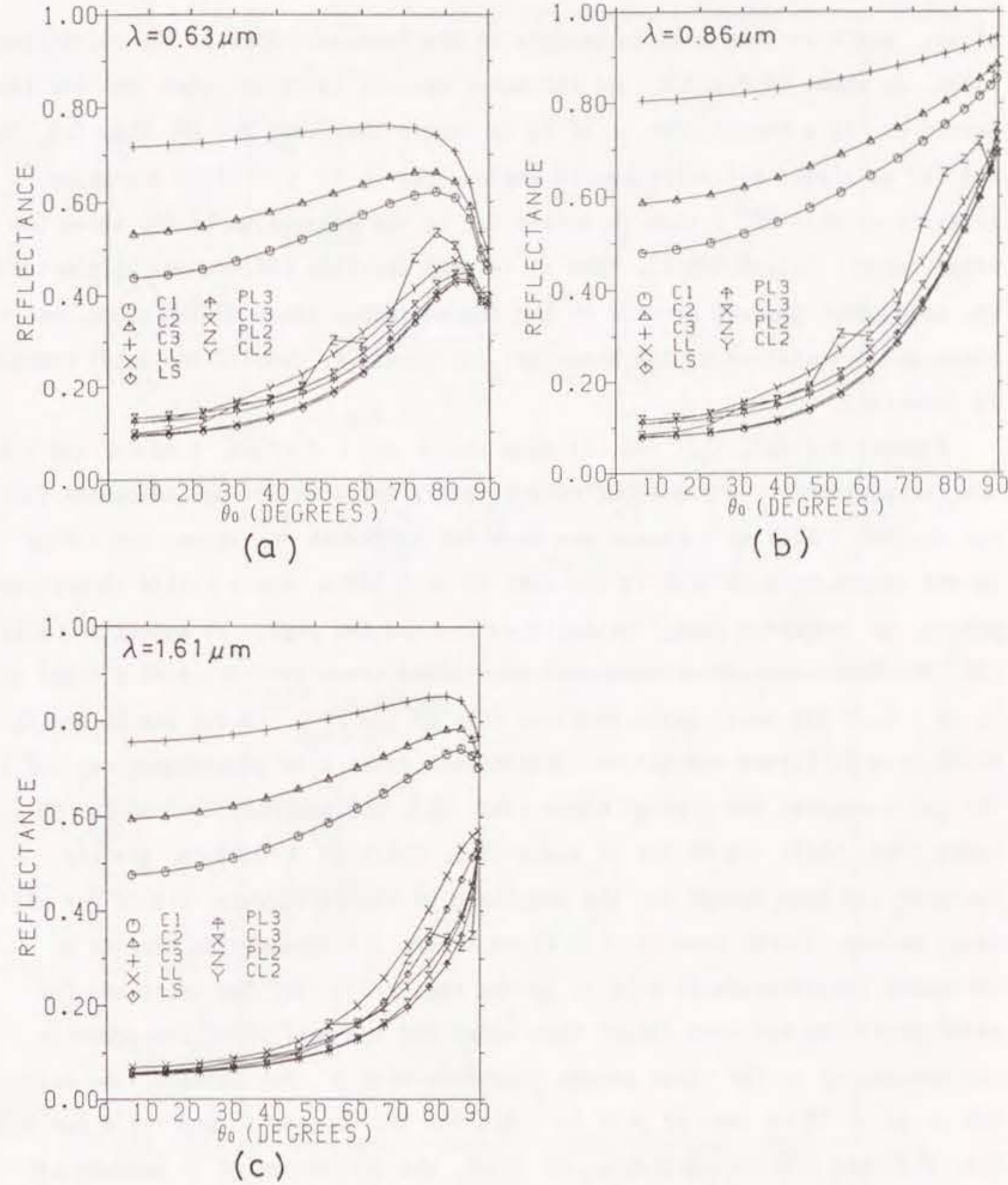

Fig.6.1 Reflectance at the top of the atmosphere as a function of the solar zenith angle (θ_0). (a) λ=0.63μm, (b) λ=0.86μm, (c) λ=1.61μm.

of ω_0, which in turn greatly depends on the imaginary part of the refractive index. As shown in Fig.3.5, ω_0 for water spheres is larger than that for ice particles. As a result, the ρ of LL is larger than that for LS, PL3, CL3, PL2 and CL2 at almost all solar zenith angles. The ρ at λ=1.61μm decreases slightly at $\theta_0\sim90°$; this is mainly due to the absorption by CO_2 above the cloud layer (τ_{abs}=0.00510). Thus it is seen that the reflectance at the top of the atmosphere depends greatly on the thermodynamic phase of the cloud, and the shape and orientation of the hexagonal ice crystals, even if the water content is identical.

Figures 6.2 (a), (b), and (c) show the ρ at λ=0.63μm, 0.86μm, and 1.61μm, respectively, as functions of vertically measured optical thickness (τ) for θ_0=60° . Similar features are seen for different θ_0 values exhibiting larger increases with θ_0. In the case of λ=0.63μm, where little absorption exists, ρ increases logarithmically with τ in the region of moderate τ: $1<\tau<20$. The difference of ρ among all nine cloud types is $\sim$0.1 with a fixed τ. It is $\sim$0.03 for small water particle (C1, C2 and C3); $\sim$0.015 for LL and LS, which have different refractive indices each other with same dimension; $\sim$0.1 for all hexagonal ice crystal cloud (PL3, CL3, PL2 and CL2); $\sim$0.06 for 3D types (PL3, CL3); $\sim$0.08 for 2D types (PL2, CL2). At λ=0.86μm, similar features are seen except for the magnitude of the difference: $\sim$0.16 for all cloud models. In the case of λ=1.61μm, where some absorption exists, ρ increases logarithmically with τ in the region $1<\tau<10$. The increases for water particles are much larger than those for ice particles. Consequently, differences of ρ for these groups increases with τ. For example, the ratio of the ρ at τ=10 to that at τ=1 is $\sim$2.6 for C1, C2, and C3 and $\sim$1.4 for PL3, CL3, PL2, and CL2, respectively. At τ=10, the difference of ρ between all nine cloud types is $\sim$0.5; it is $\sim$0.04 for C1, C2 and C3; $\sim$0.20 for LL and LS; $\sim$0.05 for PL3, CL3, PL2 and CL2; $\sim$0.005 for PL3 and CL3; $\sim$0.01 for PL2 and CL2.

It should be noted that the ρ of 2D ice crystals (PL2 and CL2) shows a different trend with respect to θ_0 than the other cloud models (Fig.6.1). As a consequence, 2D clouds exhibit higher ρ values than those of water clouds for

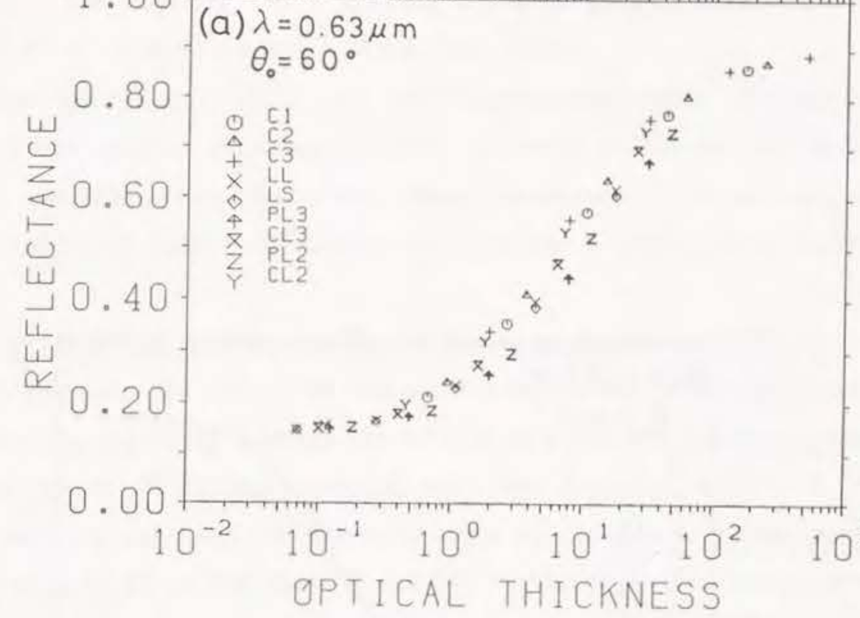

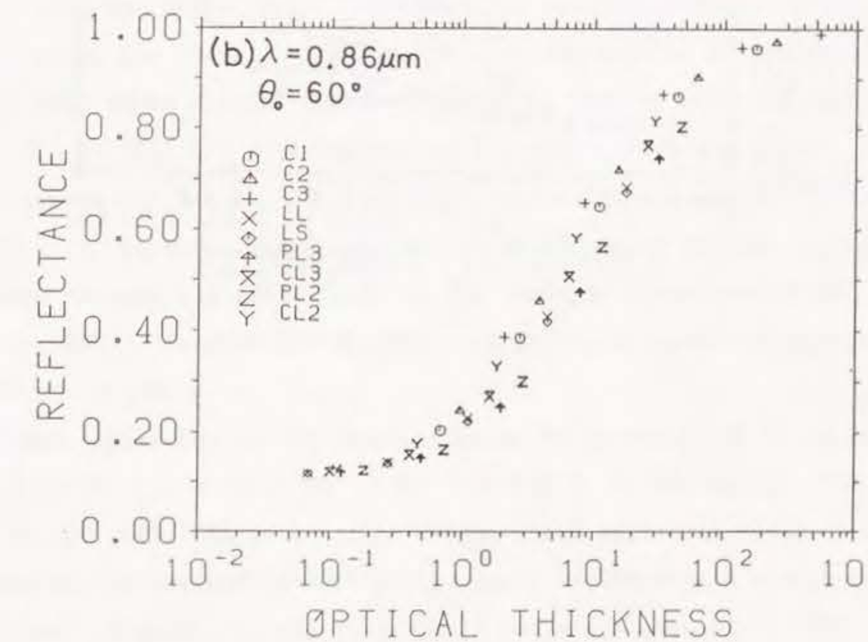

Fig.6.2 Reflectance at the top of the atmosphere as a function of the vertical optical thickness. (a) λ=0.63μm, (b) λ=0.86μm, (c) λ=1.61μm. θ_0=60° .

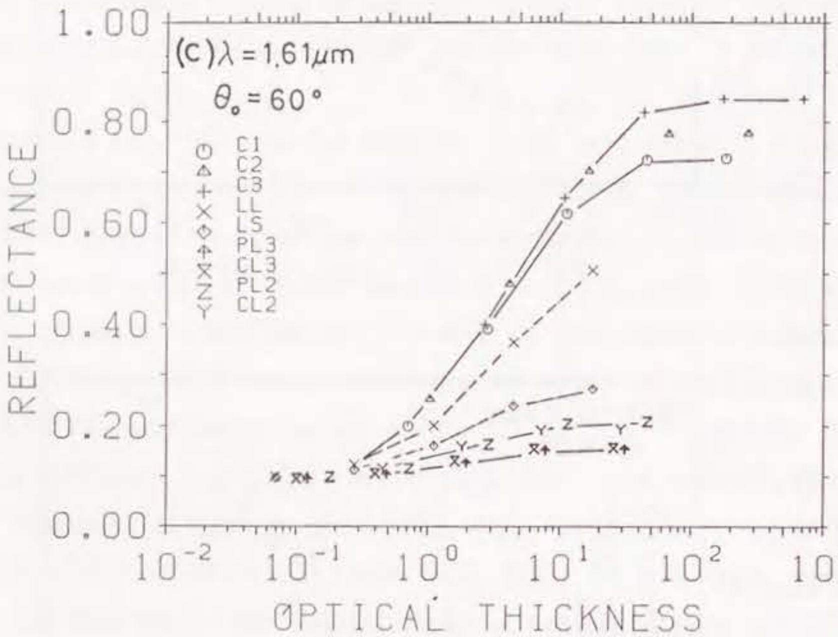

Fig.6.2 (continued)

some θ_0. For example, The ρ of PL2 is the largest of all cloud models at θ_0=77.6° at λ=0.63μm and 0.86μm (not shown).

Thus the shape, orientation, and thermodynamic phase of cloud particles, as well as the optical thickness or water content, affect the reflectance at the top of the atmosphere. Therefore, these parameters should be considered for Earth radiation budget retrievals that include a cirrus cloud layer.

6.3 Upwelling Radiance at the Top of the Atmosphere

To evaluate the effect of the water content and cloud type on radiances measured by the AVHRR onboard the NOAA satellite, the radiance (Appendix A) at the top of the atmosphere-ocean model was computed. Figures 6.3 (a)-(i) show the upwelling radiance for the nine types of cloud models considered in this paper at λ=0.63μm for θ_0=30° and 60° in the principal plane ($\phi-\phi_0$= 0-180°). Vertical water contents are assumed to be 0gm^{-2}(○), 2.5gm^{-2}(+), 40gm^{-2}(×) and 640gm^{-2}(□). Corresponding vertically measured optical thicknesses are shown in the figures. The radiance of 3D ice crystal layers (PL3, CL3) shows similar characteristics to that of spherical particle layers (C1, C2, C3, LL, LS) with respect to the observation angle (θ). For the very thin layers (+ for LL, LS, PL3, CL3), radiances are similar to those without cloud (○). In these cases, reflection by the ocean surface (i.e., sunglint) appears through the cloud layer at the specular direction (θ=30° , $\phi-\phi_0$=0° for θ_0=30°). However for θ_0=60° , it shifts slightly towards the horizon (θ ~75° , $\phi-\phi_0$=0°).

Small peaks due to the backscattering by aerosols and cloud particles are shown at $\theta=\theta_0$, $\phi-\phi_0$=180° . For 0.5<τ<2.0 (× for LL, LS, PL3, CL3 and + for C1, C2, C3), characteristics of the cloud particles appear clearly in the radiances, corresponding well to the peaks of the single scattering phase functions [Figs.3.1(a) and (b)]. Small peaks are seen at θ~72° in $\phi-\phi_0$=0° for θ_0=60° for PL3 and CL3, which correspond to the 46° halo. As the optical thickness increases (>10), radiances are smoothed out with θ and the peaks become relatively small. For PL2 [Fig.6.3(h)], there appear some optical phenomena even in the very thin cloud layer (+). As the optical thickness

Fig.6.3 Radiance of the upwelling radiation at the top of the atmosphere in the principal plane. λ=0.63 μm. (a)C1, (b)C2, (c)C3, (d)LL, (e)LS, (f)PL3, (g)CL3, (h)PL2, (i)CL2

θ_0: solar zenith angle. Abscissa denotes the nadir angle of observation (θ) with the solar plane on the left ($\phi-\phi_0$=0°) and the antisolar plane on the right ($\phi-\phi_0$=180°). The incident flux per unit area normal to itself is normalized to unity at the top.

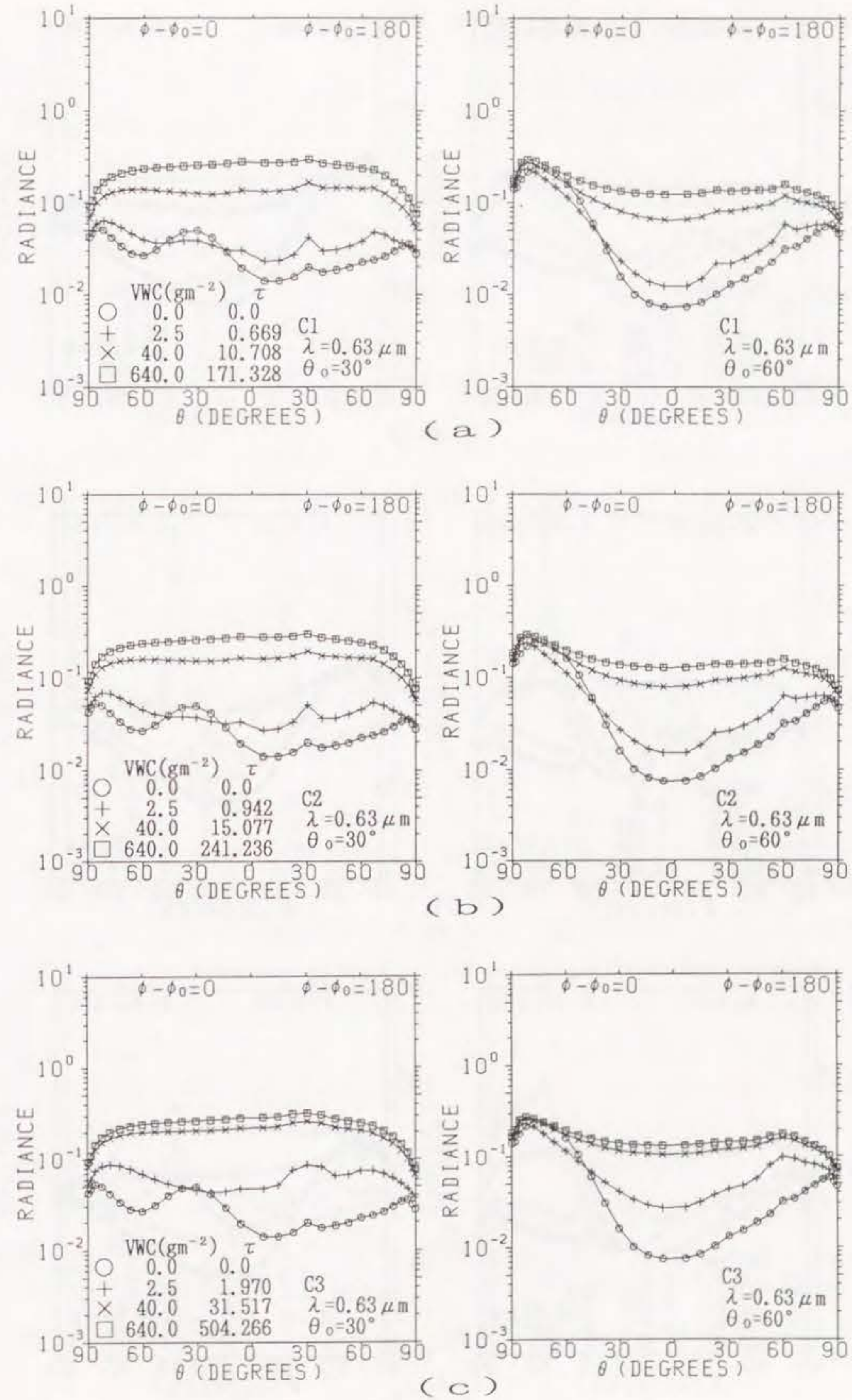

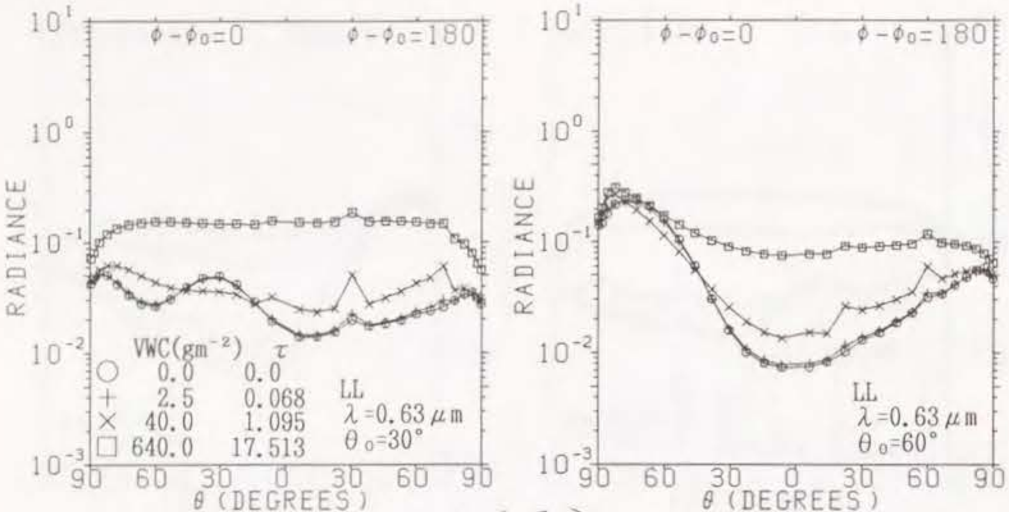
φ-φ0=0
φ-φ0=180
RADIANCE
VWC(gm⁻²) τ
0.0 0.0
2.5 0.068
40.0 1.095
640.0 17.513
LL
λ=0.63 μm
θ0=30°
θ0=60°
θ (DEGREES)
(d)

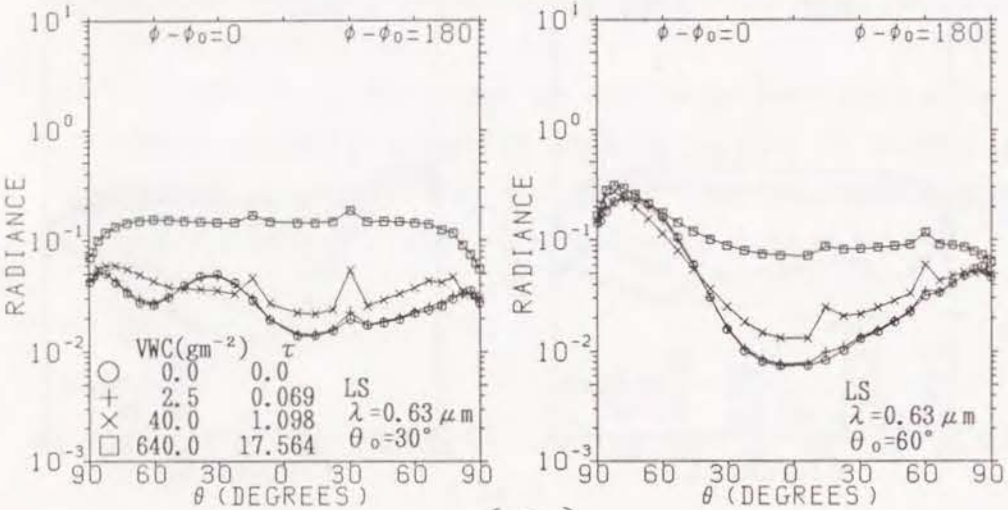
φ-φ0=0
φ-φ0=180
RADIANCE
VWC(gm⁻²) τ
0.0 0.0
2.5 0.069
40.0 1.098
640.0 17.564
LS
λ=0.63 μm
θ0=30°
θ0=60°
θ (DEGREES)
(e)

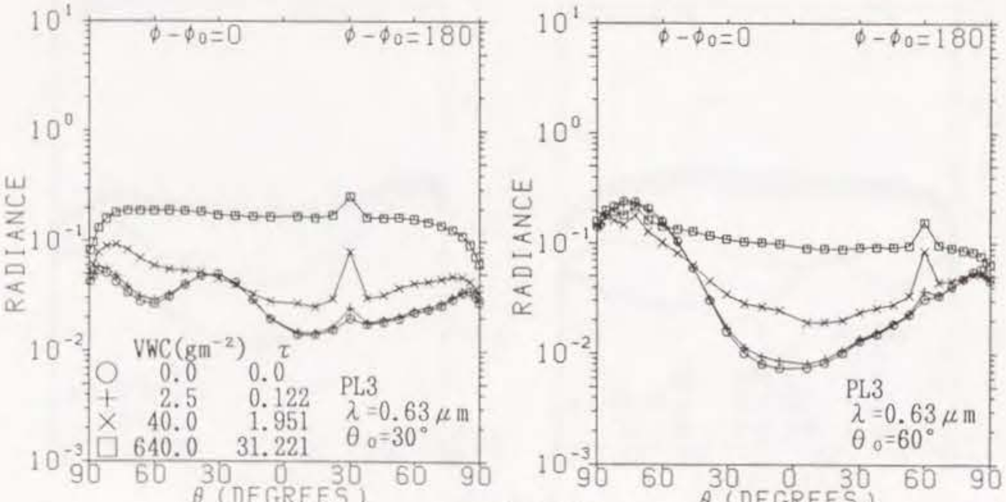
φ-φ0=0
φ-φ0=180
RADIANCE
VWC(gm⁻²) τ
0.0 0.0
2.5 0.122
40.0 1.951
640.0 31.221
PL3
λ=0.63 μm
θ0=30°
θ0=60°
θ (DEGREES)
(f)

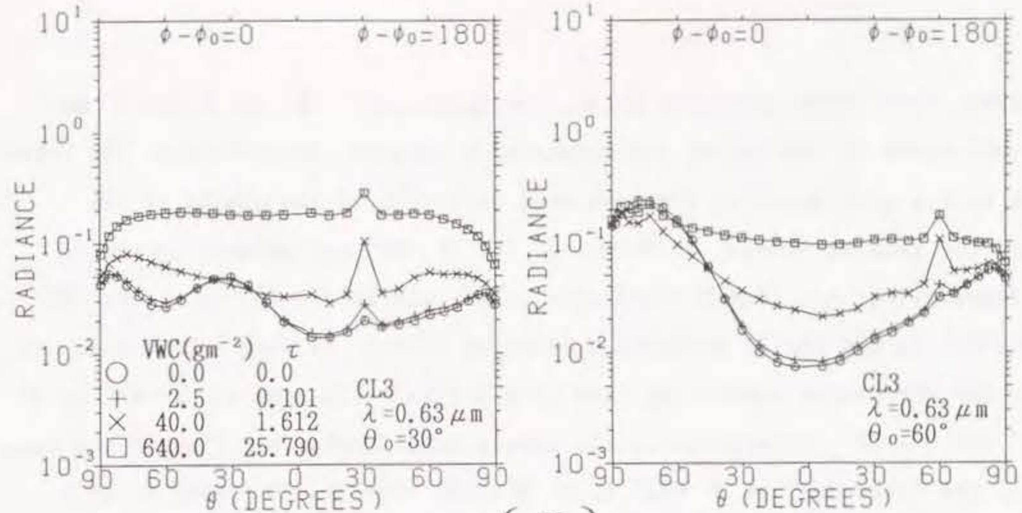
φ-φ0=0
φ-φ0=180
RADIANCE
VWC(gm⁻²) τ
0.0 0.0
2.5 0.101
40.0 1.612
640.0 25.790
CL3
λ=0.63 μm
θ0=30°
θ0=60°
θ (DEGREES)
(g)

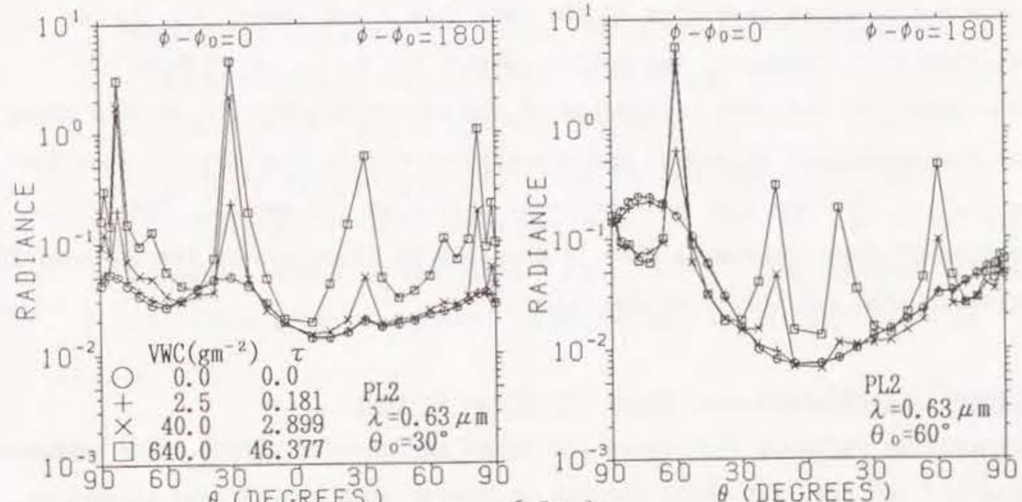
φ-φ0=0
φ-φ0=180
RADIANCE
VWC(gm⁻²) τ
0.0 0.0
2.5 0.181
40.0 2.899
640.0 46.377
PL2
λ=0.63 μm
θ0=30°
θ0=60°
θ (DEGREES)
(h)

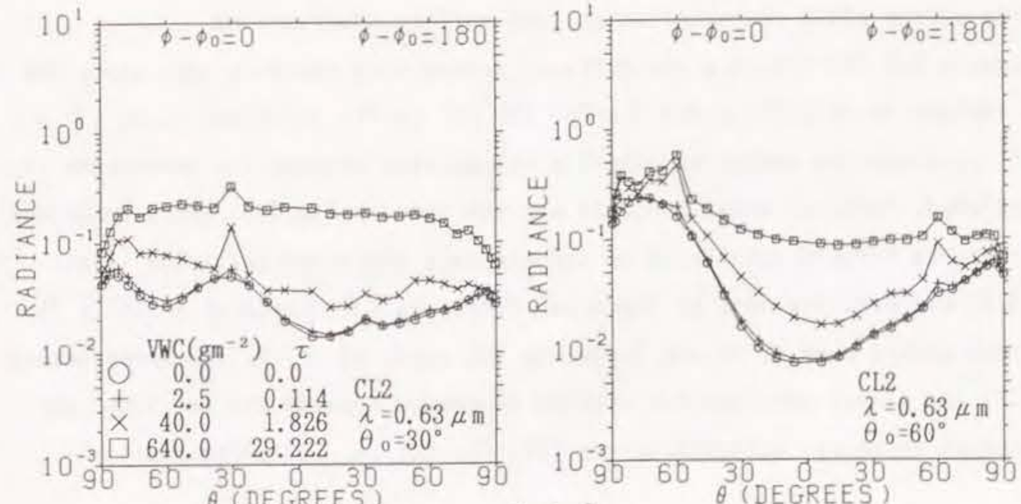
φ-φ0=0
φ-φ0=180
RADIANCE
VWC(gm⁻²) τ
0.0 0.0
2.5 0.114
40.0 1.826
640.0 29.222
CL2
λ=0.63 μm
θ0=30°
θ0=60°
θ (DEGREES)
(i)

increases, four large peaks are noted. The peaks at $\theta=\theta_0$ in $\phi-\phi_0$=0° and 180° correspond to the subsun and subparhelic circles, respectively. The latter may be partly attributed to the scattered radiation as the source of the former. The peak at $\theta\sim$15° in $\phi-\phi_0$=0° for θ_0=60° corresponds to the subcircumzenithal arc [Fig.3.2(b)]. The other peak at $\theta\sim$15° in $\phi-\phi_0$=180° for θ_0=60° is due to the multiple scattering effect, as such a peak does not appear for the single scattering case [Fig.3.2(b)]. The peak at $\theta\sim$82° in $\phi-\phi_0$=0° for θ_0=30° corresponds to the subcircumhorizontal arc (Takano and Liou, 1989a). The other peak at $\theta\sim$82° in $\phi-\phi_0$=180° for θ_0=30° seems to be a result of the multiple scattering effect. For CL2, there appears few optical phenomena due to cloud particles in the very thin cloud layer (+). As the optical thickness increases, the subsun appears at $\theta=\theta_0$ in $\phi-\phi_0$=0°.

Thus upwelling radiance at the top of the atmosphere for PL2 and CL2 shows optical phenomena such as subsun and subparhelic circle that are not seen for 3D ice crystal (PL3 and CL3) and spherical particles (LS and LL). The observation of these phenomena make it possible to discriminate the state of 2D ice crystals (PL2 and CL2) from the others.

6.4 Downwelling Radiance just above the Ocean Surface

Downwelling radiance just above the ocean surface for cirrus cloud composed of hexagonal ice crystals shows optical phenomena such as halo and antehelion that are not seen for spherical particles. These phenomena could be useful to identify cirrus cloud characteristics from surface observations.

Figures 6.4 (a)-(i) show the diffused downwelling radiance just above the ocean surface at λ=0.63μm for θ_0=30° and 60° in the principal plane ($\phi-\phi_0$=0-180°), where the radiation directly transmitted through the atmosphere is not included. Vertical water contents are the same as Fig.6.3. Sharp peaks due to the strong forward scattering by the aerosols and cloud particles (Figs. 2.2, 3.1, and 3.2) are seen at the solar direction ($\theta=\theta_0$ in $\phi-\phi_0$=0°) for all cloud models when τ is not large. In the cases of τ>10, radiances (except for PL2) are almost smoothed out showing decreases towards the horizons. The radiance of spherical particle layers (C1, C2, C3, LL, LS) shows similar

Fig.6.4 Diffused radiance of the downwelling radiation just above the ocean surface in the principal plane. Radiation directly transmitted through the atmosphere is not included. λ=0.63μm. (a)C1, (b)C2, (c)C3, (d)LL, (e)LS, (f)PL3, (g)CL3, (h)PL2, (i)CL2

θ_0: solar zenith angle. Abscissa denotes the zenith angle of observation (θ) with the solar plane on the left ($\phi-\phi_0$=0°) and the antisolar plane on the right ($\phi-\phi_0$=180°). The incident flux per unit area normal to itself is normalized to unity at the top.

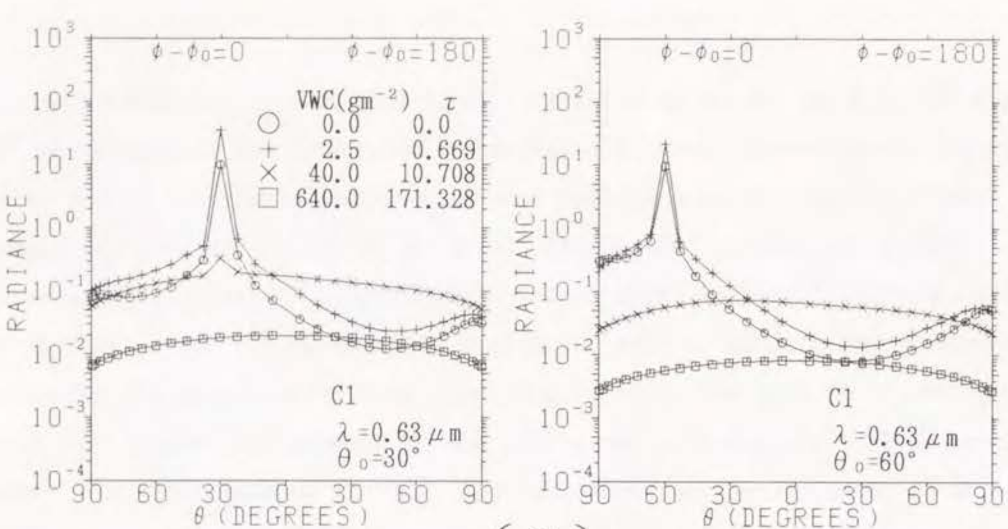

$\phi-\phi_0=0$
$\phi-\phi_0=180$
VWC(gm^{-2}) τ
0.0 0.0
2.5 0.669
40.0 10.708
640.0 171.328
RADIANCE
C1
$\lambda=0.63\,\mu m$
$\theta_0=30°$
θ (DEGREES)
$\phi-\phi_0=0$
$\phi-\phi_0=180$
RADIANCE
C1
$\lambda=0.63\,\mu m$
$\theta_0=60°$
θ (DEGREES)

(a)

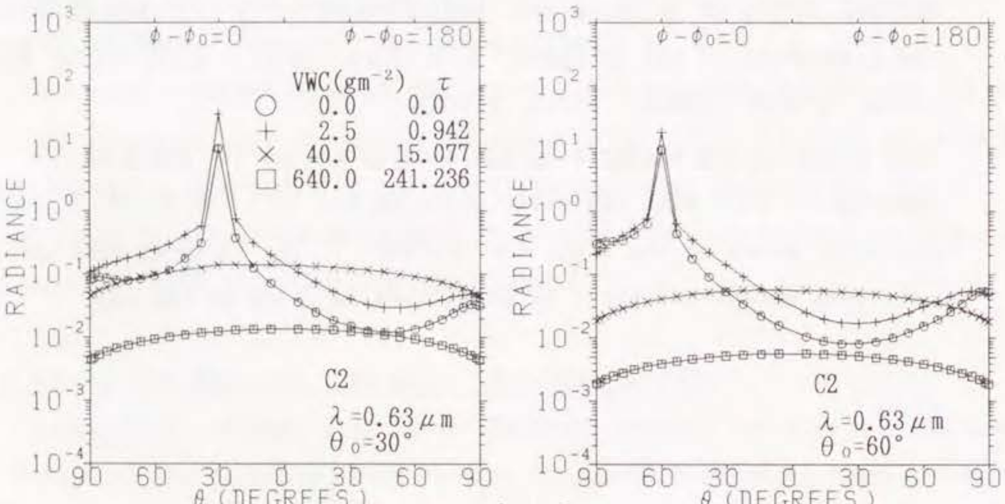

$\phi-\phi_0=0$
$\phi-\phi_0=180$
VWC(gm^{-2}) τ
0.0 0.0
2.5 0.942
40.0 15.077
640.0 241.236
RADIANCE
C2
$\lambda=0.63\,\mu m$
$\theta_0=30°$
θ (DEGREES)
$\phi-\phi_0=0$
$\phi-\phi_0=180$
RADIANCE
C2
$\lambda=0.63\,\mu m$
$\theta_0=60°$
θ (DEGREES)

(b)

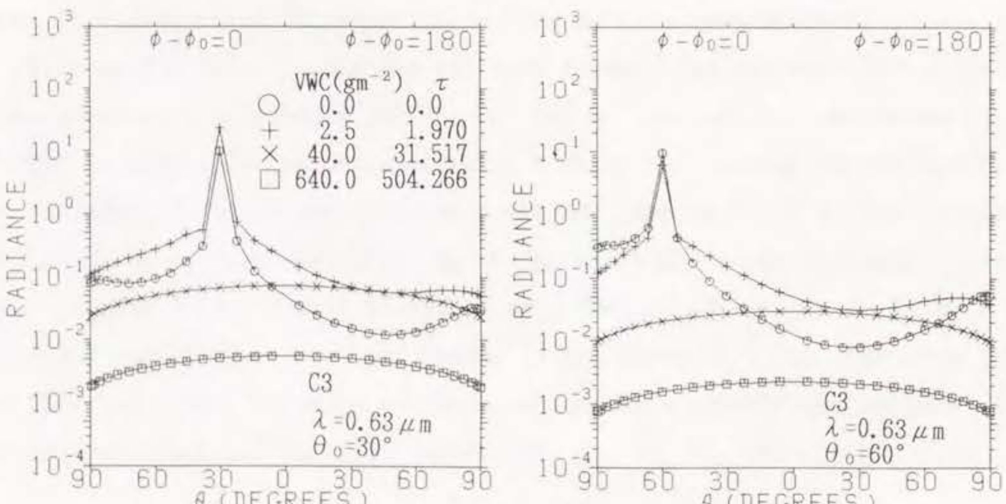

$\phi-\phi_0=0$
$\phi-\phi_0=180$
VWC(gm^{-2}) τ
0.0 0.0
2.5 1.970
40.0 31.517
640.0 504.266
RADIANCE
C3
$\lambda=0.63\,\mu m$
$\theta_0=30°$
θ (DEGREES)
$\phi-\phi_0=0$
$\phi-\phi_0=180$
RADIANCE
C3
$\lambda=0.63\,\mu m$
$\theta_0=60°$
θ (DEGREES)

(c)

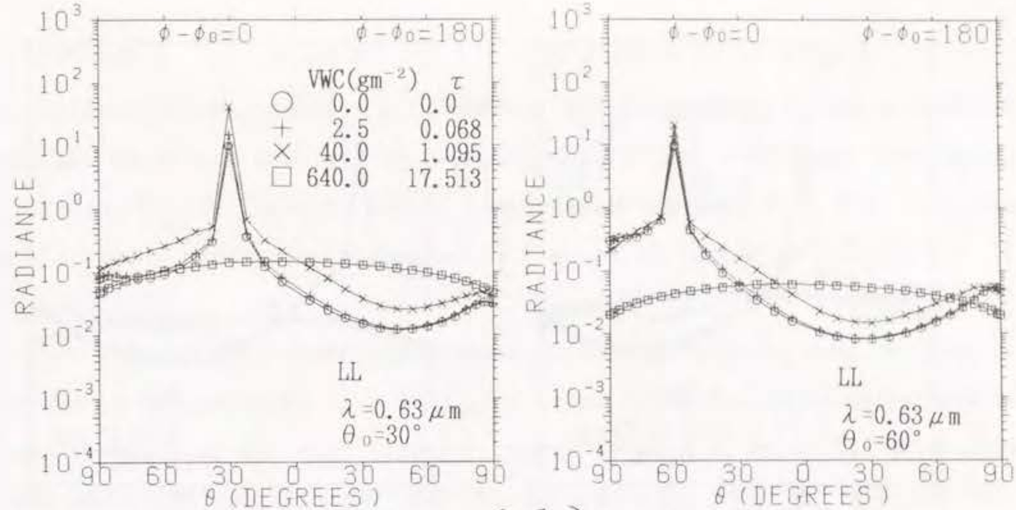

$\phi-\phi_0=0$
$\phi-\phi_0=180$
VWC(gm^{-2}) τ
0.0 0.0
2.5 0.068
40.0 1.095
640.0 17.513
RADIANCE
LL
$\lambda=0.63\,\mu m$
$\theta_0=30°$
θ (DEGREES)
$\phi-\phi_0=0$
$\phi-\phi_0=180$
RADIANCE
LL
$\lambda=0.63\,\mu m$
$\theta_0=60°$
θ (DEGREES)

(d)

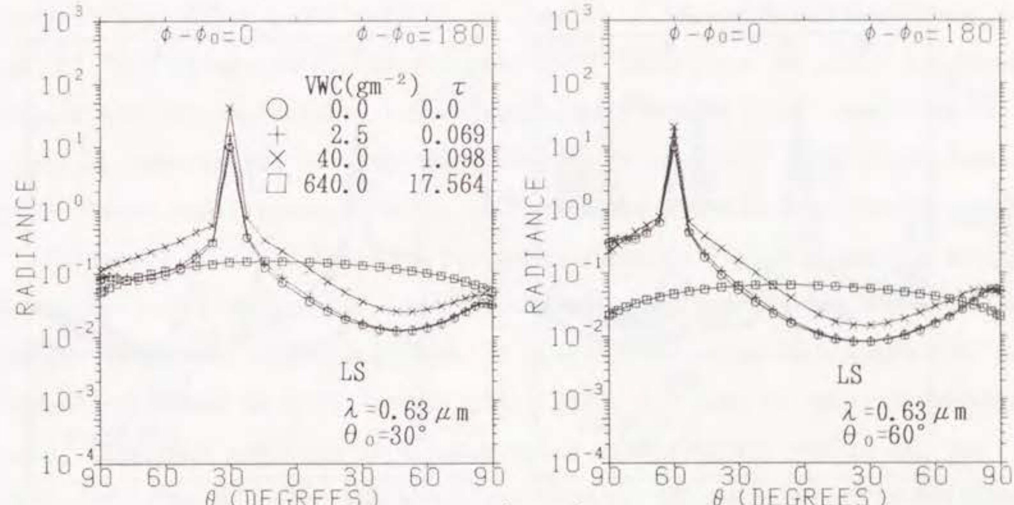

$\phi-\phi_0=0$
$\phi-\phi_0=180$
VWC(gm^{-2}) τ
0.0 0.0
2.5 0.069
40.0 1.098
640.0 17.564
RADIANCE
LS
$\lambda=0.63\,\mu m$
$\theta_0=30°$
θ (DEGREES)
$\phi-\phi_0=0$
$\phi-\phi_0=180$
RADIANCE
LS
$\lambda=0.63\,\mu m$
$\theta_0=60°$
θ (DEGREES)

(e)

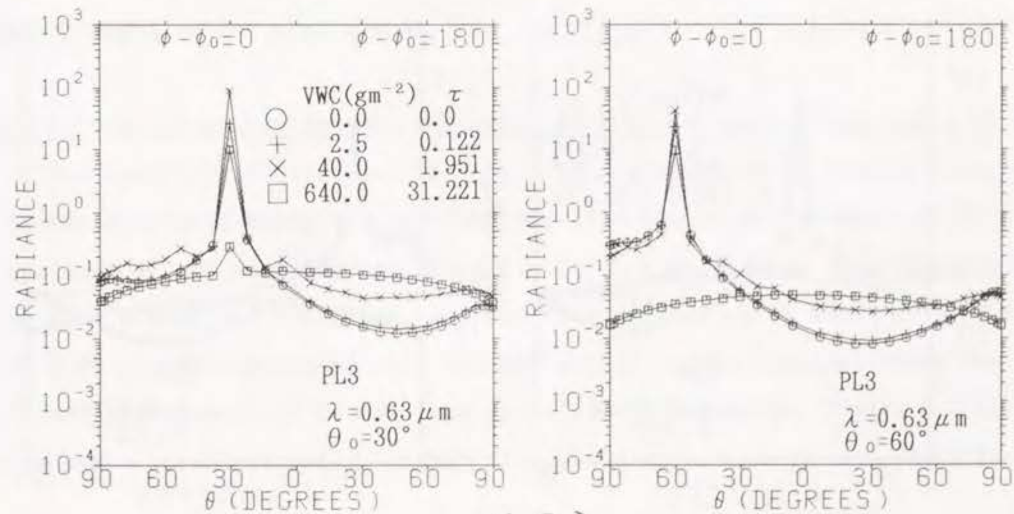

$\phi-\phi_0=0$
$\phi-\phi_0=180$
VWC(gm^{-2}) τ
0.0 0.0
2.5 0.122
40.0 1.951
640.0 31.221
RADIANCE
PL3
$\lambda=0.63\,\mu m$
$\theta_0=30°$
θ (DEGREES)
$\phi-\phi_0=0$
$\phi-\phi_0=180$
RADIANCE
PL3
$\lambda=0.63\,\mu m$
$\theta_0=60°$
θ (DEGREES)

(f)

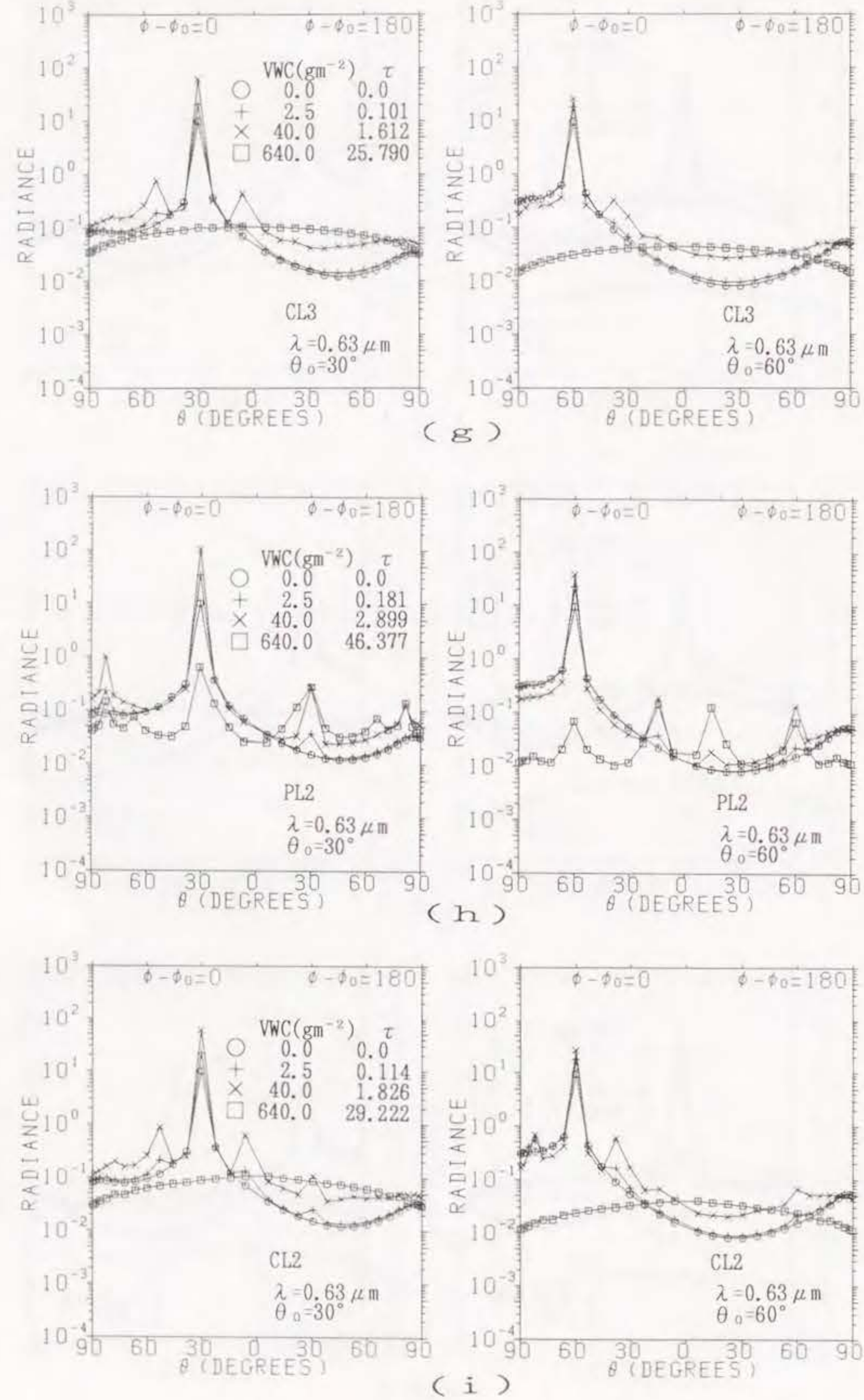

characteristics one another with respect to the observation angle (θ). For PL3 and CL3, halos are seen at the directions $\sim 22°$ and $\sim 46°$ away from the solar direction. The 22° halo of CL3 is larger than those of PL3. This is attributed to the single scattering phase function which is larger at 22° for CL3 [Fig. 3.1(b)].

For PL2 and CL2, there appear some optical phenomena; some of them correspond to the peaks of single scattering phase functions which have been shown in Fig. 3.2. For PL2, parhelic circle is seen at $\theta = \theta_0$ in $\phi - \phi_0 = 180°$. Peaks at $\theta \sim 80°$ in $\phi - \phi_0 = 0°$ for $\theta_0 = 30°$ and at $\theta \sim 22°$ in $\phi - \phi_0 = 0°$ for $\theta_0 = 60°$ are the circumhorizontal arc and the circumzenithal arc (Greenler, 1980), respectively. Other peaks seem to be results of the multiple scattering effect. For CL3, the upper tangent arc is seen $\sim 22°$ away from the solar direction towards the zenith, and the lower tangent arc is seen $\sim 22°$ away from the solar direction towards the horizon. At $\theta = \theta_0$ in $\phi - \phi_0 = 180°$, the antehelion is shown. Other small peaks seems to be results of the multiple scattering effect.

It should be noted that the radiances shown in Figs. 6.3 and 6.4 are for a particular cloud model: the ice crystal particles are assumed to be hexagonal columns or plates, the orientation is randomly oriented in a space (3D) or randomly oriented in a horizontal plane (2D), the size of the ice crystals is fixed, the cloud consists of a homogeneous single layer, and so on. The particles in an actual cloud would not necessarily satisfy such conditions. Therefore, the pattern of radiance shown in Figs. 6.3 and 6.4 would be smoothed out or modified for real clouds.

6.5 Interrelationship between Radiances at 0.63 μm (or 0.86 μm) and 1.61 μm

The upwelling radiance at the top of the atmosphere is greatly affected by the thermodynamic phase of the cloud particle due to the difference of magnitude of the imaginary parts of the refractive indices between water and ice (Table 3.1) at $\lambda = 1.61\ \mu m$, whereas this difference is small at $\lambda = 0.63\ \mu m$ and $0.86\ \mu m$. Making use of this feature should enable distinguishing the thermodynamic phase of clouds from satellite measurements. Figure 6.5 (a)-(f) show the interrelationship between the upwelling radiances in 0.63 μm (or 0.86

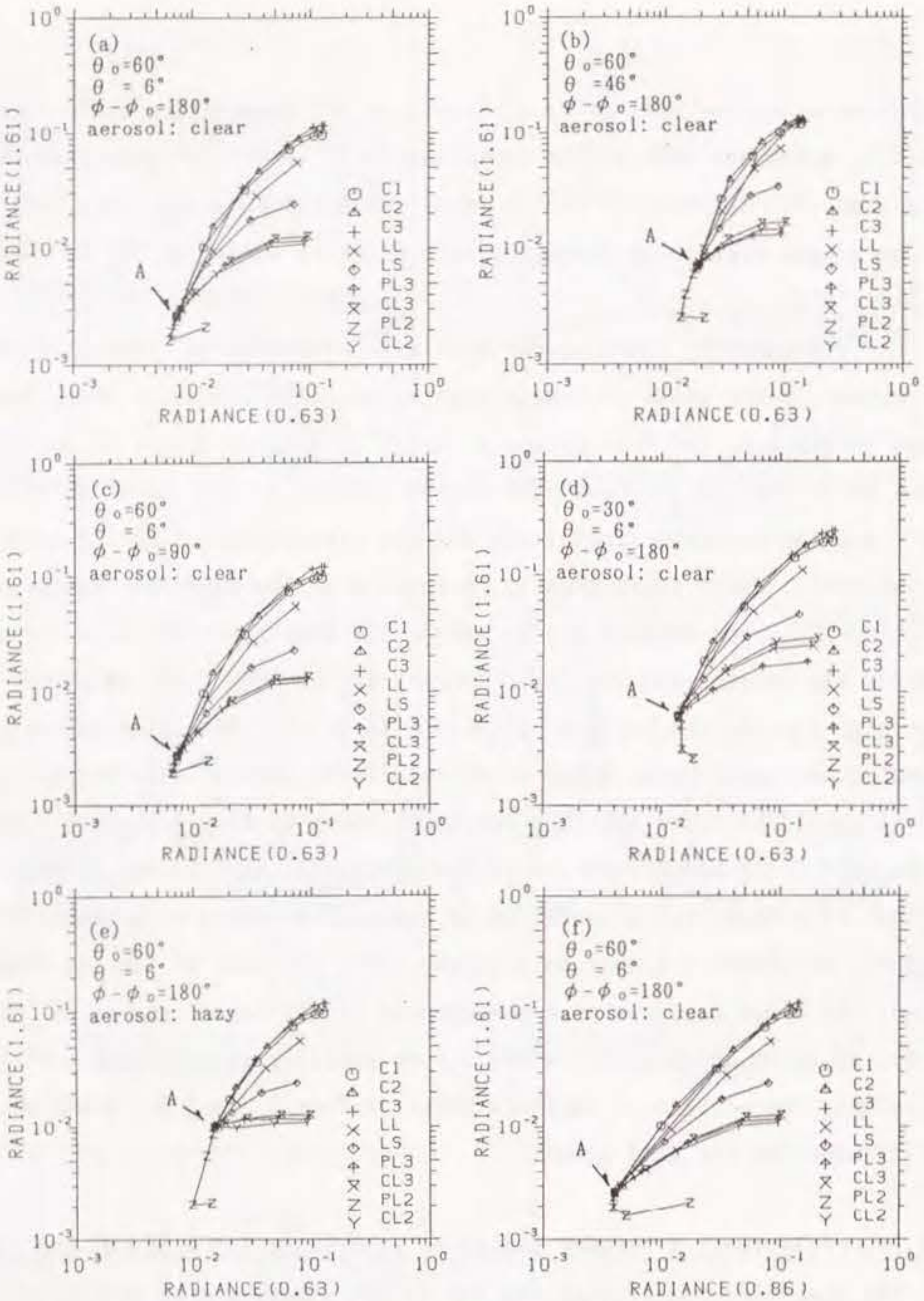

Fig.6.5 Interrelationship between the upwelling radiances with changing vertical water content.
(a) $\theta_0=60^\circ$, $\theta=6^\circ$, $\phi-\phi_0=180^\circ$, clear aerosol model, 0.63 μm vs 1.61 μm.
(b) Same as (a) but for $\theta=46^\circ$.
(c) Same as (a) but for $\phi-\phi_0=90^\circ$.
(d) Same as (a) but for $\theta_0=30^\circ$.
(e) Same as (a) but for hazy aerosol model.
(f) Same as (a) but for 0.86 μm vs 1.61 μm.
The incident flux per unit area normal to itself is normalized to unity at the top. Cloudless model is indicated by A.

μm) as abscissa and 1.61 μm as ordinate with changing vertical water content (2.5gm^{-2}, 10gm^{-2}, 40gm^{-2}, 160gm^{-2}, 640gm^{-2}). The cloudless model is indicated by the symbol A. The incident flux per unit area normal to itself is normalized to unity at the top.

Figure 6.5(a) is the case for $\theta_0=60^\circ$, $\theta=6^\circ$, $\phi-\phi_0=180^\circ$, and the clear aerosol model ($\tau=0.250$) using wavelengths of 0.63 μm and 1.61 μm. For PL2, the radiances at both wavelengths at first decrease and then increase with the increase in water content, whereas radiances of the other cloud models increase monotonically. There appear to be significantly different traces of radiances between those associated with the smaller water particles (C1, C2, C3) and those of the hexagonal ice crystals (PL3, CL3, PL2, CL2). For example, the radiance at 1.61 μm [R(1.61 μm)] is $1.0\times10^{-2}\sim1.2\times10^{-2}$ for PL3, CL3 and CL2 when R(0.63 μm) is 5.0×10^{-2}, whereas they are $5.5\times10^{-2}\sim6.2\times10^{-2}$ for C1, C2 and C3. Traces for LL and LS cloud types lie between the above two groups. For LL (water sphere), it is nearer the C1, C2, C3 group. For LS (ice sphere), it is rather similar to LL in the case of small water content, but it approaches the PL3, CL3, CL2 group with increase of water content.

Thus the difference between traces of radiances for the C1, C2, C3 group and for the PL3, CL3, CL2 group is much clearer than that for LL and LS types. Here it should be noted that the cases of LL and LS were considered as reference models. Therefore, the feasibility of discriminating the cloud thermodynamic phase from satellite data is more clearly ascertained compared with the simulation using only LL and LS type cloud models.

In Figs.6.5(b) and (c), θ and $\phi-\phi_0$ are changed to 46° and 90°, respectively. General features described above are the same as for Fig.6.5(a) although the magnitude of the radiances is different. In Fig.6.5(d), θ_0 is changed to 30°. Roughly speaking, traces of radiances are similar to those in Fig.6.5(a), but the difference among PL3, CL3 and CL2 becomes larger. For example, R(1.61 μm) is $1.4\times10^{-2}\sim1.9\times10^{-2}$ for PL3, CL3 and CL2 when R(0.63 μm) is 5.0×10^{-2}, whereas it is $5.4\times10^{-2}\sim5.9\times10^{-2}$ for C1, C2 and C3.

In Fig.6.5(e), the atmospheric condition is changed from clear ($\tau=0.250$) to hazy model ($\tau=0.873$). The coordinates without cloud (indicated by A) shifted from (0.0075, 0.0026) for the clear model [Fig.6.5(a)] to (0.0150, 0.0102) for the hazy model. The latter coordinates in the hazy model correspond to the point where the optical thickness for C1, C2 and C3 is 0.5~1.0 for the clear model [Fig.6.5(a)]. This example shows that particularly in the case of thin cloud layer, the background atmospheric condition should simultaneously be derived from satellite.

In Fig.6.5(f), the abscissa is the radiance at λ=0.86μm instead of at 0.63μm. Radiances on the ordinate are the same as Fig.6.5(a). In the abscissa, however, R(0.86μm) is smaller than R(0.63μm) in Fig.6.5(a) for the case of small water contents. This feature was also noted in the other conditions where θ_0, θ, $\phi-\phi_0$ and atmospheric conditions were changed. Therefore, the difference in the abscissa between R(0.63μm) and R(0.86μm) seems to be due to the difference of the wavelength dependence of the background molecules and aerosols rather than that of the cloud layer. Coordinates of cloudless model (indicated by A) are (0.0075, 0.0026) and (0.0040, 0.0026) for Fig.6.5(a) and (f), respectively.

These results show that a combination of 0.86μm and 1.61μm is more suitable than that of 0.63μm and 1.61μm for the analysis of cloud field from NOAA meteorological satellites, particularly for thin cloud layers. It should be noted that the above result would not be applicable in the angles of θ_0, θ and $\phi-\phi_0$ where optical phenomena due to 2D ice crystals (PL2 and CL2), such as subsun and subparhelic circle, are dominant.

As for the feasibility of remote sensing of aerosols over the oceans from present NOAA meteorological satellites during cloudless conditions, the effect of water vapor absorption in Channel 2 has been pointed out by Masuda et al. (1988). In the remote sensing of cloud, however, Channel 1 (0.63μm) seems to be more affected than Channel 2 (0.86μm) due to the absorption of the background constituents as discussed before. Optical thickness of the absorption by molecules in the Channel 2 band (0.725-1.1μm) in the present NOAA meteorological satellites is computed to be 0.00526 by LOWTRAN6 in the region above 11km for midlatitude summer model. This value is about 1/5 of 0.0258 in Channel 1 (0.59-0.67μm in the present study). Therefore, the problem

of water vapor absorption in Channel 2 is not so important in cloud remote sensing.

It is expected that one can distinguish the thermodynamic phase of cloud particles from space using multichannels that include 1.61μm. Discrimination of the orientation of the ice cloud crystals, except for the PL2 type, seems to be difficult by the method described in this section.

6.6 Comparison of Computational Results with Skylab Observations

Curran and Wu (1982) have analyzed Skylab observations of the radiation reflected and emitted by clouds to determine the thermodynamic phase, particle size and temperature of lee-wave clouds over northern New Mexico in December 1973. They have presented the possible conclusion that the clouds are composed of supercooled water droplets based on the near-infrared (0.83μm, 1.61μm, and 2.125μm) radiation transfer properties of clouds.

Skylab was launched on 14 May 1973 into near circular orbit at an altitude of 435km above the Earth. Curran and Wu (1982) analyzed reflection functions from three near-infrared channels out of 13 channels of multispectral scanner which scanned the Earth at a constant observation angle of 5°, where the solar zenith angle at the time of observation was 62°. The cloud tops were close to an altitude of 10km above mean sea level. The soundings at Albuquerque on 1 December showed a temperature of ~-42° C at the 10km level. Table 6.2 shows the reflection function averaged over 100 picture elements at 0.83μm and 1.61μm for sixteen locations over the cloud. Here the "reflection function" (R*) is defined by

$$R^*(\mu, \mu_0, \phi-\phi_0)=(\pi/\mu_0)\cdot R(\mu, \mu_0, \phi-\phi_0)/(\pi F_0), \qquad (6.1)$$

where μ, μ_0, $\phi-\phi_0$, R, and πF_0 are cosine of the observation nadir angle, cosine of the solar zenith angle, difference of azimuth angles between the incident and reflected radiations, radiance at the top of the atmosphere, and the incident solar flux density normal to its direction at the top of the atmosphere, respectively. The reflection function thus defined represents the ratio of the radiance at the top of the atmosphere to an ideal Lambert surface for which the albedo is unity (Curran and Wu, 1982). When the solar flux

Table 6.2 Area averaged reflection function (after Curran and Wu, 1982)

Location	$R^*(0.83\,\mu m)$	$R^*(1.61\,\mu m)$
A	1.021	0.690
B	0.923	0.620
C	0.922	0.599
D	0.910	0.959
E	0.825	0.518
F	0.818	0.591
G	0.755	0.537
H	0.749	0.529
I	0.709	0.502
J	0.705	0.521
K	0.495	0.245
L	0.481	0.366
M	0.462	0.420
N	0.459	0.436
O	0.425	0.408
P	0.374	0.354

density incident on the top of the atmosphere is normalized to unity ($\pi F_0=1$), Eq. (6.1) becomes,

$$R^*(\mu,\mu_0,\phi-\phi_0)=(\pi/\mu_0)\cdot R(\mu,\mu_0,\phi-\phi_0). \qquad (6.2)$$

Therefore the radiance values described in the previous sections are converted to the reflection function by multiplying a factor of π/μ_0. Figure 6.6 illustrates the 16 pairs of reflection function at $0.83\,\mu m$ and $1.61\,\mu m$ presented in Table 6.2. The curves shown in Fig.6.6 are theoretical calculations relating the reflection functions calculated by Curran and Wu (1982). Curves are shown for zero ground albedo and for the wavelength-dependent ground albedos found at a location of cloudless areas. The theoretical curves are generated by doubling method for a plane-parallel cloud layer which contains spherical water droplets or ice clouds, where the background molecules and aerosols are not included. The size distribution function for the particles used by Curran and Wu (1982) is the modified gamma distribution in the form,

$$n(r)=\mathrm{constant}\cdot r^{(1-3b)/b}\cdot e^{-r/(ab)}, \qquad (6.3)$$

where n(r)dr is the number of particles per unit volume with radius between r and r+dr. Parameters a and b are the effective radius (r_e) and a dimensionless effective variance (v_e), respectively. Note that this distribution function is essentially the same as that for C1, C2, and C3 cloud models described in Chapter 2, although expression is slightly different each other. The parameters (r_e, v_e) for the distributions used in Fig.6.6 are ($5.56\,\mu m$, 0.111) for the upper curves in each phase and ($16.2\,\mu m$, 0.128) for lower curves. The mode radii, given by $r_e\cdot(1-3v_e)$, for each case are $3.7\,\mu m$ and $10\,\mu m$, respectively. The refractive indices used by Curran and Wu (1982) is 1.33-i0.0, $1.317-i8.55\times10^{-5}$ for $0.83\,\mu m$ and $1.61\,\mu m$, respectively, for water droplets, and 1.33-i0.0, $1.293-i3.8\times10^{-4}$ for ice clouds. Based on the reflection function of $R^*(0.83)>0.7$ in Fig 6.6, Curran and Wu (1982) estimated that the effective radius is $5.7\pm1.1\,\mu m<r_e<10.6\pm1.0\,\mu m$ for water, and $1.4\pm0.6\,\mu m<r_e<3.5\pm0.5\,\mu m$ for ice, respectively. The averaged similarity parameter ($s_{1.61}$), which is defined by

$$\{(1-\omega_0)/(1-\langle\cos\Theta\rangle\omega_0)\}^{1/2}, \qquad (6.4)$$

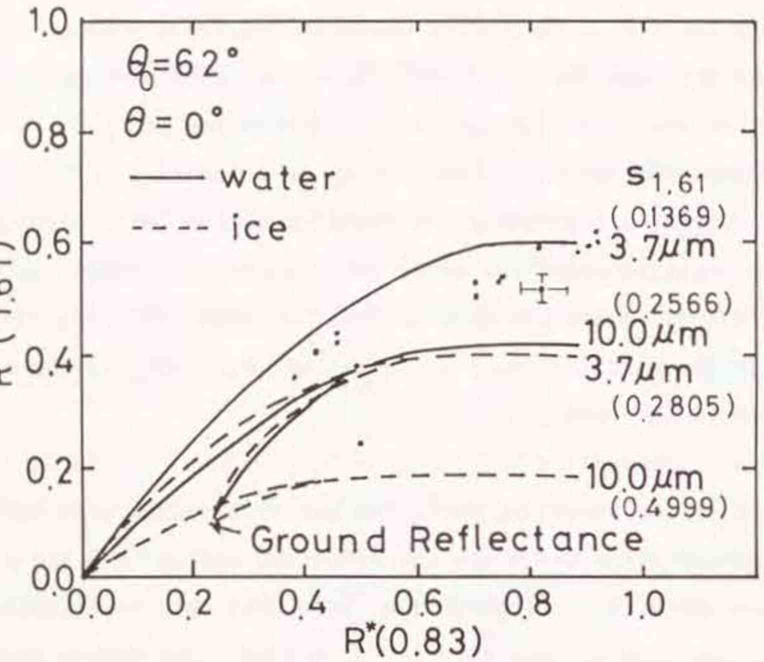

Fig.6.6 Reflection function at 0.83 μm vs 1.61 μm. The data points from Table 6.2 are shown as black dots. The absolute error is drawn on one sample point and is representing of each of the sample points. θ_0: solar zenith angle, θ: observation nadir angle. Mode radius of the particles is shown on the right of the curves. Numerals in parentheses are similarity parameter ($s_{1.61}$) (after Curran and Wu, 1982).

was 0.167±0.018. Similarly, from the reflection functions of 0.83 μm versus 2.125 μm, they estimated that 6.1±0.6 μm $<r_e<$9.1±0.6 μm for water, and 3.4±0.5 μm $<r_e<$5.8±0.4 μm for ice, respectively. The similarity parameter ($s_{2.125}$) was 0.288±0.014. From these estimated radii, Curran and Wu (1982) concluded that the clouds are composed of supercooled water droplets whose effective radii range from ~5 μm to ~10 μm.

Figure 6.7 shows the reflection function of our computational results at 0.86 μm vs 1.61 μm. The data points from Table 6.2 are shown as black dots except for the locations A and D, because these two pairs cannot be found in the figure of reflection function at 0.83 μm versus 1.61 μm shown by Curran and Wu (1982). For theoretical curves, the solar zenith angles (θ_0) are 60° and 66°, the observation nadir angle (θ) is 6°, and the azimuth differences are 0°, 90° and 180°. Background molecules are for midlatitude summer region. Aerosols are the oceanic type in the clear condition. The surface wind speed is 5m/s without whitecaps. The effect of hydrosols is excluded. The wavelength, θ_0 and θ are slightly different from those by Curran and Wu (1982). Further, property of the surface in our model is not the same as the observations. However, the effect of the surface does not seem to be very significant at R*(0.83 μm) > 0.6 (Fig.6.6). From Fig.6.7, the clouds seems to be composed of water droplets whose mode radius is greater than several microns rather than hexagonal ice crystals whose dimensions are ranging from several ten microns to several hundred microns. This result is in agreement with that by Curran and Wu (1982).

If the clouds were composed of hexagonal ice crystals, what size of crystals would give such magnitude of reflection functions? A rough estimation is given as follows on the assumption that hexagonal ice crystals are randomly oriented in space (PL3 or CL3). First, the asymmetry factor, $\langle\cos\Theta\rangle$, was estimated to be ranging from 0.65 to 0.90 for ice spheres whose radius < 30 μm from Mie scattering theory by Curran and Wu (1982); here, $\langle\cos\Theta\rangle$ is assumed to be in the same range for PL3 or CL3 whose size is of the same order. Next, the ω_0 for PL3 or CL3 is assumed to be approximated by Eq.(12) by Takano and Liou (1989a) as a function of the radius (a) and length (l) of the ice crystal and

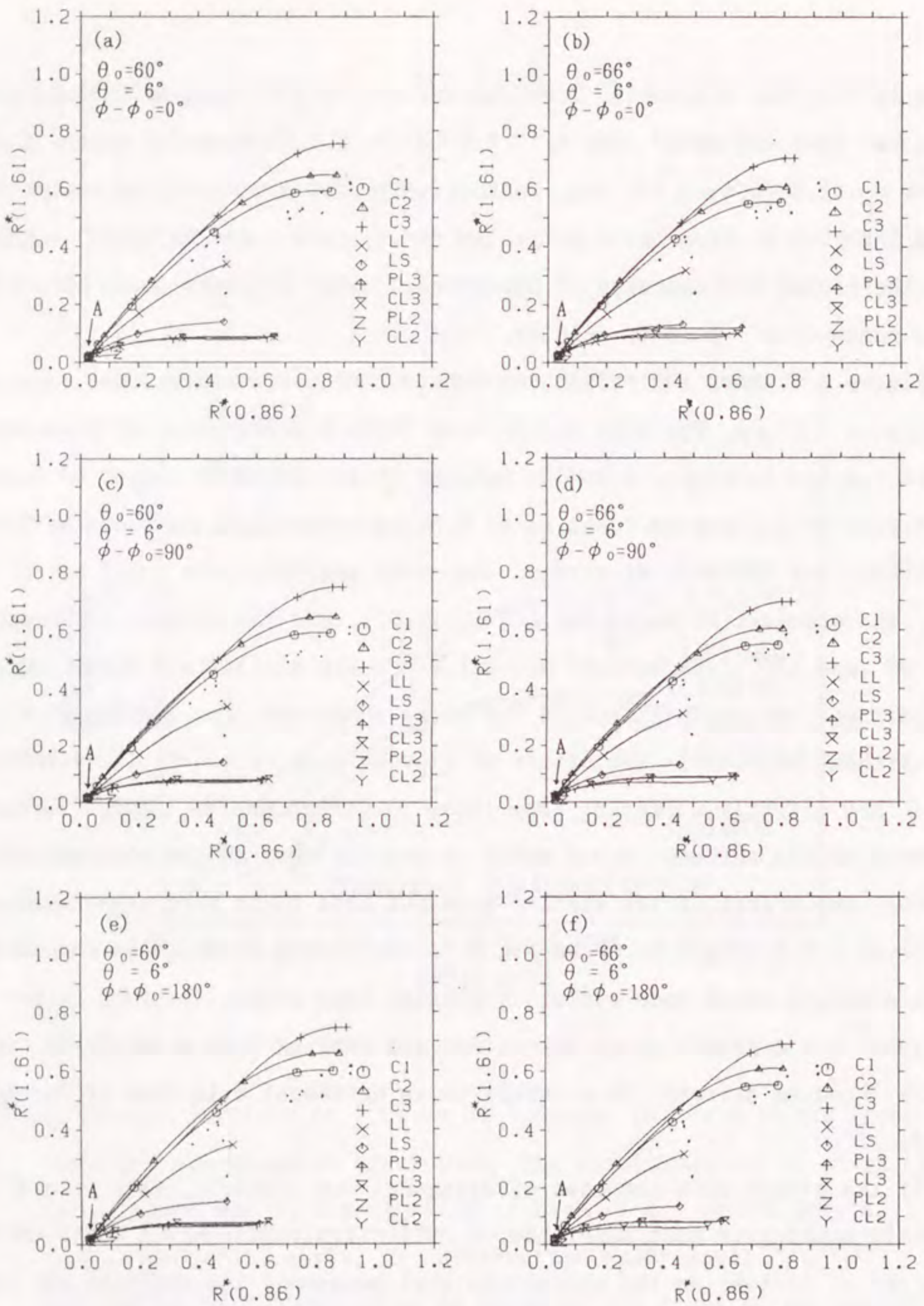

Fig.6.7 Reflection function at 0.86 μm vs 1.61 μm.
(a) θ_0=60°, θ=6°, $\phi-\phi_0$=0°, clear aerosol model.
(b) Same as (a) but for $\phi-\phi_0$=90°.
(c) Same as (a) but for $\phi-\phi_0$=180°.
(d) Same as (a) but for θ_0=66°.
(e) Same as (b) but for θ_0=66°.
(f) Same as (c) but for θ_0=66°.
The data points from Table 6.2 except for the locations A and D are shown as black dots. Cloudless model is indicated by symbol A.

the imaginary part of refractive index of ice. Using these $\langle\cos\Theta\rangle$ and ω_0, the similarity parameter ($s_{1.61}$) is obtained by Eq.(6.4). Under these assumptions, $s_{1.61}$ for PL3 and CL3 were calculated with keeping the ratio of a/l to be 100/30 and 35/245 for PL3 and CL3, respectively. The (a, l) of PL3, for which $s_{1.61}$ is 0.167, were (10.1, 3.1), (8.7, 2.6), (7.3, 2.2), (5.8, 1.8), (4.4, 1.3), and (2.9, 0.9), respectively for $\langle\cos\Theta\rangle$ = 0.65, 0.70, 0.75, 0.80, 0.85, and 0.90. Similarly, they were (3.0, 20.8), (2.5, 17.8), (2.0, 14.8), (1.7, 11.8), (1.3, 8.8), and (0.8, 5.9), for CL3. Thus if clouds were composed of hexagonal ice crystals whose (a, l) are (10 μm, 3 μm) ~ (3 μm, 1 μm) or (3 μm, 20 μm) ~ (1 μm, 6 μm), the observed reflection function might be obtained. Unfortunately the geometrical optics approximation for calculating the phase function are applicable only to the ice crystals whose size is much larger than the wavelength considered (Liou,1980). Further, *in situ* observations of ice crystals of this order of dimensions have been limited (Liou, 1986). Therefore, it is difficult to conclude that the clouds observed by Skylab are composed of ice crystals of the above dimension from the method described in this thesis.

6.7 Summary and Conclusions

Reflectance and radiance of the upwelling radiation from the model atmosphere-ocean system were computed at λ=0.63 μm, 0.86 μm, and 1.61 μm. These correspond to the effective wavelengths of the visible and near-IR channels of the future NOAA-AVHRR radiometer. The cirrus cloud layer inserted into the atmosphere was assumed to be composed of either water particles or ice crystals. In the case of ice crystal cirrus cloud, hexagonal ice crystals (columns or plates) were assumed to be randomly oriented in space or in the horizontal plane with long axis horizontal.

Based on simulation, the salient features of the dependence of the reflectance and upwelling radiation on various cirrus parameters are summarized as follows. The reflectance (ρ) at 0.63 μm and 0.86 μm increases logarithmically with the increase of cloud optical thickness (τ) in the region, $1<\tau<20$ for solar zenith angle (θ_0)=60°. For θ_0=60° ρ ranges within ~0.1 with the various cloud types adopted for the present simulation. For the 3D ice crystal layers, it varies within ~0.06. The reflectance is higher for water clouds than for 3D ice crystal clouds, but for some θ_0, a 2D cloud exhibits a higher reflectance than that of a water cloud. At $\lambda = 1.61\,\mu m$, the reflectance is mainly affected by τ and the thermodynamic phase of cloud. For $\theta_0 = 60°$ the reflectance of a water cloud increases with an increase of τ, whereas that of an ice crystal cloud does so little. This characteristic may be mainly due to the difference in the imaginary part of their refractive indices.

The radiance of 3D type ice crystal clouds changes rather smoothly with observation angle (θ), exhibiting an angular distribution similar to that of a water cloud, except that it shows halos ~22° and ~46° away from the solar direction. The radiance of 2D type ice crystal clouds (PL2 and CL2) exhibits an irregular change with θ. Furthermore, for PL2 clouds such optical phenomena as subsun are noted even if τ is small (~0.2). This is typical of 2D type ice crystal clouds. With the aid of satellite data from a $1.61\,\mu m$ channel and from either a $0.63\,\mu m$ or $0.86\,\mu m$ channel, discrimination among cloud types (water cloud, ice crystal cloud, and PL2 cloud) is possible when τ is moderate or large. In this case, data from the $0.86\,\mu m$ channel are more suitable for the analysis rather than those from the $0.63\,\mu m$ channel because of the smaller absorptive effect of stratospheric ozone together with the smaller molecular scattering. Finally, the computational result of reflection function was compared with the Skylab observations. From the reflection functions at $0.86\,\mu m$ and $1.61\,\mu m$, the observed clouds seems to be composed of water droplets whose mode radii is greater than several microns. This result is in agreement with that by Curran and Wu (1982).

Chapter 7 Conclusions

A numerical simulation was carried out to estimate the effects of cirrus cloud parameters (e.g., optical thickness, water content, and shape, dimension, orientation, thermodynamic phase of the cloud particles) on the earth radiation budget, and to develop a method for deriving cirrus cloud parameters over the ocean using the visible and near-IR channels of the future series of satellite-borne NOAA-AVHRR radiometers. In this thesis, first, the optical properties of single scattering were examined in Chapter 3 for (1) hexagonal ice crystals randomly oriented in space; (2) randomly oriented with long axis in the horizontal plane; and (3) spherical water particles. Next, dependence of radiation absorbed in the ocean (I^{w}_{abs}), together with the reflected radiation at the top (I^{t}), on atmospheric and oceanic parameters including cirrus cloud parameters was estimated using a realistic plane-parallel, vertically inhomogeneous atmosphere-ocean model in Chapters 4 and 5. A method to infer I^{w}_{abs} and I^{t} from the NOAA-AVHRR radiometer, together with its accuracy, was discussed. Finally, in Chapter 6, a retrieval technique of cloud parameters for the next-generation NOAA meteorological satellite was discussed.

The dependence of I^{w}_{abs} and I^{t} on various atmospheric and oceanic parameters is shown in Chapter 4 under a cloudless condition. For this cloudless condition, we have the following conclusions. (1) I^{w}_{abs} and I^{t} depend mainly on the atmospheric turbidity. Different aerosol types also affect I^{w}_{abs}. (2) Precipitable water also affects I^{w}_{abs}, but have little effect on I^{t}. (3) Ozone amount has some effect on I^{w}_{abs}, but very little on I^{t}. (4) The surface roughness without whitcaps shows little effect on I^{w}_{abs} and I^{t}. (5) Whitecaps affect I^{w}_{abs} and I^{t} when v >10m/s, particularly in cases of small solar zenith angles. (6) The oceanic hydrosols show little effect on I^{w}_{abs} and I^{t}, except when they are of the pure scattering type in a turbid condition. I^{w}_{abs} may be roughly evaluated using I^{t} obtained from space by neglecting absorption by the atmospheric constituents (I^{a}_{abs}), but in this procedure I^{a}_{abs} (irradiance absorbed by the atmosphere) remains as an error. Therefore, to improve the accuracy of I^{w}_{abs}, I^{a}_{abs} should be evaluated simultaneously. Moreover, a precise investigation of the optical characteristics and turbidity of hydrosols would also be required to improve the accuracy of I^*_{abs}.

The dependence of I^*_{abs} and I^t on cirrus cloud parameters, such as the thermodynamic phase of the cloud particles and the shape and orientation of the hexagonal ice crystals, is discussed in Chapter 5. The dispersion of I^t and I^*_{abs} ($|\Delta I^t|$ and $|\Delta I^*_{abs}|$) among all nine cloud types considered in this thesis are >30Wm^{-2} and >150 Wm^{-2} for the cloud optical thickness of τ=1 and 10, respectively for θ_0=30°. For all hexagonal ice crystal types (PL3, CL3, PL2 and CL2), both $|\Delta I^t|$ and $|\Delta I^*_{abs}|$ are ~30Wm^{-2} and ~100 Wm^{-2} at τ=1 and 10, respectively for θ_0=30°. These values are much larger than the accuracy of 10Wm^{-2} that is required for climatological applications. Therefore, it is essential to give the shape and orientation of the ice crystals as cirrus cloud parameters for improving the accuracy of simulation for the atmosphere model in which a cirrus cloud layer is included. In Chapter 5, the relationship between radiance (λ=0.63μm) at the top of the atmosphere (R) and I^t (or I^*_{abs}) is also investigated. Except for PL2, the dispersion of I^t and I^*_{abs} due to the cloud types range from 25Wm^{-2} to 100Wm^{-2} at R=0.05. For ice crystals (except for PL2), they could be larger than 50Wm^{-2}, which is due to differences in shape and orientation of hexagonal ice crystals. These seem to be systematic errors that cannot be reduced by averaging. Therefore to derive I^t and I^*_{abs} accurately from satellite measurements, it is necessary to know the shape and orientation of the ice crystals in addition to the thermodynamic phase of the cloud.

In Chapter 6, radiance of the upwelling radiation from the model atmosphere-ocean system is computed at λ=0.63μm, 0.86μm, and 1.61μm, which correspond to the effective wavelengths of the visible and near-IR channels of the future NOAA-AVHRR radiometer. The radiance of 3D type ice crystal clouds (PL3 and CL3) changes rather smoothly with observation angle (θ), exhibiting an angular distribution similar to that of a water cloud. The radiance of 2D type ice crystal clouds (PL2 and CL2) exhibits an irregular change with θ. Furthermore, for PL2 clouds such optical phenomena as subsun are noted even if τ is small (~0.2). This is typical of 2D type ice crystal clouds. With the aid of satellite data from a 1.61μm channel and from either a 0.63μm or 0.86

μm channel, discrimination is possible among cloud types (water cloud, ice crystal cloud, and PL2 cloud) when τ is moderate or large. In this case, data from the 0.86μm channel are more suitable for the analysis rather than those from the 0.63μm channel because of the smaller absorptive effect of stratospheric ozone together with the smaller molecular scattering. Comparison of the computational results of reflection function with the Skylab observations is also described in Chapter 6.

The results shown in this thesis are for a particular cloud model: the ice crystal particles are assumed to be hexagonal columns or plates, the orientation is randomly oriented in space (PL3, CL3) or randomly oriented in the horizontal plane (PL2, CL2), the size of the ice crystals is fixed, the cloud consists of a homogeneous single layer, and so on. An actual cloud would not necessarily satisfy such conditions. In particular, the effect of size parameter (size/wavelength ratio) and ratio of radius to length of ice particles should also be investigated. Recently, polarization measurements from satellites, such as EOSP (Earth Observing Scanning Polarimeter) and POLDER (Polarization and Directionality of Reflectances), are proposed (WMO, 1990). Therefore, this work should be extended for the case involving polarization information.

Appendix A Basic Radiative Quantities

Consider the differential amount of radiant energy dE_λ in a time interval dt and in a specified wavelength interval λ to $\lambda+d\lambda$, which crosses an element of area dA depicted in Fig.A.1, and in directions confined to a differential solid angle, which is oriented at an angle θ to the normal of dA. This energy is expressed in terms of the monochromatic radiance R_λ by

$$dE_\lambda = R_\lambda \cos\theta \, d\Omega \, dA \, d\lambda \, dt. \tag{A.1}$$

From Eq.A.1, the monochromatic radiance is expressed by,

$$R_\lambda = dE_\lambda / (\cos\theta \, d\Omega \, dA \, d\lambda \, dt). \tag{A.2}$$

Thus the radiance is in units of energy per area, per time, per wavelength, and per steradian ($Wm^{-3}sr^{-1}$). The radiance R_λ integrated over the wavelength region is denoted by R and is called the integrated radiance ($Wm^{-2}sr^{-1}$); namely,

$$R = \int_{\lambda_1}^{\lambda_2} R_\lambda \, d\lambda, \tag{A.3}$$

where λ_1 and λ_2 are lower and upper boundaries of the wavelength region considered.

The monochromatic flux density or the monochromatic irradiance (Wm^{-3}) of radiant energy is defined by the normal component of R_λ integrated over the entire spherical solid angle and may be written as

$$F_\lambda = \int_\Omega R_\lambda \cos\theta \, d\Omega. \tag{A.4}$$

In polar coordinates, we write,

$$F_\lambda = \int_0^{2\pi} \int_0^{\pi/2} R_\lambda(\theta, \phi) \cos\theta \sin\theta \, d\theta \, d\phi. \tag{A.5}$$

The total flux density or irradiance (Wm^{-2}) is obtained by integrating the monochromatic flux density or the monochromatic irradiance over the wavelength region,

$$F = \int_{\lambda_1}^{\lambda_2} F_\lambda \, d\lambda. \tag{A.6}$$

The dimensionless monochromatic reflectance is defined by,

$$\rho_\lambda = F_\lambda / (\mu_0 \pi F_{0\lambda}), \tag{A.7}$$

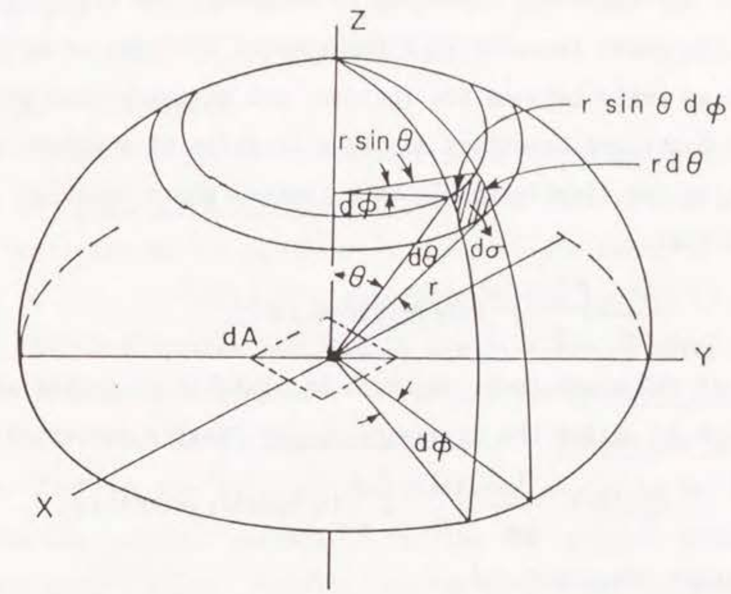

Fig.A.1 Diagram representing a solid angle in polar coordinates. The differential area in polar coordinates is given by $d\sigma = (r d\theta)(r \sin\theta \, d\phi)$, hence, the differential solid angle is $d\Omega = d\sigma / r^2 = \sin\theta \, d\theta \, d\phi$.

where F_λ, μ_0, and $\pi F_{0\lambda}$ are the upward monochromatic flux density, cosine of the direction of the incident radiation, and the monochromatic flux density of incident radiation normal to its direction. Similarly, total <u>reflectance</u> is obtained by,

$$\rho = F/(\mu_0 \pi F_0). \tag{A.8}$$

The angular distribution of the scattered energy is described by the <u>phase function</u> P. For spherical particles or hexagonal ice crystals randomly oriented in space, the phase function is a function of the scattering angle Θ which is defined as an angle between the incident and scattered radiations. The optical properties described hereafter may be a function of wavelength (λ), but symbol λ is omitted for simplicity. In this thesis, phase function is normalized to unity such that,

$$\frac{1}{4\pi}\int_0^{2\pi}\int_0^{\pi} P(\Theta)\sin\Theta\, d\Theta\, d\phi = 1. \tag{A.9}$$

The shape of the phase function could be usefully characterized by a single number which is called the <u>asymmetry factor</u> $\langle\cos\Theta\rangle$ expressed by,

$$\langle\cos\Theta\rangle = \frac{1}{4\pi}\int_0^{2\pi}\int_0^{\pi} P(\Theta)\cos\Theta\sin\Theta\, d\Theta\, d\phi. \tag{A.10}$$

$\langle\cos\Theta\rangle$ varies between 1 and -1.

The phase function for the ice crystals randomly oriented in the horizontal plane is a function of the direction of the incident and scattered radiations. In this case the phase function is normarized to unity such that,

$$\frac{1}{4\pi}\int_0^{2\pi}\left\{\int_0^1 P(\mu,\phi;-\mu_0,\phi_0)\,d\mu + \int_0^1 P(-\mu,\phi;-\mu_0,\phi_0)\,d\mu\right\}d\phi = 1. \tag{A.11}$$

where μ_0 and ϕ_0 are cosine of the zenith angle and azimuth angle of the incident radiation, and μ and ϕ are those of the scattered radiation, respectively. Here μ and μ_0 are positive. In Eq.A.11, μ_0 and μ show that the directions of the radiations are upward, whereas $-\mu_0$ and $-\mu$ show that the directions of the radiations are downward, respectively. The incident radiation is assumed to be from above. $\langle\cos\Theta\rangle$ is expressed by,

$$\langle\cos\Theta\rangle = \frac{1}{4\pi}\int_0^{2\pi}\left\{\int_0^1 P(\mu,\phi;-\mu_0,\phi_0)\cos\Theta\, d\mu + \int_0^1 P(-\mu,\phi;-\mu_0,\phi_0)\cos\Theta\, d\mu\right\}d\phi \tag{A.12}$$

where cosine of the scattering angles are obtained by,

$$\cos\Theta = -\mu\mu_0 + ((1-\mu^2)(1-\mu_0^2))^{1/2}\cos(\phi-\phi_0), \tag{A.13}$$

for the first term, and

$$\cos\Theta = \mu\mu_0 + ((1-\mu^2)(1-\mu_0^2))^{1/2}\cos(\phi-\phi_0), \tag{A.14}$$

for the second term, respectively.

The radiation incident on particles is partly scattered and partly absorbed by the particles. The <u>scattering cross section</u> (σ^s: m^2) is an area such that the total energy scattered by the particle is equal to the energy of incident radiation falling on σ^s. Similarly, the <u>absorption cross section</u> (σ^a: m^2) is an area such that the total energy absorbed by the particle is equal to the energy of incident radiation falling on σ^a. Further the <u>extinction cross section</u> (σ^e: m^2) is defined as the sum of σ^s and σ^a. <u>Albedo for single scattering</u> ($\omega_0 = \sigma^s/\sigma^e$) is the ratio of the scattered energy to the total energy removed from the incident radiation. For the ice crystals randomly oriented in the horizontal plane, $\langle\cos\Theta\rangle$, σ^s, σ^a, σ^e, and ω_0 are functions of the zenith angle of the incident radiation. The dimensionless <u>optical thickness</u> (τ) between two points of s_1 and s_2 is defined using the extinction cross section by,

$$\tau = \int_{s_1}^{s_2} \sigma^e(s) N(s)\, ds, \tag{A.15}$$

where N(s) is the number density of particles per unit volume (m^{-3}).
The radiance R_0 becomes $R_0 \cdot \exp(-\tau)$ after passing through the medium of optical thickness of τ.

<u>Appendix B Single Scattering Albedo of the Hexagonal Ice Crystals</u>

The single scattering albedo (ω_0) might significantly affect I^t and I^*_{obs}. Unfortunately, the computations of phase functions for hexagonal ice crystals consume much CPU time using geometrical optics approximation. Therefore, in the present simulation ω_0 are computed at 10 wavelengths shown in Table 5.1. ω_0 for all 108 wavelengths are approximated by modifying ω_0 of the ice sphere (LS model), which are computed from Mie scattering theory, so that they are identical to ω_0 of the ice crystals at the above 10 wavelengths. The procedure is as follows.

Let ω_{0i}^{c} be the single scattering albedo of the hexagonal ice crystals at the wavelength λ_i^c for $i=1...n_c$. Similarly let ω_{0j}^{s} be the single scattering albedo of the LS model at the wavelength λ_j^s for $j=1...n_s$. Here, n_c and n_s are 10 and 108, respectively.

step 1. Compute the co-albedo c_i^c and c_j^s for $i=1...n_c$ and for $j=1...n_s$, respectively. $c_i^c=1-\omega_{0i}^c$ and $c_j^s=1-\omega_{0j}^s$.

step 2. Interpolate the co-albedo of the LS model at λ_i^c for $i=1...n_c$ (c'^s_i).
If $\lambda_i^c < \lambda_1^s$ then $c'^s_i=c_1^s$: $\lambda_i^c > \lambda_{n_s}^s$ then $c'^s_i=c^s_{n_s}$:
otherwise $c'^s_i=c^s_{k-1}+(c^s_k-c^s_{k-1})(\lambda^c_i-\lambda^s_{k-1})/(\lambda^s_k-\lambda^s_{k-1})$ where $\lambda^s_{k-1}<\lambda^c_i<\lambda^s_k$.

step 3. Compute the ratio of c'^s_i to c^c_i for $i=1...n_c$ (r_i).
If $c'^s_i\neq0$ and $c^c_i\neq0$ then $r_i=c'^s_i/c^c_i$: otherwise $r_i=1$.

step 4. Interpolate r_i at λ^s_j for $j=1...n_s$ (r^*_j).
If $\lambda^s_j < \lambda^c_1$ then $r^*_j=r_1$: $\lambda^s_j > \lambda^c_{n_c}$ then $r^*_j=r_{n_c}$:
otherwise $r^*_j=r_{k-1}+(r_k-r_{k-1})(\lambda^s_j-\lambda^c_{k-1})/(\lambda^c_k-\lambda^c_{k-1})$ where $\lambda^c_{k-1}<\lambda^s_j<\lambda^c_k$.

step 5. Compute the co-albedo c^*_j for $j=1...n_s$.
$c^*_j=c^s_j/r^*_j$.

step 6. Compute the albedo for single scattering for hexagonal ice crystals ω^*_{0j} for $j=1...n_s$.
$\omega^*_{0j}=1-c^*_j$.

References

Ahmad, Z., Sutton, J., Stowe, LL., and Rao, C. R. N. (1989), A regression method for estimating atmospheric aerosol properties from a modified AVHRR instrument, *IRS'88: Current Problems in Atmospheric Radiation* (J. Lenoble and J. F. Geleyn, Eds.), A. Deepak, pp. 575-578.

Arking, A., and Childs, J. D. (1985), Retrieval of cloud cover parameters from multispectral satellite images, *J. Climate Appl. Meteorol.* 24:322-333.

Asano, S. (1983), Transfer of solar radiation in optically anisotropic ice clouds, *J. Meteorol. Soc. Japan* 61:402-413.

Barton, I. J. (1983), Upper level cloud climatology from an orbiting satellite, *J. Atmos. Sci.* 40:435-447.

Bohren C. F., and Huffman D. R. (1983), *Absorption and Scattering of Light by Small Particles*, John Wiley & Sons, 530pp.

Born, M., and Wolf, E. (1964), *Principles of Optics*, Pergamon Press, 808pp.

Cai, Q., and Liou, K. N. (1982), Polarized light scattering by hexagonal ice crystals: theory, *Appl. Opt.* 19:3569-3580.

Chandrasekhar, S. (1960), *Radiative Transfer*, Dover, 393pp.

Coleman, R. F., and Liou, K. N. (1981), Light scattering by hexagonal ice crystals, *J. Atmos. Sci.* 38:1260-1271.

Cox, C., and Munk, W. (1955), Some problems in optical oceanography, *J. Mar. Res.* 14:63-78.

Curran, R. J., and Wu, M. C. (1982), Skylab near-infrared observations of clouds indicating supercooled liquid water droplets, *J. Atmos. Sci.* 39:635-647.

de Haan, J. F., Bosma, P. B., and Hovenier, J. W. (1987), The adding method for multiple scattering calculations of polarized light, *Astron. Astrophys.* 183:371-391.

Deirmendjian, D. (1969), *Electromagnetic Scattering on Spherical Polydispersions*, Elsevier, New York, 290pp.

Diak, G. R., and Gautier, C. (1983), Improvements to a simple physical model for estimating insolation from GOES data, *J. Climate Appl. Meteorol.* 22:505-508.

Dobson, F. W., and Smith, S. D. (1988), Bulk models of solar radiation at sea, *Quart. J. Roy. Meteorol. Soc.* 114:165-182.

Feddes, R. G., and Liou, K. N. (1978), Atmospheric ice and water content derived from parameterization of Nimbus 6 High-Resolution Infrared Sounder data, *J. Appl. Meteorol.* 17:536-551.

Freeman, K. P., and Liou, K. N. (1979), Climatic effects of cirrus clouds, *Adv. Geophys.* 21:231-287.

Gautier, C., Diak, G., and Masse, S. (1980), A simple physical model to estimate incident solar radiation at the surface from GOES satellite data, *J. Appl. Meteorol.* 19:1005-1012.

Greenler, R. (1980), *Rainbows, Halos, and Glories*, Cambridge University Press, Cambridge, 195pp.

Hale, G. M., and Querry, M. R. (1973), Optical constants of water in the 200-nm to 200-μm wavelength region, *Appl. Opt.* 12:555-563.

Hansen, J. E., (1971), Multiple scattering of polarized light in planetary atmospheres. Part I. The doubling method, *J. Atmos. Sci.* 28:120-125.

Hansen, J. E., and Travis, L. D. (1974), Light scattering in planetary atmospheres, *Space Science Reviews* 16:527-610.

Heymsfield, A. J., and Platt, C. M. R. (1984), A parameterization of the particle size spectrum of ice clouds in terms of the ambient temperature and the ice water content, *J. Atmos. Sci.* 41:846-855.

Iqbal, M. (1983), *An Introduction to Solar Radiation*, Academic Press, 390pp.

Ito, S., and Oguchi, T. (1987), An approximate method for solving the vector radiative transfer equation in discrete random media, *Radio Science* 22:873-879.

Jacobowitz, H. (1971), A method for computing the transfer of solar radiation through clouds of hexagonal ice crystals, *J. Quant. Spectrosc. Radiat. Transfer* 11:691-695.

Kneizys, F. X., et al. (1983), Atmospheric transmittance/radiance: computer code LOWTRAN 6, Air Force Geophysics Laboratory, AFGL-TR-83-0187.

Koepke, P. (1984), Effective reflectance of oceanic whitecaps, *Appl. Opt.* 23:1816-1824.

Lacis, A. A., and Hansen, J. E., (1974), A parameterization for the absorption of solar radiation in the earth's atmosphere, *J. Atmos. Sci.* 31:118-133.

Lenoble, J. (1985), *Radiative Transfer in Scattering and Absorbing Atmospheres: Standard Computational Procedures*, A. Deepak, 300pp.

Liou, K. N. (1974), On the radiative properties of cirrus in the window region and their influence on remote sensing of the atmosphere, *J. Atmos. Sci.* 31:522-532.

Liou, K. N. (1980), *An Introduction to Atmospheric Radiation*, Academic, Orlando, San Diego, New York, London, Toronto, Montreal, Sydney, and Tokyo, 392pp.

Liou, K. N. (1986), Influence of cirrus clouds on weather and climate processes: A global perspective, *Monthly Weather Review*, 114:1167-1199.

Masuda, K., and Takashima, T. (1986), Computational accuracy of radiation emerging from the ocean surface in the model atmosphere-ocean system, *Pap. Meteorol. Geophy.* 37, 1-13.

Masuda, K., and Takashima, T. (1988), Sensitivity of radiation absorbed in the ocean to atmospheric and oceanic parameters in the short wavelength region part I. cloudless atmosphere, *J. Meteorol. Soc. Japan* 66:617-628.

Masuda, K., and Takashima, T. (1989), Numerical estimation of the effect of multiple scattering by horizontally randomly oriented hexagonal ice crystals, *IRS'88: Current Problems in Atmospheric Radiation* (J. Lenoble and J. F. Geleyn, Eds.), A. Deepak, pp. 53-56.

Masuda, K., and Takashima, T. (1990a), Deriving cirrus information using the visible and near-IR channels of the future NOAA-AVHRR radiometer, *Remote Sens. Environ.* 31:65-81.

Masuda, K., and Takashima, T. (1990b), Sensitivity of shortwave radiation absorbed in the ocean to cirrus parameters, *Remote Sens. Environ.* 33:75-86.

Masuda, K., Takashima, T., and Rao, C. R. N. (1988), Remote sensing of atmospheric aerosols over the oceans using multispectral radiances measured with the Advanced Very High Resolution Radiometer onboard the NOAA meteorological satellites, *Aerosols and climate* (P. V. Hobbs and M. P. McCormick, Eds.), A. Deepak, pp. 39-49.

Monahan, E. C. (1971), Oceanic whitecaps, *J. Phys. Oceanogr.* 1:139-144.

Morel, A. (1974), In *Optical Aspects of Oceanography* (N. G. Jerlov, and E. S. Nielsen, Eds.), Academic, London, pp. 1-24.

Möser, W., and Raschke, E. (1983), Mapping of global radiation and of cloudiness from METEOSAT image data. Theory and ground truth comparisons, *Meteorol. Rdsch.* 36:33-41.

Muinonen, K., Lumme, K., Peltoniemi, J., and William, M. I. (1989), Light scattering by randomly oriented crystals, *Appl. Opt.* 28:3051-3060.

Nakajima, T., and Tanaka, M. (1983), Effect of wind-generated waves on the transfer of solar radiation in the atmosphere-ocean system, *J. Quant. Spectrosc. Radiat. Transfer* 29:521-537.

Nakajima, T., and Tanaka, M. (1986), Matrix formulations for the transfer of solar radiation in a plane-parallel scattering atmosphere, *J. Quant. Spectrosc. Radiat. Transfer* 35:13-21.

Ono, A. (1969), The shape and riming properties of ice crystals in natural clouds, *J. Atmos. Sci.* 26:138-147.

Ono, A. (1970), Growth mode of ice crystals in nature clouds, *J. Atmos. Sci.* 27:649-658.

Plass, G. N., and Kattawar, G. W. (1971), Radiative transfer in water and ice clouds in the visible and infrared region, *Appl. Opt.* 10:738-748.

Plass, G. N., Kattawar, G. W., and Catchings, F. E. (1973), Matrix operator theory of radiative transfer. 1: Rayleigh scattering, *Appl. Opt.* 12:314-329.

Platt, C. M. R., Abshire, N. L., and McNice, G. T. (1978), Some microphysical properties of an ice cloud from lidar observation of horizontally oriented crystals, *J. Appl. Meteorol.* 17:1220-1224.

Platt, C. M. R., Spinhirne, J. D., and Hart, W. D. (1989), Optical and microphysical properties of a cold cirrus cloud: evidence for regions of small ice particles, *J. Geophys. Res.* 94:11151-11164.

Quenzel, H., and Kaestner, M. (1980), Optical properties of the atmosphere: calculated variability and application to satellite remote sensing of phytoplankton, *Appl. Opt.* 19:1338-1344.

Radiation Commission, IAMAP(1986), A preliminary cloudless standard atmosphere for radiation computation, WCP-112, WMO/TD-No. 24. (World Meteorological Organization, Geneva)

Rao, C. R. Nagaraja, and Takashima, T. (1986), Solar radiation anomalies caused by the El Chichon volcanic cloud: Measurements and model comparisons, *Quart. J. Roy. Meteorol. Soc.* 112:1111-1126.

Raschke, E., and Rockwitz, K. D. (1989), The international cirrus experiment some preliminary results from the first field phase, *IRS'88: Current Problems in Atmospheric Radiation* (J. Lenoble and J. F. Geleyn, Eds.), A. Deepak, pp. 6-9.

Reed, R. K. (1977), On estimating insolation over the ocean, *J. Phys. Oceanogr.* 7:482-485.

Schiffer, R. A., and Rossow, W. B. (1983), The International Satellite Cloud Climatology Project (ISCCP): The first project of the World Climate Research Programme, *Bull. Am. Meteorol. Soc.* 64:779-784.

Selby, J. E. A., and McClatchey, R. M. (1972), Atmospheric transmittance from 0.25 to 28.5 μm: computer code LOWTRAN2, Air Force Cambridge Research Laboratory, AFCRL-72-0745.

Shettle, E. P., and Fenn, R. W. (1979), Models for the aerosols of the lower atmosphere and the effects of humidity variations on their optical properties, Air Force Geophysics Laboratory, AFGL-TR-79-0214.

Sparkman, Jr., J., K. (1989), NOAA polar orbiting sensor systems Today and tomorrow, *Int. J. Remote Sensing* 10:609-612.

Stamnes, K., Tsay, S. C., Wiscombe, W., and Jayaweera, K. (1988), Numerically stable algorithm for discrete-ordinate-method radiative transfer in multiple scattering and emitting layered media, *Appl. Opt.* 27:2502-2509.

Stephens, G. L. (1980), Radiative transfer on a linear lattice: application to anisotropic ice crystal clouds, *J. Atmos. Sci.* 37:2095-2104.

Takano, Y., and Jayaweera, K. (1985), Scattering phase matrix for hexagonal ice crystals computed from ray optics, *Appl. Opt.* 24:3254-3263.

Takano, Y., and Liou, K. N. (1989a), Solar radiative transfer in cirrus clouds. PartI: Single-scattering and optical properties of hexagonal ice crystals, *J. Atmos. Sci.* 46:3-19.

Takano, Y., and Liou, K. N. (1989b), Solar radiative transfer in cirrus clouds. PartII: Theory and computation of multiple scattering in an anisotropic medium, *J. Atmos. Sci.* 46:20-36.

Takashima, T. (1975), A new approach of the adding method for the computations of emergent radiation of an inhomogeneous plane-parallel planetary atmosphere, *Astrophys. Space Sci.* 36:319-328.

Takashima, T., (1985), Polarization effect on radiative transfer in planetary composite atmospheres with interacting interface, *Earth, Moon, and Planets*, 33:59-97.

Takashima, T., and Masuda, K. (1988), Validation of single scattering approximation for an atmospheric correction on satellite data in the visible region, *J. Remote Sens. Soc. Japan* 8:101-111.

Tanaka, M., and Nakajima, T. (1977), Effects of oceanic turbidity and index of refraction of hydrosols on the flux of solar radiation in the atmosphere-ocean system, *J. Quant. Spectrosc. Radiat. Transfer* 18:93-111.

Tarpley, J. D. (1979), Estimating incident solar radiation at the surface from geostationary satellite data, *J, Appl. Meteorol.* 18:1172-1181.

Tränkle, E., and Greenler, R. G. (1987), Multiple scattering effects in halo phenomena, *J. Opt. Soc. Am. A.* 4:591-599.

Twomey, S., Jacobowitz, H., and Howell, H. B. (1966), Matrix methods for multiple-scattering problems,, *J. Atmos. Sci.* 23:289-296.

van de Hulst, H. C. (1980), *Multiple Light Scattering: Tables, Formulas, and Applications*, Vols. 1 and 2, Academic Press, 739pp.

Varley, D. J. (1978), Cirrus particle distribution study: part I, Air Force Geophysics Laboratory, AFGL-TR-78-0192.

Warren, S. G. (1984), Optical constants of ice from the ultraviolet to the microwave, *Appl. Opt.* 23:1206-1225.

Wendling, P., Wendling, R., and Weickmann, H. K. (1979), Scattering solar radiation by hexagonal ice crystal, *Appl. Opt.* 18:2663-2671.

Wielicki, B. A., Suttles, J. T., Parker, L., and Arduini, R. F. (1990), Satellite derived cirrus particle size: tropical clouds, *Proc. Seventh Conference on Atmospheric Radiation* 16-22.

Wiscombe, W. J. (1976), On initialization, error and flux conservation in the doubling method, *J. Quant. Spectrosc. Radiat. Transfer* 16:637-658.

World Meteorological Organization (1984), Report of the TOGA workshop on sea surface temperature and net surface radiation, WCP-92.

World Meteorological Organization (1986), Report of the workshop on surface radiation budget for climate applications (J. T. Suttles, and G. Ohring, Eds.), WCP-115, WMO/TD-No. 109.

World Meteorological Organization (1990), Report of the experts meeting on space observations of tropospheric aerosols and complementary measurements (L. L. Stowe, R. Hitzenberger, and A. Deepak, Eds.), WCRP-48, WMO/TD-No. 389.

Yeh, H. Y. (1984), Determination of cloud parameters from infrared sounder data, *J. Geophys. Res.* 89:11759-11770.

Yeh, H. Y., and Liou, K. N. (1983), Remote sounding of cloud parameters from a combination of infrared and microwave channels, *J. Climate Appl. Meteorol.* 22: 201-213.